C h a p t e r 4

CHARACTERIZING EMISSIVITY SPECTRA FROM GEOMORPHIC SURFACES ALONG THE SOUTHERN SAN ANDREAS FAULT

Rebecca A. Witkosky[1], Joann Stock[1], David Tratt[2], Kate Scharer[3], Kerry Buckland[2], Paul Adams[2], and Pat Johnson[2]

[1]*California Institute of Technology, Division of Geological and Planetary Sciences, 1200 E. California Blvd., MC 170-25, Pasadena CA 91125*

[2]*The Aerospace Corporation, 2310 E. El Segundo Blvd., El Segundo CA 90245*

[3]*U.S. Geological Survey, 525 S. Wilson Ave., Pasadena, CA 91106-3212*

ABSTRACT

Well-developed varnish and pavement are usually characteristic of relatively older geomorphic surfaces: the environment must be broad, flat, and stable for extended periods of time for these features to reach advanced stages of development. However, varnish and pavement formation rates are not understood well enough for those features alone to be used as a reliable chronometer. In this research, we combine the known ages for a set of terraced geomorphic surfaces along the Mission Creek strand of the southern San Andreas fault in the Coachella Valley, southern California, to explore the use of thermal hyperspectral airborne remote sensing imagery for identifying age-dependent characteristics of spectral emissivity

features. In spectra from an airborne sensor, the band depth of an emissivity minimum at 9.16 μm generally increases with age of geomorphic surface. The spectral position of this feature is within the wavelength range for clay minerals (9.1-9.6 μm), which suggests increasing abundance of clay minerals on older surfaces. Desert varnish is known to contain clay minerals, so it is possible that the increased clay band depth with age manifests from increasing desert varnish development on older surfaces. We collected field data to test for other effects that might contribute to the increased band depth with age. Our field results show that desert varnish and desert pavement scores (higher numerical score assigned to a greater degree of development), and vegetation spacing estimates all display some positive correlation with surface age. Ground-based spectra from hand samples that we collected display a spectral feature at 9.30 μm, which also indicates clay content, but does not occur at the exact same wavelength position as that in the airborne spectra. Most of the airborne and ground-based spectra indicate the presence of clay mineral(s), along with quartz and feldspars. Ground-based vegetation spectra are generally flat and featureless over the wavelengths covered in remote sensing imagery. In summary, it appears that while a clay mineral signal in the airborne spectra is plausible, the overall spectral contrast increases with surface age due to the combination of varnish development, topographic smoothing associated with pavement formation, and increase in vegetation spacing (net decrease in vegetation). This suggests that the positive correlation between spectral contrast in airborne remote sensing spectra and surface age can potentially be used to determine relative ages of Quaternary geomorphic surfaces.

INTRODUCTION

The southern San Andreas fault is a major tectonic plate boundary that is especially hazardous due to its location near many major population centers in southern California. Tectonism in this desert region influences the health and safety of millions of people, so the numerous specific sections and strands of the southern San Andreas fault have been rigorously studied to assess prehistoric and current seismic activity. To assess the risk, we need to know about the slip rates of the faults. To estimate fault slip rates on the basis of tectonic geomorphology, the ages of geomorphic surfaces must be known. Relative ages of surfaces can be assigned using the degree of development of surficial coatings on gravel clasts (desert varnish) and/or surficial smoothing (desert pavement), to characterize and differentiate faulted geomorphic surfaces (alluvial fans or terraces). The degree with which desert varnish and desert pavement has developed over time can indicate the relative or absolute ages of distinct geomorphic units; this type of analysis has been applied to features that have been cut and offset by California's southern San Andreas fault (e.g., Keller et al., 1982; Shifflett et al., 2002; van der Woerd et al., 2006; Behr et al., 2010). In this study, we incorporate both developmental criteria to evaluate relative ages from the perspective of remote sensing imaging spectroscopy.

Desert varnish is a potential chronometer for estimating the ages of geomorphic surfaces, but to accurately employ the chronometer, we need to know how the lithologic coating forms and develops. The formation and development of desert varnish (from herein, sometimes referred to as just "varnish" for brevity) has long attracted interest from geologists, biologists, and others. Varnish can also form in non-arid environments, and is therefore sometimes more generically referred to as "rock varnish." Ideas for the primary

formation mechanism are usually either 1) inorganic chemical alteration of, and addition to, lithologic surfaces, or 2) microbiologic activity (note that (1) and (2) are not mutually exclusive). For both cases, primary formation will also depend on whether the constituent material of the varnish was derived in situ or had been transported to the present site. A combination of these factors likely vary in relative contribution based on the specific regional and local environment. Regardless of the source of origin materials, petrographic observations of varnish usually reveal a microstratigraphy (Perry and Adams, 1978; Reneau et al., 1992), indicating it is an accretionary process, and encouraging attempts to calculate some type of accretion/sedimentation/growth rate (Liu and Broecker, 2000).

In order to use varnish as a chronometer, empirical knowledge about its growth rates is needed. Rates of growth, based on varnish thickness and the age of surfaces determined radiometrically, have been calculated with very broad results. Calculated rates range from <1 to 40 μm/ky (ky = one thousand years), with the caveat that those rates are certainly minima due to an unknown time lag between deposition and inception of growth, and the observation that older samples tend to exhibit slower growth rates (Liu and Broecker, 2000; Spilde et al., 2013). The time lag required for initiating varnish growth has been observed in a number of cases, with estimates of as little as 25 years (Engel and Sharp, 1954), up to about 100 years (Whitley and Dorn, 1987). In specific cases, faster growth rates can be attributed to an environment conducive to accelerated growth (Krinsley et al., 2012), such as more frequent and consistent moisture (Hunt, 1954; Thiagarajan and Lee, 2004). The high variability in growth rates, and the fact that a maximum varnish thickness of c. 200 μm is usually observed (Liu and Broecker, 2000; Spilde et al., 2013), precludes the use of thickness alone as a chronometer.

The idea of using varnish as a chronometer has stimulated various ideas and methods aimed at measuring the formation process. In a given region, a calibrated relationship to geologic time can be established, and then potentially used for future work (e.g., Helms et al., 2003). A rigorous and widely tested application of this method involves establishing a calibrated, standard regional time scale for the Late Pleistocene to which varnish microstratigraphy can be correlated (Liu and Broecker, 2013). This calibrated method has yielded ages that agree with those from independent surface exposure dating methods used on the same lithologic units (Marston, 2003; Phillips, 2003; Liu, 2003). Some other methodologies for using varnish as a chronometer, namely cation ratios, and direct dating using accelerator mass spectrometry, are not yet reliably developed (e.g., see reviews by Beck et al., 1998; Watchman, 2000).

Desert varnish often includes a high relative abundance of clay minerals (Potter and Rossman, 1977), so perhaps geomorphic surfaces with varnished clasts can be spectroscopically distinguished by measuring relative clay content. Due to their predominantly submicroscopic size, clay mineral grains are commonly detected and identified via laboratory methods, including x-ray diffraction (XRD) and spectroscopy. Remote sensing data and methods (i.e., imaging spectroscopy) are an extension of laboratory spectroscopy, and with recent technological development, the limitations of low spectral and spatial resolution have been overcome on many modern platforms.

For this study, we are focusing on distinguishing varnish that has accumulated on a chemically dissimilar (mineralogic/petrologic) substrate material. We can take advantage of previous work that used spectroscopy and remote sensing to determine the mineralogy and petrology of substrate material that lies beneath coatings of desert varnish. Formative

research in lithologic remote sensing has typically involved examining the way varnish represents "noise" that complicates and/or conceals the signal from its mineralogic/petrologic substrate in laboratory and imaging spectroscopy (Kahle and Goetz, 1983; Gillespie et al., 1984; Kahle, 1987; Bartholomew et al., 1989; Rivard et al., 1993; Christensen and Harrison, 1993). In this research, we are focusing on varnish as "signal," exploiting the fact that it is both opaque from manganese and iron oxide content, and contains clay minerals not always present in a substrate material, and so can be detected and identified via remote sensing methods.

Ultimately, we want to relate remote sensing of lithology and active tectonics in a way that benefit society: the age-dependent development of geomorphic surfaces, and the overprinting of continuous tectonic displacement present an opportunity to capture measurements of both time and distance. Desert varnish and related desert pavement surfaces can provide an idea of geologic age (or at least the passage of time into a current state), and tectonics can provide an idea of physical displacement, which together provide the quantities needed for a geologic fault slip rate. Varnish and pavement are often associated with Quaternary unconsolidated lithologic units, and geologic fault slip rates from these relatively young displaced features can have greater relevance for guiding risk and hazard assessment on the current state of a tectonic system.

GEOLOGIC/TECTONIC SETTING

The southern San Andreas fault in the northern Coachella Valley offsets a number of geomorphic surfaces with well-determined exposure ages (Blisniuk and Sharp, 2014). There

is also an abundance of observations of both modern and ancient seismic activity. The prehistoric, historic, and modern seismic activity have been analyzed in three main ways: 1) paleoseismic trenching to establish earthquake recurrence intervals (and in rare cases, calculate fault slip rates); 2) methods in tectonic geomorphology to establish geologic fault slip rates; and 3) Global Positioning System (GPS) and interferometric synthetic aperture radar (InSAR) data and modeling to establish present-day geodetic fault slip rates. All of these types of data can be incorporated into modeling and analyses of seismic hazards along the San Andreas fault (e.g., Jones et al., 2008; Porter et al., 2011; Davis and O'Rourke, 2011). Of these types of seismic hazards analysis mentioned above, our research is most closely related to the tectonic geomorphology approach. An overview of the other two approaches may be found in the Appendix.

Tectonic Geomorphology

The Coachella Valley region contains numerous Late Pleistocene to Holocene recognizable geomorphic features indicating a tectonically active landscape. The Indio Hills (Keller et al., 1982), Mecca Hills, Edom Hill, and Durmid Hill (Bürgmann, 1991) are all archetypal examples of how the Earth's surface responds to active strike-slip fault motion, transpression, and various modes of tectonic buckling. Fluvial channels and alluvial fans are cut and displaced, revealing both historic and prehistoric strike-slip fault motion. Those geomorphic features have been used to estimate geologic slip rates for the southern San Andreas fault, which vary widely, depending on the specific location and/or fault strand(s)

considered. For this research, we chose to analyze the Mission Creek strand of the southern San Andreas fault at Pushawalla Canyon (Figure 1).

Thousand Palms Oasis and Pushawalla Canyon areas in the Indio Hills

The remote sensing data used here includes thermal hyperspectral airborne imagery that covers a set of alluvial/fluvial deposits near the Thousand Palms Oasis and Pushawalla Canyon (Figure 1). These deposits are offset by the Mission Creek strand of the San Andreas fault, and have been dated recently using the ^{10}Be cosmogenic exposure and uranium-series methods (Blisniuk and Sharp, 2014). That study yielded a slip rate of 22-25 mm/yr, somewhat faster than rates from the same fault in nearby areas (e.g., see Behr et al., 2010; Fletcher et al., 2010). By combining our remote sensing data and techniques with their geochronology, we have a prime opportunity to perform mineral spectroscopy on varnished gravels in an area of known geomorphic surface exposure ages. This area is located within the Coachella Valley Preserve in southern California. The Coachella Valley Preserve is a protected, environmentally sensitive area. Thus, an important advantage of using hyperspectral airborne imagery for this type of research is its minimal environmental impact.

CHARACTERIZING ALLUVIAL/FLUVIAL DEPOSITS WITH REMOTE SENSING DATA AND METHODS

The Quaternary alluvial fans and fluvial terraces in this region formed in response to a combination of climatic and tectonic processes. Deposition of the detrital material can

occur under varying climatic influences, including glacial (Owen et al., 2014; Cyr et al., 2016), interglacial (Bull, 1991; Reheis et al., 1996), or transitional glacial-interglacial conditions (e.g., Bull, 1991; Friedrich et al., 2003; Pazzaglia, 2013). When deposition occurs along active faults, the tectonic influence is coupled with the climatic, affecting depositional patterns and the overall structure of the formation. Along the southern San Andreas fault, tectonic activity has contributed to uplifting broad, detrital surface deposits into uplands, forming a series of terraces. After deposition ceased and the geomorphic surfaces stabilized, the influence of the arid desert conditions set in, and the surfaces evolved with age.

The prevailing methods that are currently used for dating Quaternary deposits include analyses of cosmogenic radionuclides, luminescence, and Uranium-Thorium decay series (or "U-series," in this context, usually performed on carbonate formed in soil). All of those methods are rigorous and costly, which has encouraged other researchers to seek new dating methods that consider other physical and chemical aspects of geomorphic surface development. Here, we explore the applicability of using remote sensing data and methods, which have an economic advantage, and also, potential to characterize whole regions, particularly if they are poorly accessible. Remote sensing data and methods can be more accessible because they only require a computer and some software (albeit after significant costs and efforts to launch a platform), instead of a full laboratory setup.

Features of geomorphic surfaces relevant to age that are best characterized via remote sensing include mineralogy/petrology, and topographic surface roughness. Because older fans include a higher fraction of relatively erosion-resistant clasts (Gillespie et al., 1984), multispectral thermal infrared (8-12 μm wavelengths) airborne images produce spectra that are sensitive to compositional changes. Furthermore, as discussed below, the spectral

emissivity minimum moves to a longer wavelength as desert varnish develops on the clasts (Gillespie et al., 1984).

To quantify topographic surface roughness, digital elevation models (DEMs) produced from radar or lidar data are typically employed. With these data, Frankel and Dolan (2007; also see Frankel et al., 2007) found that topographic smoothing at the scale of 5-10 m wavelengths, the typical wavelength of bar and swale structures on alluvial surfaces, appears to occur over a time period of about ≤70 ky, after which roughness can increase if new channels begin to incise the surface as the base level of streams becomes lower. They also noted that a decrease in clast size due to weathering over time might also contribute to the overall smoothing at shorter wavelengths. Data from ground-based lidar, which is sensitive to variation in smaller clast sizes, has also been used to show that Quaternary geomorphic surfaces become topographically smoother over time (Mushkin et al., 2014).

Mushkin et al. (2014) attributed clast size reduction on geomorphic surfaces predominantly to salt weathering and shattering (e.g., Hunt and Mabey, 1966), in addition to the effects of clast exfoliation, and dissolution of carbonate rocks. Their study area was in the Jordan Rift Valley, which also includes the hypersaline Dead Sea. Salt weathering is also a dominant component in alluvial fan surface development at a site in China, where it may have hindered the advanced desert varnish and pavement development that can be comparatively observed in southern California (Farr and Chadwick, 1996). Our study area in the Coachella Valley does not consist primarily of carbonate rocks, and although there is currently a hypersaline water body in the region (the Salton Sea, and also possibly the prehistoric Lake Cahuilla; see the interpretations of Van de Kamp, 1973), salt weathering

does not appear to have played a large role in clast size reduction in the Pushawalla Canyon area.

Many previous studies have combined multiple remote sensing data types to look at the combined effects of compositional varnish and topographic smoothing. Combined approaches can take many forms, one of which used visible wavelength imagery for lithologic character, and a backscatter metric from satellite-borne radar for surface roughness (Farr and Chadwick, 1996). Jayko et al. (2005) used the panchromatic band (0.5-0.9 μm wavelengths) of the Landsat 7 satellite, and surface slope and curvature quantities derived from DEMs. The combined methods of Jayko et al. (2005) worked well in arid regions with minimal vegetation, but faltered in the following areas: 1) where the substrate lithology either quickly develops varnish, or might already resemble the ubiquitous dark color of a substantial varnish (for both cases, mafic volcanic rocks); 2) where varnish-resistant carbonate rocks abound; and 3) where rapidly-eroding fissile shales abound, presumably because higher erosion rates inhibit the stabilization necessary for a substantial coating. It is encouraging for future work that the mapping of geomorphic surfaces, at least to first order, can be fully automated using algorithms for classifying surfaces based on varying roughness and lithologic content (Jayko et al., 2005).

DESERT VARNISH

The primary chemical constituents of desert varnish are typically manganese and iron oxides (Hunt, 1954; Engel and Sharp, 1958; Perry and Adams, 1978), clay minerals (Hunt, 1954; Potter and Rossman, 1977; 1979), and silica (Perry et al., 2006; Aulinas et al., 2015).

Its characteristic black- and red-hued colors result from manganese and iron content (Perry and Adams, 1978). The specific metal oxide minerals can include hematite and birnessite, respectively (Potter and Rossman, 1979). Birnessite ($(Na,Ca,K)Mn_7O_{14}\cdot 3H_2O$) is a manganese oxide mineral that has a layered crystal structure, and is therefore similar to the phyllosilicate clay minerals that can also be present in significant abundance. Clays can compose up to 70% of the varnish (Potter and Rossman, 1977), but samples from some regions do not include a significant clay fraction. Clay-poor samples have been found instead to have main phases that include quartz polymorphs and amorphous silica (Aulinas et al., 2015). Some studies interpreted the silica to have played an important role in overall varnish formation (Perry et al., 2006). Varnishes that are predominantly silica (i.e., resemble more of a silica glaze) have been termed "Si-rich rock varnish" (Aulinas et al., 2015).

The amount of moisture present in the atmosphere, and/or within the microscopic aqueous realm on the lithologic surface, greatly affects the potential development of desert varnish (Hunt, 1954; Thiagarajan and Lee, 2004). Wet zones along river banks are also known to support significant varnish development (Krinsley et al., 2012; references therein). Despite the dependence on regional environmental conditions and ecology, the specifics on the chemical makeup of a given varnish strongly suggest that the varnish material itself does not appear to be derived from its lithologic substrate (Engel and Sharp, 1958; Potter and Rossman, 1977; 1979; Thiagarajan and Lee, 2004; Macholdt et al., 2015). Formation and development thus appears to be independent of the substrate lithology. The metal oxides are likely transported by water (Potter and Rossman, 1979), whereas the provenance of the clay minerals is more likely based on aeolian transport and deposition (Potter and Rossman, 1977; 1979; Perry and Adams, 1978). Some workers support the idea that for long-term stability

and ongoing accretion, the clays and metal oxides must both be present (Potter and Rossman, 1977), while others suggest that the manganese-rich component predates clay deposition (Krinsely et al., 2012).

A microstratigraphy is commonly present in varnish (Perry and Adams, 1978; Reneau et al., 1992; Liu and Broecker, 2000; Liu, 2003; Liu and Broecker, 2013), indicating that formation is primarily depositional or accretionary (however, for a case where microlaminations are absent, see Aulinas et al., 2015). The layered structure can also contain botryoidal or stromatolitic structures (Perry and Adams, 1978), organic compounds (Perry et al., 2006), and/or microbial-sized forms (Krinsely et al., 2012); all of those features suggest that microbiologic activity may be integral to the formation process.

The continuous accretion of varnish into a microstratigraphic structure suggests that increasing thickness might have a systematic dependence on time, but, as in the case of stratigraphy, a number of studies indicate that this is not the case. Difficulties include: 1) some substantial varnish coatings have apparently grown within a few decades to a century (Engel and Sharp, 1958; Krinsley et al., 2012); 2) younger varnishes often appear to have faster accretion rates (Liu and Broecker, 2000; Spilde et al., 2013); 3) those faster accretion rates do not appear to be sustainable for a long time, since varnish thickness >200 μm is rarely observed (Spilde et al., 2013); 4) varnished surfaces at higher elevations might not have survived the effects of glacial erosion during the Late Pleistocene, which means that a maximum age has been imposed for many locations (Quade, 2001); and 5) it might be nearly impossible to account for all of the variation in regional and local environmental factors that control the balance of accretion, erosion, and preservation at any given location.

Microtopography of the lithologic substrate has significant control over varnish accretion rates (Reneau et al., 1992) and resulting thickness (Liu and Broecker, 2000). Both accumulation rates and thickness increase in local topographic troughs and decrease on local peaks (Reneau et al., 1992), analogous to macro- and regional-scale accumulation of sediment in basins. The rapid early accretion model of Reneau et al. (1992), where differential varnish accumulation causes an overall smoothing of the lithologic micro-surface, could explain some instances where higher varnish accumulation rates are found on younger geomorphic surfaces (Liu and Broecker, 2000; Krinsley et al., 2012; Spilde et al., 2013).

THE RELATIONSHIP BETWEEN DESERT VARNISH AND DESERT PAVEMENT

Based on reconnaissance images (field photographs, and visible wavelength satellite imagery), the older geomorphic surfaces in our study area generally have a darker overall color index, which is likely due to a greater degree of desert varnish and desert pavement development. A relatively smooth and well compacted macroscopic desert/stone pavement surface is often associated with moderate to heavy varnish development on coarse gravels. The way that a desert pavement forms has implications for the validity of using varnish as a chronometer. A classical hypothesis regarding desert pavement formation invokes the idea that a geomorphic surface can experience overall deflation, where the coarser interlocking clasts in a pavement have progressively become exposed, agglomerated, and compacted at the surface of the Earth over a long period of time, all while finer sediment is winnowed via

aeolian processes. In this case, a lithologic surface coating of varnish would not be a valid chronometer, since not all of the clasts were exposed at the surface when it first formed. An alternative hypothesis is the "born at the surface" model (Wells et al., 1985; 1995; McFadden et al., 1987), where the coarse, interlocking surficial clasts have been exposed continuously since formation of the geomorphic surface commenced. The "born at the surface" model explains data for pavements with exposure ages similar to those of proximal bedrock source material (Wells et al., 1995). Under this model, any lithologic surface coatings have potentially accumulated continuously over the entire age span of the surface. In that case, the overall varnish development could be a chronometer that records the entire life span of the surface.

Regardless of the pavement formation model, other processes must also be considered. Bioturbation by plants and animals can disrupt the protracted development of substantial desert varnish coatings and associated pavement surfaces. It is also possible that the varnish can undergo diagenesis, including dissolution, and this might always be a state of disequilibrium (Garvie et al., 2008), analogous to erosive forces acting during aggradation in sedimentary basins. While these complications might hinder attempts to see varnish accretion as a chronometer on the microscopic scale, the remote sensing data and methods that we employ here take into account a much broader sample of the overall geomorphic surface. Desert varnish accretion, coupled with desert pavement development, might result in specific characteristics of the geomorphic surface that can be observed and quantified via the synoptic view that airborne hyperspectral imagery provides.

SPECTROSCOPY OF CLAYS AND OTHER RELEVANT MINERALS

The ability to identify submicroscopic clay minerals via spectroscopy is intrinsic to this research. Electromagnetic energy from the Sun interacts with the crystal structure of minerals to produce diagnostic spectral features seen in infrared reflectance and emission spectroscopy. Furthermore, clays are often present in significant abundance on planetary surfaces, yielding strong signals that can be rigorously quantified and interpreted (e.g., Michalski et al., 2006; Ehlmann et al., 2009).

The clay minerals montmorillonite and illite were identified in significant abundance within desert varnish from southern California, using laboratory infrared absorbance spectra (Potter and Rossman, 1977). Montmorillonite is part of the di-octahedral smectite group, which has the general chemical formula: $(½Ca,Na)_{0.7}(Al,Mg,Fe)_4[(Si,Al)_8O_{20}](OH)_4 \cdot nH_2O$ (Deer et al., 1992). The montmorillonite in desert varnish from southern California was c. 50% of a mixed-layer clay component that also included illite (Potter and Rossman, 1979a). Illite has spectral features nearly identical to those of montmorillonite in thermal infrared emissivity spectra (Figure 1a in Michalski et al., 2006), so in this research we are focusing primarily on montmorillonite's spectral features to guide our interpretations of clay mineral content in desert varnish.

Clays and all other silicate minerals display the most prominent spectral feature, the Reststrahlen band, which appears in the thermal wavelength regime (λ = 8-15 μm). The Reststrahlen band occurs as a minimum in emissivity spectra, and is due to Si-O asymmetric stretching vibrations in the crystal lattice (Thomson and Salisbury, 1993). The exact spectral position of the Reststrahlen band is dependent on the degree of silica tetrahedra polymerization in a crystal lattice (Launer, 1952). For the nesosilicate minerals (and the rocks

they form) that have a lower degree of Si-O polymerization (e.g., olivine, garnet, dunite, basalt), the Reststrahlen band generally occurs at longer wavelengths. In contrast, silicates (and rocks) with higher polymerization (e.g., quartz, feldspars, granite, rhyolite) have a Reststrahlen band at shorter wavelengths (see Figure 2 in Hook et al., 2005). The phyllosilicate clay minerals in the smectite group (and kaolinite) have intermediate silica polymerization. These clays have a major spectral feature at a position somewhere in the range 9.1-9.6 μm (Keller and Pickett, 1950; Hunt et al., 1950; Launer, 1952; Farmer, 1974; Bishop et al., 2002a; Frost et al., 2002; Michalski et a., 2006; Bishop et al., 2008). The 9.1-9.6 μm feature is due to Si-O stretching (Bishop et al., 2002a; Frost et al., 2002; Michalski et a., 2006), and therefore represents the Reststrahlen band position for these minerals.

Highly polymerized tectosilicate spectral features are likely to be observed in remote sensing spectra, and they may overlap with features from clay minerals. In general, spectral data must be evaluated on the basis of considering mixtures of minerals that might possibly have spectral features at similar, overlapping, or identical wavelengths. Some of the common tectosilicate minerals were significantly represented in the desert varnish substrate lithology (detrital clasts) from our study area. Figure 2 illustrates that both quartz and montmorillonite clay have a spectral feature near 8.8 μm (also see Figure 5 in Michalski et al., 2006; Bishop et al., 2008). For quartz, this is the primary feature, but for clays, this is a minor, secondary feature. Quartz also has a diagnostic spectral feature, a very distinct doublet (or two Reststrahlen bands, as described by Thomson and Salisbury, 1993) with emissivity minima at 8.4-8.6 μm and 8.8-9.0 μm (Figure 2 in this study; Figure 1 in Conel, 1969; Figure 4 in Christensen et al., 2000; Figure 5 in Michalski et al., 2006). Potassium feldspar has prominent

spectral features at c. 8.7, 9.2, 9.5, and 9.9 μm (Figure 2 in this study; Figure 1b in Thomson and Salisbury, 1993; Figure 5 in Michalski et al., 2006).

The minor spectral features at longer wavelengths are less important to this research. Smectite clays have minor features from 10-13 μm (Keller and Pickett, 1950; Hunt et al., 1950; Launer, 1952), due to aluminum/magnesium/iron hydroxide bending vibrations (Farmer, 1974; Sposito et al., 1983; Bishop et al., 1994; Bishop et al., 2002a; 2002b; Frost et al., 2002; Michalski et al., 2006; Bishop et al., 2008). Other clays (kaolinite and illite) have minor spectral features from 12-13 μm (Keller and Pickett, 1950), as does quartz (Figure 2 in this study; Keller and Pickett, 1949; Hunt et al., 1950; Launer, 1952; Lippincott et al., 1958; Lyon, 1965; Michalski et al., 2006), and feldspars (Thomson and Salisbury, 1993). Tectosilicate spectral features from 12-13.5 μm are due to a symmetric stretching mode in the Si-O molecules, and various Si-O-Al combinations for feldspars (Thomson and Salisbury, 1993). We did not consider minor features from clays at longer wavelengths, partly because some of the other studies were based on transmission spectra, which can sometimes be more revealing than emission spectra (e.g., Michalski et al., 2006).

Furthermore, even though the manganese and iron oxides (birnessite and hematite, respectively) are significant components in desert varnish, we also gave these metal oxides little consideration, because in the wavelengths that our data covered (λ = 7.6-13.2 μm) their infrared absorbance spectra are relatively flat (Figures 3 and 6 in Potter and Rossman, 1979a; Figure 14 in Potter and Rossman, 1979b), and lack any fundamentally diagnostic spectral features.

SPECTRAL MIXTURE MODELS

The combination and mixing of spectral features shows how progressively heavier coats of desert varnish will alter the spectrum of a substrate lithology, including changes in band depth and positions of minima. When a lithologic mixture includes a greater fraction of a certain mineral, the wavelength positions where distinct features occur for that mineral will usually display a greater depth in spectra. When a quartz-rich substrate has a coating of varnish, the minimum in emissivity spectra shifts to a longer wavelength (Gillespie et al., 1984), due to the clay mineral's lower degree of silica polymerization and resultant influence on the Reststrahlen band position. In laboratory and field spectra, spectral features for quartz are progressively modified and obscured by an increasing varnish coating. If the varnish is present in sufficient quantity, its own spectral features, which bear a striking resemblance to those of clay minerals, will completely mask those of the substrate (Figure 13 in Kahle, 1987; Figure 9 in Bartholomew et al., 1989; Rivard et al., 1993).

The results mentioned above from previous research on spectroscopy of desert varnish coatings can be recreated by modeling the spectral effect of mixing clay with tectosilicate minerals. We created linear spectral mixture models using laboratory thermal emission spectra (Christensen et al., 2000), to exemplify the results from previous research (Figure 2). These models also helped guide our own hypotheses on how desert varnish might alter remote sensing spectra from our study area. Linear mixture models of laboratory spectra are accurate in the wavelength range that includes Reststrahlen band positions if surface scattering is prevalent, a condition that is met if the particle sizes of the single mineral components are much larger than the wavelengths in measured spectra (Thomson and Salisbury, 1993). To represent a typical varnish substrate lithology (detrital clasts) from our

study area, we mixed spectra from three common tectosilicates in roughly equal relative abundances: 33% quartz (125-2000 μm), 34% andesine plagioclase feldspar (710-1000 μm), and 33% microcline potassium feldspar (710-1000 μm). Spectral features from each of the three tectosilicates, the deepest of which are in the range 8.5-9.2 μm, are represented in this synthetic "granite" spectrum (Figure 2A). To represent the clay minerals found in desert varnish, we used a spectrum from montmorillonite, which was taken from a pressed pellet (Cooper and Mustard, 1999, noted that clay crystal aggregates behave spectrally like larger particles). As more clay is added to the "granite" substrate, the spectral features of the clay alter and ultimately conceal the granite's spectral features. The clay's major spectral feature at 9.36 um begins to dominate the spectrum at adding as little as 33% to the mixture, and deepens substantially as more is added, representing a heavy coating of desert varnish (Figure 2B).

Based on the results from previous research and from our own spectral mixture modeling, we expect to see in our data a spectral feature in the range 9.1-9.6 μm, due to clay minerals in desert varnish. Different minerals and materials can have spectral features at similar spectral positions (Figure 13 in Launer, 1952), creating some ambiguity when attempting to interpret remote sensing observations. We need to take into account the chemical aspects of other minerals that are known to be present, as well as variation in the physical aspects of lithology (e.g., clast size and topographic surface roughness), and other natural features (e.g., vegetation), that can also contribute to the spectral emission signal. Even if the signal is present and real, we consider various ways for why it changes on the geomorphic surfaces of varying ages and characteristics.

METHODS

Some of the text in the following subsections is copied verbatim from Chapter 2 of this thesis (on remote sensing of the Lavic Lake fault). The wording is identical, or almost identical, because the sensor calibration procedure and the image data processing sequence were the same for the two study areas.

Thermal Hyperspectral Airborne Imagery Acquisition

We collected thermal hyperspectral airborne imagery on 24 September 2015 (at c. 10:45 am to 10:55 am, Pacific daylight savings time) using Mako, a "whiskbroom"-type sensor developed and operated by The Aerospace Corporation. The Mako sensor measures surface radiance in the thermal regime at 128 bands (Hall et al., 2011). For the data used in this study, the wavelength range was 7.6-13.2 μm, with one-meter ground sampling distance (or image pixel resolution), from a flight at 6000 feet above ground level (c. 6800 feet altitude). For the terminology used herein regarding the hyperspectral image data from the Mako whiskbroom sensor, each single "whisk" (or linear track) is a single data cube, so the words "whisk" and "data cube" are used interchangeably. When multiple data cubes (or whisks) are concatenated into a larger image, the set of combined data cubes can be called a "super cube." The full hyperspectral imagery data set presented here consisted of two super cubes (or image swaths) with parallel, adjacent flight lines that were flown in opposing azimuthal directions. The two neighboring super cubes were combined for greater spatial coverage in a single scene. Although a set of combined super cubes can still be called a super

cube, when the two super cubes used here are combined into a single image, we call this the "complete image scene."

The complete image scene covered portions of both the Mission Creek and Banning strands of the southern San Andreas fault. The complete image scene covers a rectangular area, c. 6.1 km along the flight path (roughly parallel to and centered on the Mission Creek strand), and c. 4.7 km wide. The complete image scene consists of 114 whisks total, with 57 whisks in each of the two parallel, adjacent flight swaths. The spatial extent of a single whisk relative to the complete image scene can be seen in Figure 3: in the saw tooth pattern along the sides of the image swath (sides that are parallel to the fault traces), the tip of each tooth is the boundary between two whisks. Two adjacent whisks generally have a small amount of overlap, and for this data, the two parallel, adjacent swaths also have a small amount of overlap.

Mako Sensor Calibration

The Mako airborne hyperspectral infrared sensor underwent radiometric and wavelength calibration. For radiometric calibration, two onboard blackbody sources were observed immediately before and after the scene was acquired. These were stabilized at different temperatures that spanned the expected radiance values of the scene. A linear relation between the known blackbody radiance input and the digital counts output was assumed so that the sensor response could be modeled with multiplicative gain and additive offset terms. The gain and offset terms for the pre- and post-collection calibrations were then time-interpolated to match the actual collection time of the data.

The wavelength calibration was done by observing blackbody sources covered by National Institute of Standards and Technology (NIST) traceable transparent polymer films (with calibrated absorption features), and performing a least-squares fit across the full extent of the focal plane array. For more detailed descriptions of the calibration processes, see Hall et al. (2011) and Buckland et al. (2017).

Hyperspectral Airborne Imagery Data Processing

All of the steps in the following image processing sequence, unless otherwise specified, were completed using the Environment for Visualizing Images Software, version 4.8 (ENVI, Exelis Visual Information Solutions, Boulder, Colorado). We began with data cubes of airborne thermal hyperspectral imagery that had undergone radiometric and wavelength calibration, bad pixel replacement, and spectral smile removal. We first concatenated the 114 data cubes (whisks) that made up the complete image scene into a single "supercube." After that, we could carry out the subsequent processing steps in bulk.

For the hyperspectral image data presented here, we had to remove the first ten bands that covered wavelengths from 7.56-7.96 μm because they were dominated by noise. We proceeded to use bands 11-128 (118 total), with wavelengths from 8.01-13.15 μm. We performed an in-scene atmospheric compensation (ISAC algorithm from Young et al., 2002), setting the regression pixels to maximum hit, the fitting technique to normalized regression, and using for the noise equivalent spectral radiance (NESR), the median value of the super cube. Then, we used a minimum noise fraction (MNF) transformation (Green et al., 1988; note that it is called a "maximum noise fraction" in that paper; also, see Lee et al., 1990) to

identify noise or data artifacts in the imagery. A gradation perpendicular to the flight direction (across track) was present near the edges of each individual data cube, so we discarded this spurious spectral signal in an MNF inverse transformation.

Next, we converted the data from at-sensor radiance to emissivity with the emissivity normalization method (Kealy and Hook, 1993). With the emissivity image, we could extract spectra of the geomorphic surfaces for analyses, since we were characterizing spectra in relation to known surface ages (Table 1).

Before extracting the emissivity spectra, we needed to mask younger, ephemerally active channels that cut into the older surfaces. To achieve this, we used a digital elevation model (DEM) with 1.5 m spatial resolution (created by Ryan Gold) to first calculate from the DEM a slope map, and then use the slope map to mask areas with high slopes (which represent relatively steep walls of the younger channels). The parameters for creating the slope mask were topographic kernel size of 5 to create the slope map (with slope in degrees), and we then masked pixels with a slope value greater than 3 degrees. The slope mask was then intersected with the digitized polygons that represented the mapped geomorphic surfaces with known ages (Figure 4).

To produce a single representative spectrum for each distinct geomorphic surface, we averaged (arithmetic mean) a random sampling for 1% of the total number of pixels within each surface's digitized boundaries. We performed the 1% random spectral sampling a total of five times to capture statistical variability in the spectral data. We also removed the continuum from all of the representative emissivity spectra, so that they could be compared against one another with a normsalized baseline (i.e., with respect to the band depth/strength at wavelength positions for spectral features of interest, see Clark and Roush, 1984). From

herein, we will refer to any hyperspectral airborne imagery emissivity spectra as “airborne remote sensing spectra.” The airborne remote sensing spectra were plotted after being smoothed with a moving average over a three band interval (Figure 5).

We hypothesized that the older surfaces contain a greater fraction of clay minerals (in varnish), and will therefore display a greater band depth somewhere in the wavelength range where the Reststrahlen bands are predicted to occur for clay minerals, which is 9.1-9.6 μm (Bishop et al., 2002a; Frost et al., 2002; Michalski et a., 2006). We chose to focus on the wavelength position at 9.16 μm, because in our airborne remote sensing data, the greatest number of spectra had an emissivity minimum at 9.16 μm. Figure 6 is a plot of airborne spectra band depth at 9.16 μm versus surface age. Whether or not this spectral feature at 9.16 μm corresponds to the fraction of clay minerals present or not will be discussed later, but we analyzed the order of increasing/decreasing relative band depth based on this wavelength position.

If we assume the above hypothesis, then older surfaces will have increased band depth at 9.16 μm. In the following Results section, we will use the phrases “in position” and “out of position” to describe whether the band depth at 9.16 μm for each spectrum is in sequence with the others with respect to the sequence of known surface ages (e.g., a spectrum for the oldest geomorphic surface would be “in position” if it displayed the greatest band depth at 9.16 μm, a spectrum for the second oldest surface would be “in position” if it displayed the second greatest band depth at 9.16 μm, etc.). Interpretations of those results will be discussed in a later section.

Ground Truth Field Work

We also needed field measurements to compare with our airborne remote sensing spectra interpretations. We did field work in the study area from March 2017 through May 2017 to collect ground truth information. We arbitrarily chose from two to four sites located on each geomorphic surface with known age to collect field data. At each site, a square plastic frame, one meter on edge, was placed on the ground to collect data within a confined area that represented the hyperspectral airborne imagery pixel size. First, we took two types of field photographs at each sample site: 1) an overhead (bird's eye) view of the sample square meter (or sample area field photograph); and 2) an overview perspective of the geomorphic surface (or site overview field photograph). To describe the lithologic characteristics of each sample square meter, we collected petrologic data, including primary mineralogy and textures of detrital surface clasts that make up the alluvial fan deposits. We used a combination of field observations and the sample square meter photographs to estimate the dominant (>50% relative abundance) clast size ranges, for sizes down to 1 mm mean diameter (when possible), using percentage diagrams for estimating composition by volume (see Appendix 3 in Compton, 1985). We also collected up to ten lithologic sample chips from most of the field sites.

To assess the degree of desert varnish, and desert pavement development, we established a numerical scale to give each a score, from 1-4, for each sample site (the scores are not single values, but ranges). In the numerical scale, a higher number is a greater degree of development, as follows: 1 = absent/rare, 2 = light/weak, 3 = moderate, and 4 = heavy/strong. Varnish scoring was based mainly on darkening color, and pavement scoring was based mainly on smoothness and compaction (compaction assessed by placing the ball

of a booted foot on the surface and twisting to see how easily clasts broke free from their interlocking arrangement). We acknowledge that these numerical scores are subjective, but our experience in the field allowed us to develop a sense of varnish and pavement development in a relative sense to other sites visited and analyzed.

To quantify the variable presence of vegetation between the surfaces, we estimated the average spacing between desert scrub bushes or other plants, as a proxy for vegetation abundance/density. We also collected several vegetation leaves and branches from a few of the sites.

Rock Area Fraction: Analysis Using Ground-based Field Photographs

We also assessed whether clast size variation existed between surfaces with another independent method. Larger clasts are less susceptible to induced motion, and therefore are more stable and conducive to extended periods of varnish development. Along these lines, we were interested in deriving a quantitative measurement for the fraction of clasts that were above some size threshold. We defined this quantity as the "rock area fraction." Since the terms "rock, sediment, and grains" are undefined with respect to size, we established a definition to quantify our data. To decide which clasts qualify as "rocks," we chose a threshold size of 2.5 cm mean diameter. The edge of the plastic frame that was used to define each sampling area had a thickness of 2.5 cm, so this served as a consistent reference scale in all of the field photographs. With a value defined for size cutoff, we could determine the areal percentage of each sample square meter that was occupied by the larger clasts that were more likely to have a greater degree of varnish development. The remaining lithologic

detrital material, with sizes below 2.5 cm, represented clasts that were generally not large enough (i.e., not kinematically stable) for protracted varnish development.

To complete this analysis, we used the ground-based field photographs of the sample square meter sites. On a printout of each photograph, clasts that were within the sample square meter, and above the size threshold of 2.5 cm, were outlined by hand with vellum tracing paper on a light table (these larger outlined clasts would be included in the "rock" fraction). The tracing paper sheets were scanned to digital image files, and the digital image files were then processed with ImageJ software (Schneider et al., 2012). With ImageJ, we established the scale size in each image, automatically filled all of the clast outlines that were traced, then calculated the fraction of the sample square meter area occupied by the filled clast outlines (i.e., the integrated area occupied by all of the clasts with mean diameter greater than c. 2.5 cm). The remaining fraction of unfilled area was then smaller clast sizes that would not be large and stable enough for protracted varnish development. This analysis allowed us to quantify the fractional area (in percent) of a single airborne remote sensing pixel that was available for varnish development. Note that the total rock area fractions that we calculated are minimum values, because our analysis was inherently subjective, and it is possible that we did not capture every single clast that exceeded the size threshold.

Ground-based Spectra

To observe spectral variation among the geomorphic surfaces on a smaller scale, we used a hand held field spectrometer to directly measure lithologic spectra from the exposed, top (and sometimes varnished) sides of single clast surfaces. In addition to measuring the

single clast lithologic spectra, we also measured spectra from samples of finer, unconsolidated lithologic detrital material (from herein, we will refer to these as "sand" spectra, where "sand" does not imply a technical definition of clast size), and vegetation samples, since these materials were included in noteworthy abundance in our study area. The apparatus we used was an Agilent 4100 ExoScan™ portable Fourier Transform Infrared spectrometer (spot size: 3-5 mm), which measures diffuse reflectance by active source. From herein, we will refer to any spectral measurements that we made with this apparatus as "ground-based spectra." Some of the ground-based spectra were collected in situ, but due to difficulties in the field (e.g., inability to transport all of the equipment to distal field sites, and/or equipment failure), most were collected later, on samples that we brought back. We collected up to ten ground-based spectra from a variety of materials at each site (Table 2).

To compare the general shape and wavelength positions of prominent spectral features between airborne remote sensing and ground-based spectra, the ground-based reflectance spectra were converted to emissivity using Kirchhoff's law. In a general form, Kirchhoff's law states that reflectance and emissivity sum to unity (Robitaille, 2009). The ground-based spectra were diffuse reflectance measurements, which is similar to a conical-hemispherical measurement (see Case 6 from Table 2 in Schaepman-Strub et al., 2006). If seeking quantitative spectral measurements, directional-hemispherical reflectance spectra are usually considered acceptable (assuming isothermal conditions) for converting to emissivity via Kirchhoff's law (Salisbury and Walter, 1989; Salisbury et al., 1994). However, the simple conversion offered by Kirchhoff's law is not generally considered appropriate for converting some other types of reflectance spectra to emissivity (Christensen and Harrison, 1993). Still, other types of spectral reflectance measurements converted to emissivity via

Kirchhoff's law do generally maintain the same general spectral shape as direct spectral emissivity measurements (Figure 3b in Christensen and Harrison, 1993; Figure 4 in Christensen et al., 2000). We did not assume that the ground-based spectra were quantitative to begin with, and since we were mainly concerned with the qualitative aspect of this analysis, we accepted the error involved in converting ground-based diffuse reflectance spectra to emissivity via Kirchhoff's law.

Finally, all of the ground-based spectra were plotted for each site, along with the site average (arithmetic mean), to show how spectra from a mixture of materials within the hyperspectral airborne imagery's pixel size might manifest as a single remote sensing spectrum. From herein, when we refer to any ground-based spectra, we are referring to the single representative site average, unless otherwise specified.

RESULTS

Airborne Remote Sensing Spectra

The results here will be presented according to their respective geomorphic surface names (Table 1). We separated the airborne remote sensing spectra into two groups: from surfaces that are located upstream, and downstream, of the southern San Andreas fault, Mission Creek strand. The spectra were then further subdivided by surface age. The R^2 correlation coefficient between all airborne spectra band depth at 9.16 μm and surface age is 0.59 (Table 3).

For the upstream sets of spectra (Figure 5), the oldest surface, Qt0 (>95 ka), is in position (greatest band depth at 9.16 μm) for four of the five subsets. The two youngest surfaces, Qt3 (13 ka) and Qt4 (<11 ka), are together in position for all five subsets, with the caveat that Qt3, not Qt4, has the least depth for four of the five subsets. In all five of the sampling sets, Qt2 (74 ka) is always out of position, with a greater 9.16 μm band depth than Qt1 (87 ka).

For the downstream sets of spectra (Figure 5), the oldest surface, C0 (>95 ka), is in position (greatest band depth at 9.16 μm) for three of the five subsets, and we note that for the remaining two sets, C2f (26 ka) has the greatest band depth. The youngest surface in the downstream group, C3 (13 ka), is in position (least band depth at 9.16 μm) for all five of the subsets. The downstream group of surfaces are in complete ideal sequence (according to our increasing-band-depth-with-age hypothesis) for two of the five subsets.

Ground Truth Field Work

Primary Mineralogy and Lithologic Textures of Detrital Surface Clasts

Surficial clasts at all of the sample sites had generally similar primary mineralogy and lithologic textures. Quartz/alkali feldspar/plagioclase (QAP) clast compositions of phaneritic (individual crystals generally 1-5 mm) igneous rocks included granite, granodiorite, quartz monzodiorite, and quartz monzonite. Some other types of clasts and/or textures included conglomerate/breccia, gneiss, schist (rich in amphibole and/or biotite mica), pegmatite, porphyry with feldspar megacrysts, and fine-grained mafic (pyroxene-rich)

rocks. At a site on the oldest downstream surface, C0p2 (>95 ka), we noted that the lithologic substrate for some of the most heavily varnished clasts was a mafic schist.

Clast Size Measurements

The results for the dominant (>50% relative abundance, down to 1 mm) clast size ranges are shown in Figure 7. We do not observe any trends, such as a general monotonic increase or decrease, between the dominant clast size ranges and surface age. The R^2 correlation coefficient between mean of dominant (>50%) clast size ranges and surface age is 0.10 (Table 3). The largest range was recorded at a site on the youngest downstream surface, C3p2 (13 ka). In the field, we also observed fewer larger clasts (>30 cm long axis) at a site on one of the older upstream surfaces (Qt1, 87 ka, see site overview field photograph for Qt1p2, Figure S8 in the Supplemental Items).

Desert Varnish and Desert Pavement Development Scores

The scores for degree of desert varnish and desert pavement development are plotted in Figures 8 and 9, respectively. For both sets of scores, we observe a general monotonically increasing trend between score and surface age, with the lowest scores for the youngest surfaces, and the highest for the oldest. The Spearman's rank correlation coefficients (used for categorical variables, see Simspon, 2015) between varnish and pavement scores, and surface age are 0.90 and 0.90, respectively (Table 3). For the downstream surfaces, the general monotonic increase in desert varnish and desert pavement scores is interrupted by a

decline in score for the site C2fp4 on the C2f (26 ka) surface. From our field inspections, we observed that varnish was absent/rare even on larger, more stable boulders, on the younger surfaces on either side of the fault.

Vegetation Abundance

The estimates for average vegetation spacing are shown in Figure 10. There is a generally monotonic increasing trend between average vegetation spacing and surface age. The R^2 correlation coefficient between vegetation spacing and surface age is 0.34 (Table 3).

Additional Field Observations

On the younger upstream surfaces (Qt4, <11 ka, and Qt3, 13 ka), we also observed meter scale bar and swale (hummocky) topography, which was composed of larger clasts (10-20 cm long axes) concentrated on channel bars (see field photographs for Qt4p2 (which was a site directly located on one of the channel bars with larger clasts), Qt3p1, and Qt3p2, Figures S2, S3, and S4 in the Supplemental Items).

At the upstream site Qt1p2 (87 ka), we observed a conspicuous higher relative abundance of red-orange micro- or cryptocrystalline iron-oxide minerals (likely included hematite and goethite; see field photographs for Qt1p2, Figure S8 in the Supplemental Items). It is possible that many of the clasts at the Qt1p2 site were flipped over, because an orange coat on the buried bottom of varnished clasts is often present due to iron oxide formation at soil or sub-soil level (Figures 2 and 3 in Engel and Sharp, 1958; Potter and

Rossman, 1977; 1979a). On the oldest upstream surface Qt0 (>95 ka), we observed the best examples of extremely well-developed, smooth, resistant, heavily varnished desert pavement (see field photographs for Qt0p2, Figure S10 in the Supplemental Items).

At the downstream site C2fp1 (26 ka), we noted a distinct, light pink oxidation on clasts (see sample square meter field photograph for C2fp1, Figure S15 in the Supplemental Items). At the site C0p1 (>95 ka) on the oldest downstream surface, we noted that the dimensions for broader areas with the greatest degree of varnish and pavement development, had their longest dimension parallel to the direction of channel drainage (see site overview field photograph for C0p1, which was taken facing southwest, parallel to the channel drainage direction, Figure S25 in the Supplemental Items). In a view perpendicular to the drainage direction, more vegetated areas were observed in channel rills. The implication of these observations is that channel bars of larger clasts (e.g., gravel/cobbles/boulders) could have ended up being the most heavily varnished and strongly developed pavement surfaces.

Rock Area Fraction

The results for the rock area fraction (minimum, %), calculated for each of the 1-m^2 field sampling sites using image processing software, are shown in Figure 11. There is no general monotonic increase or decrease between the rock area fraction and surface age, and the R^2 correlation coefficient is 0.00 (Table 3). This implies that, for our airborne remote sensing data, the fraction of area for a single pixel that was at least fundamentally available for varnish development did not increase for older surfaces.

However, we noted that for the upstream surfaces (upper panel in Figure 11), the youngest and oldest surfaces had sites with the highest and lowest rock area fractions, respectively: Qt4p2 (<11 ka, a site directly located on one of the channel bars with larger clasts, Figure S2), and Qt0p2 (>95 ka, Figure S10). For the downstream surfaces (lower panel in Figure 11), the sites C2p3 (74 ka, Figure S21) and C2fp4 (26 ka, Figure S18) have the highest and lowest rock area fractions, respectively. Additionally, for the downstream surfaces, the two sites (for which rock area fraction was measured) on the youngest surface (C3, 13 ka, Figures S11 and S12), both have rock area fractions that are greater than any of those from the three sites on the oldest surface (C0, >95 ka, Figures S25-S27). Furthermore, the upstream and downstream surfaces that have the greatest difference for rock area fraction between sites are Qt4 (<11 ka, Figures S1 and S2) and C2 (74 ka, Figures S19-S22), respectively. The upstream and downstream surfaces that have the least difference for rock area fraction between sites are Qt3 (13 ka, Figures S3 and S4) and C3 (13 ka, Figures S11 and S12), respectively. See field photographs for all of the sites referenced above in the Supplemental Items.

Ground-based Spectra

Ground-based spectra for all 27 field sites, along with accompanying sample square meter, and site overview field photographs, are in the Supplemental Items, and a summary of which materials were measured at each site is in Table 2. Figures 12 and 13 are two examples of the ground-based spectra for the sites Qt4p1 (<11 ka) and C0p1 (>95 ka), respectively. Some additional ground-based spectra that are relevant to the discussion of clast

size effects are from the following sites (see Table 2, and the Supplemental Items): Qt4p1 (<11 ka; Figure 12), spectra 1-5; C3p1 (13 ka, Figure S11), spectra 1,8,9; C3sand (13 ka, Figure S13), spectra 1-10; and C2fp4 (26 ka, Figure S18), spectra 4-9. Ground-based spectra of relevance to the consideration of vegetation effects include: Qt4p1 (<11 ka; Figure 12) spectra 6-10; Qt2p2 (74 ka, Figure S6), spectrum 1; and C3veg (13 ka, Figure S14), spectra 1-4. Note that both of these material variation considerations were covered at the upstream site Qt4p1 (<11 ka, Figure 12).

For the ground-based averaged spectra, a first order observation is that measurements from the youngest surfaces (see sites from Qt4 (<11ka) and C3 (13 ka), Figures S1, S2, and S11-S14 in the Supplemental Items) can be relatively flat in the range 9-10 μm, or they can contain a prominent, deeper feature at 9.30 μm. Compare this to ground-based spectra for the oldest surfaces (see site C0p1 (>95 ka) in Figure 13, sites from Qt0 and C0 (both >95 ka), Figures S9, S10, and S25-S27 in the Supplemental Items), which all contain a prominent, deeper feature at 9.30 μm. As stated previously, the ground-based spectral measurements are not quantitative, so we did not expect to see any correlation with surface age for the band depth of any specific features. For completeness, though, the R^2 correlation coefficient between ground-based spectra band depth at 9.30 μm and surface age is 0.04 (Table 3).

The feature at 9.30 μm in ground-based spectra is at odds with the 9.16 μm feature in airborne spectra. Spectra from the oldest surfaces are generally the most representative for maximum band depth at either of the respective wavelength positions, so we plotted a few of the oldest typical airborne and ground-based spectra together on the same axes to illustrate the systematic difference in shape and position of minimum (Figure 14).

DISCUSSION

In our airborne remote sensing spectra, we observed a general increase in band depth (also known as band strength or spectral contrast) of the 9.16 μm feature with age. As reported above in the Results section, some of the remote sensing spectra for geomorphic surfaces display a band depth at 9.16 μm that is in position with respect to the relative band depth for older/younger surfaces. For example, the upstream oldest surface Qt0 (>95 ka) has the greatest band depth at 9.16 μm for four of the five subsets, and the downstream oldest surface C0 (>95 ka) has the greatest band depth for three of the five subsets (Figure 5). The two youngest upstream surfaces, Qt3 (13 ka) and Qt4 (<11 ka), together have the least band depths for all five subsets, and the youngest downstream surface C3 (13 ka) has the least band depth for all five subsets (Figure 5). Furthermore, the downstream surfaces are in complete ideal sequence (band depth at 9.16 μm strictly increases with age) for two of the five subsets (Figure 5). However, there are a number of remote sensing spectra for surfaces that are out of position. Along with airborne spectra band depth at 9.16 μm, the other parameters with correlation coefficients >0.30 include desert varnish and desert pavement scores, and vegetation spacing (Table 3 and Figure 15).

The Effect of Petrology

The likely bedrock sources for alluvial/fluvial deposition in the Indio Hills are in the Little San Bernardino Mountains located immediately to the north east, which generally consist of intrusive crystalline rocks (hornblende diorite-gabbro, and various granitoids), and

metamorphic rocks, various politic and mafic schists (Dibblee, 2008; Lancaster et al., 2012). We expected similarity of clast compositions between surfaces, because they are all alluvial/fluvial deposits (now sets of terraces) along the same source drainage through Pushawalla Canyon. There has only been about 2 km of displacement of the Pushawalla Canyon drainage in the past c. 100 kyr (Blisniuk and Sharp, 2014), so it is unlikely that the eroding bedrock source for the system has shifted to a drastically distant and different source during that time. Therefore, we rule out fundamental petrologic differences in clasts as a reason to explain the spectral variation between surfaces.

The Effect of Other Minerals

We examined the effect of other minerals by comparing the airborne remote sensing (Figure 5), ground-based averaged (Figures 12, 13, 14, Table 2, and Supplemental Items), and the library laboratory spectra (from Christensen et al., 2000; Figure 2 in this study). As discussed previously, the spectral emissivity spectral features that we expected to see were at the following wavelength ranges (in μm, with the attributable mineral(s) in parantheses): 8.2-8.6 (quartz+microcline+andesine), 8.6-9.0 (quartz+microcline+andesine), 9.0-9.4 (microcline); 9.2-9.4 (montmorillonite clay); two separate and distinct features from 9.4-10.0 (microcline+andesine), and two separate and distinct features from 12.4-13.0 (quartz).

Nearly all of the airborne remote sensing and ground-based averages have prominent spectral features at the following wavelengths (μm): 8.2-8.6, 8.6-9.0, two separate and distinct features from 9.4-10.0, and two separate and distinct features from 12.4-13.0 (Figures 5, 12, 13, 14, and Supplemental Items). We correlate these features to the following

corresponding features observed at wavelengths (μm) for specific minerals in the library laboratory spectra, and their synthetic "granite" mixture spectrum (Figure 2): 8.2-8.6 (quartz+microcline+andesine), 8.6-9.0 (quartz+microcline+andesine), two separate and distinct features from 9.4-10.0 (microcline+andesine), and 12.4-13.0 (quartz).

For the Reststrahlen band of clay minerals, the wavelength range of interest is 9.1-9.6 μm (Keller and Pickett, 1950; Hunt et al., 1950; Launer, 1952; Farmer, 1974; Bishop et al., 2002a; Frost et al., 2002; Michalski et a., 2006; Bishop et al., 2008). But we see a particular difference between airborne remote sensing and ground-based average measurements in the range 9.1-9.6 μm. In the majority of the airborne remote sensing spectra (mainly from older surfaces), a distinct spectral feature is present with a minimum at 9.16 μm, and the band depth of that feature generally increases with surface age (Figures 5, 6, 15, and Table 3).

In the majority of the ground-based averaged spectra (Figures 12, 13, 14, and Supplemental Items), a distinct spectral feature is present with a minimum at 9.30 μm. As expected, this 9.30 μm ground-based feature does not generally increase in absolute band depth with surface age in site-averaged spectra, because the ground-based spectrometer is not quantitative (as discussed previously), and furthermore, broad variations exist for the microscopic surface roughness of lithologic sample chips measured, as well as their temperatures at the time of measurement. Yet, it appears that some of the older surfaces might generally exhibit a greater band depth at 9.30, if measured relative to the band depth of the quartz feature from 8.2-8.6 μm.

The library laboratory spectrum for montmorillonite clay (Figure 2B) has its Reststrahlen band at 9.36 μm, and there is another laboratory spectrum from montmorillonite

(Figure 5 in Michalksi et al., 2006) with a Reststrahlen band at 9.33 μm. Considering these observations, the ground-based 9.30 μm feature correlates more closely than the airborne 9.16 μm airborne feature to the 9.36 μm library laboratory montmorillonite Reststrahlen band. The difference in the emissivity minimum at 9.16 μm for airborne spectra and 9.30 μm for ground-based spectra is real and unexplained (Figure 14), so we do not assert that this aspect is unimportant. However, the difference does not completely rule out that the 9.16 μm remote sensing feature could be from clay minerals, so we considered some reasons why the two data sets do not agree.

Our analysis is complicated by the following spectral features from other minerals that overlap with the clay features: the laboratory synthetic "granite" spectrum has a spectral feature centered at about 9.2 μm from microcline and quartz (Figure 2). The synthetic "granite" spectrum has a distinct feature at 8.8 μm that directly overlaps with a feature at the same position from the library laboratory montmorillonite clay spectrum (Figure 2B). Additionally, there is another quartz feature that has been observed at 9.2 μm (Launer et al., 1952). The 9.2 μm feature observed by Launer et al. (1952) was not discussed in detail in that study, so it is possible that they observed a shoulder of one the quartz features, from 9.0-9.4 μm (Figure 2A). It is also possible that smaller particles might shift the minimum of the quartz feature at 8.86, to 9.09 μm (e.g., see models in Figure 6D and 6E in Moersch and Christensen, 1995). The quartz feature from 8.6-9.0 μm (Figure 2A) is clearly present in the majority of our spectra, but it appears to be overprinted by the addition of another spectral feature that extends this limb over into higher wavelengths, up to about 9.30 μm. The addition of this extension into higher wavelengths is probably due to the combined addition of a clay feature from 9.1-9.6 μm, and the microcline feature at 9.2 μm.

If the increased 9.16 μm band depth in airborne remote sensing spectra is only a result of other lithologic factors, such as clast/particle size, surface roughness, degree of clast/particle size sorting, and rock area fraction, then it remains compelling that the spectral signal occurs at the Reststrahlen band for clay minerals. All of our spectra show that minerals with similar and/or overlapping spectral features are present in the overall lithologic mixtures. All in all, both the remote sensing and ground-based spectra represent a similar mixture of minerals, with quartz, feldspars, and clay(s) present, but the problem remains between the 9.16/9.30 μm features, and this will require further investigation. Only the band depth at 9.16 μm in airborne spectra varies systematically with surface age, and the majority of all of the spectra can be explained by similar mineral mixtures, where the mixture does not vary with age. While the increasing band depth (or spectral contrast) with age in airborne remote sensing spectra cannot be explained by varying mineral mixtures alone, the difference between the 9.16/9.30 μm features in airborne/ground-based data sets remains a problem that needs to be addressed.

Definitions of Clast and Particle Size

For the purposes of this discussion and here after, we need to define how we are using terms that refer to the size of lithologic material in loose surficial regolith. The best resolution of our ability in the field to analyze sediment size is limited to ~ ≥1 mm. We use the term "clast(s)" to refer to macroscopic sediment sizes that are ≥1 mm, and "particle(s)" to refer to microscopic sediment sizes that are <1 mm. Following the Wentworth scale for sediment size (e.g., Boggs, 2012), terms for macroscopic clasts ≥1 mm are very coarse sand,

granule(s), pebble(s), cobble(s), and boulder(s), whereas terms for microscopic particles <1 mm are coarse/medium/fine/very fine sand, coarse/medium/fine/very fine silt, and clay. Note that since much of this manuscript involves a detection of clay mineralogy, the reader can assume that when we refer to "clay(s)", we are referencing mineralogy and not particle size. We will avoid using the term "clay(s)" to refer to particle size, but it will be clearly indicated if necessary. Although the majority of the sediment sizes that we were able to analyze were macroscopic clasts ≥1 mm, we acknowledge that our hypothesis is based on a spectral contribution from clay minerals, which are likely present in abundance in smaller size fractions. Thus, there will also be some discussion regarding how microscopic particles <1 mm might also contribute to the remote sensing signals and trends that we observe.

The Effect of Clast and Particle Size

Infrared laboratory spectra show that as microscopic particle size increases, often so does spectral contrast/band depth (Lyon, 1965; Hunt and Vincent, 1968; Conel, 1969; Figure 1 in Salisbury and Walter, 1989; Salisbury and Wald, 1992; Bishop et al., 1994; Cooper and Mustard, 1999; but for examples where this is not always the case, see Hunt and Vincent, 1968; Salisbury et al., 1987). Horgan et al. (2009) acquired similar results in short-wavelength infrared spectra (1.0-2.5 μm), but they also included in their analysis sediment sizes >1 mm to the same effect. The decrease in spectral contrast with decreasing particle size can be partially attributed to volume scattering, where the size of smaller particles causes them to become optically thin and have lower overall opacity (Salisbury and Wald, 1992).

If the effect of spectral contrast and band depth increasing as particle size increases continues to scale up to even larger macroscopic clast sizes, then it is possible that the observed trend in our data is due to variation in dominant clast size on the different geomorphic surfaces. Based on the general pattern of increasing band depth with age in our remote sensing spectra, it follows that this might be due to increasing dominant clast size with age on the Quaternary geomorphic surfaces. Figure 7 shows estimates for dominant (>50%) clast size range for each of the sampling sites on the upstream and downstream sets of surfaces. The correlation coefficient between dominant clast size (mean value of each range) and age is very small, $R^2 = 0.10$ (Figure 15 and Table 3). The dominant clast size varies over the different surfaces, but it fluctuates unpredictably.

Clay minerals could be more abundant in the smaller clast size fraction, below our ability to resolve. Our clast size analysis is limited to fragments that are ≥1 mm, yet we are concerned with looking for evidence that the remote sensing signal is influenced primarily by clay mineralogy. Even though our field data for dominant size of macroscopic individual surficial clasts do not show an increase in size with age, microscopic clay particles can increase in size in a few different ways. Individual clay crystals could grow and increase in size with age as part of their initial formation mechanism via weathering and alteration of existing minerals. Alternatively, individual clay crystals can agglomerate and increase in aggregate size, which is, however, likely for clays that accrete on surfaces to form desert varnish. In addition to increasing band strength with increasing particle size, Cooper and Mustard (1999) also observed that, in coarser samples, the larger clay particles were not individual crystals, but rather amalgamations of smaller particles. As surficial coatings of desert varnish grow, constituent clay particles amalgamating into larger single masses might

result in spectra that are consistent with larger single particles, which is the obvious source of the increasing band depth at 9.16 μm in the airborne spectra.

Most of the ground-based spectra that we collected were from single lithologic sample chips, where clay minerals might be underrepresented. Therefore, spectra of specific relevance to the consideration of clast size effects include "sand" spectra, from finer, unconsolidated lithologic detrital material (see Table 2). In many of the ground-based spectra for single clasts, there is an apparent signal, and remarkable band depth for a feature at 9.30 μm (Figures 13, 14, and Supplemental Items). However, in "sand" spectra, there is also always an apparent signal, but not always remarkable band depth at 9.30 μm (Figures 12, and S11, S13, and S18 in the Supplemental Items).

We wanted to assess whether the smaller clast size fraction had higher clay mineral content. To check this, we observed the spectral behavior at a field site located within an ephemerally active channel (C3sand, 13 ka, Figure S13 in the Supplemental Items). The dominant (>50%) clast size range for C3sand is <1 mm (Figure 7, labeled "(sand sample)"). Interestingly though, for C3sand the ground-based spectra do not have a pronounced band depth at the expected position for clays, from 9.1-9.6 μm (see Figure 1 in Michalski et al., 2006). This supports ruling out a higher relative abundance of any clay minerals in the smaller clast size fractions. Although a noticeable emissivity trough is present in ground-based spectra for C3sand at about 9.30 μm, the feature does not have a significant band depth, especially relative the main quartz doublet located from 8-9 μm. For reference, see a remarkable band depth at about 9.30 μm, relative to the quartz doublet from 8-9 μm, in ground-based spectra for the increasingly older upstream (Qt2, Qt1, Qt0) and downstream (C2, C1, C0) surfaces. Any clay minerals at the site C3sand may have been removed by

fluvial and/or aeolian processes. Or, it is possible that the effects of particle size reduction (reduction in spectral contrast) compete with increasing clay abundance (increasing band depth of features attributable to clay minerals). In any case, a significant band depth is also absent in airborne remote sensing spectra for the C3 surface, which could be why C3 is "in position" for all five sets of spectra (see Results: Airborne Remote Sensing Spectra).

Our data do not show strong correlation between macroscopic clast size and surface age (Figure 15 and Table 3), so we exclude this as a factor that is primarily causing the increasing-band-depth-with-age trend in our remote sensing spectra. However, even though the macroscopic dominant clast size does not generally increase with age, it is likely that the individual microscopic clay crystals are agglomerating with age to manifest as larger particles. These larger particles or coatings could cause the increased band depth for the older surfaces if the agglomeration process occurs via protracted and continuous desert varnish growth. By proxy, this means that the trend in our data could be at least partially dependent on time.

The Effect of Macroscopic Topographic Surface Roughness and Degree of Clast Size Sorting

We did not expect individual clasts to increase in size with age, since rocks at the Earth's surface undergo physical and chemical weathering processes that almost always result in size reduction. Instead, we could hypothesize that clast size would decrease over time, but this by itself would likely decrease spectral contrast and band depth, opposite to the

general trend in airborne remote sensing spectra. Therefore, we must instead consider how clast size and surface morphology are related in a way that could increase band depth.

Figures 8, 9, 15, and Table 3 show that desert varnish and desert pavement scores generally increase with surface age. For surface morphology in general, the term 'desert pavement' is used to describe the primary topographic characteristic of surfaces in warm, arid regions when they become relatively smooth and compacted, which occurs over thousands to tens of thousands of years. McFadden et al. (1987) propose an evolutionary path in which bombardment of larger clasts by eolian dust assists in physical weathering, while the dust also accumulates with other smaller clasts in topographic depressions to form soil that eventually underlies a surficial veneer of stone pavement. The overall effect is a smoothing of the surficial topography, which can increase spectral contrast and band depth. Relatively smooth pahoehoe-style lava flows have been shown to exhibit increased spectral contrast in relation to their rougher, aa-style counterparts of the same composition (Kahle et al., 1988). Similarly, an increase in spectral contrast was also observed for smooth obsidian glass relative to more uneven surfaces on vesiculated pumice (Ramsey and Fink, 1999).

Spectral variation due to surface roughness is known as the cavity effect. With this effect, spectral emissivity increases at all wavelengths, due to energy being reflected multiple times when it encounters internal surfaces of a hollow cavity (Kirkland et al., 2001). The cavity effect on lithology is in play at all scales of physical size, from macroscopic (≥1 mm) hollows due to the random orientations of surficial regolith, down to microscopic (<1 mm) roughness that might be present even on deceptively smooth-appearing lithic fragments (Kirkland et al., 2001). For our purposes, it is possible that for the older surfaces that have smoothed topography coincident with a significant desert pavement formation, the relative

smoothness could be contributing to the increasing 9.16 μm band depth (in airborne spectra) with age.

The evolution towards a smoother surface also involves, to some degree, the effect of clast size sorting. The sorting process likely involves some transport and/or removal of smaller, more labile particles, while larger particles are broken down into smaller fragments by weathering processes. This convergence in clast size for the ultimate surficial material will cause the dominant clast size range to decrease, resulting in a higher degree of sorting. Given the overall character of older, stable terrace surfaces where a moderately- to well-developed desert pavement surface has developed (usually along with substantial coatings of desert varnish on clast surfaces), we could hypothesize a relationship between age and degree of clast size sorting.

The dominant (>50%) clast size range graphs (Figure 7) might show a weak correlation between age and degree of sorting, in the sense that the ranges are generally smaller for sites on older surfaces. If only taking the largest range for each surface, the correlation becomes slightly more compelling. In a youngest/oldest age binary sense for both the upstream and downstream sets of surfaces, the smallest range for the oldest surface is exceeded by the largest range for the youngest surface. Furthermore, the youngest upstream and downstream surfaces (Qt4 and C3 respectively) exhibit both the largest and smallest dominant clast size ranges, which shows a lower overall degree of sorting for the entire surface. This age and sorting relationship is also somewhat qualitatively evident by viewing all of the field site images and noting the relatively chaotic surface morphology of the younger surfaces that results from mixtures of larger clasts, finer particles, and also a greater amount of vegetation (which will be discussed below). On the younger surfaces, our data

show that there can be a greater degree of sorting (smaller range) for individual 1-m^2 pixels (e.g., see C3sand in Figure 7), but the higher variability between sites on single surfaces exhibits greater overall variation (overall lesser degree of sorting).

The youngest upstream and downstream surfaces exhibit the largest difference among dominant (>50%) clast size ranges for multiple sample sites (Figure 7). This implies a lower degree of sorting for younger surfaces, which increases macroscopic roughness and the cavity effect, and ultimately reduces spectral contrast. Although this conclusion implies that the increasing 9.16 μm band depth with age is not necessarily (or entirely) dependent on clay minerals accumulating in desert varnish, the spectral effect is still related to age. It is plausible that a relationship between topographic smoothing and age exists (e.g., see Mushkin et al., 2014), and it is also likely that the relationship is concomitant with desert varnish and pavement development. The topographic smoothing with age can be one of the reasons that there is increased spectral contrast and 9.16 μm band depth with surface age in airborne remote sensing spectra. Topographic smoothing with age is also apparent for the surfaces that we are studying at the meter-scale level: bar and swale hummocky topography was only observed at sites on the younger upstream surfaces (see field photographs for sites Qt4p2 (<11 ka), Qt3p1 and Qt3p2 (13 ka), Figures S2-S4 in the Supplemental Items).

The Effect of Vegetation

It is outside of the scope of this study to consider the identifications, nuances, and associated thermal infrared spectroscopy of specific vegetation types that can be found in the study area. Also, much of the area is usually sparsely vegetated to begin with, given the

regional desert environment. Therefore, we speak with broad generality regarding vegetation species that are present and contributing to remote sensing spectra, and we usually only refer to vegetation in this arid region in the most general sense as "desert scrub." However, we do provide a limited assessment when such data were collected in the field for our purposes. The desert scrub mainly includes an abundance of common, non-deciduous chaparral plants, such as creosote and sage, and other species that are also likely present.

The period that we performed field work in the area (March 2017 through May 2017) followed a very wet winter season; precipitation was the heaviest seen in probably at least a decade in southern California. Thus, many of the field images contain lots of 10 to 50 cm tall plants, including flowers, shrubs, and grasses, in various states of desiccation: these were only present in the spring for a few weeks, following a brief cycle of sprouting, blossoming, and then dying off. This relatively small, flowering vegetation can dominate the scene during spring blooms that follow rainy winter seasons. But due to their ephemeral nature, this vegetation will not play a significant role in contributing to remote sensing spectra, unless the acquisition occurs during a spring bloom. Our airborne remote sensing imagery was collected during the height of summer heat and aridity extremes (the norm for Coachella Valley summers), at 10:45-11:00 am (Pacific daylight savings time), on 24 September 2015.

In the study area, vegetation is generally sparse or absent where desert pavement is well-developed, which coincides with older surfaces (Figures 8, 9, and 10). If present on older surfaces, vegetation is usually localized in/near channels, or flanking areas with pavement (e.g., see field photographs from sites on Qt2 (74 ka) and Qt1 (87 ka), Figures S5-S8 in the Supplemental Items). Vegetation is also absent in the youngest, most active channels on younger surfaces (e.g., see field photographs from C3sand, Figure S13 in the

Supplemental Items). Vegetation found on older surfaces are mostly 1-2 m scrub bushes, but vegetation on younger surfaces is much more abundant and diverse, also including 10-30 cm shrubs, 10-50 cm cacti, and some dead wood.

In our analyses, we included some ground-based spectra of the larger (1-2 m scale), woody, desert scrub bushes that are more drought tolerant and likely to persist year round. At the upstream site Qt4p1 (<11 ka, Figure 12), five ground-based spectra from vegetation were combined with five lithologic spectra into the "Average" mixture spectrum for the 1-m^2 sample area. For Qt4p1, ground-based vegetation spectra samples included: 1) two spectra from some very light green to whitish broad leaves (see sample square meter field photograph in Figure 12A: the small, 10-30 cm light green/white broad-leaved plant included in the upper right corner of the sampling area, possibly *Encelia farinosa*, or white brittlebush?); 2) two spectra of white, leafless (at time of collection), dry, woody, branches from the 30-50 cm white branchy plant (located in the lower right corner of the site overview field photograph in Figure 12B); and 3) one spectrum from a branch of dead wood (located just to the left of the sample square meter in Figure 12B). Also present on the Qt4 surface were 1-2 m green woody scrub, and 10-50 cm cacti. Ground-based spectra for the upstream site Qt2p2 (74 ka) included one vegetation measurement that is averaged with eight other lithologic spectra from within the sample square meter (see Table 2, and Figure S6 in the Supplemental Items). The ground-based vegetation spectrum at Qt2p2 is from a c. 10 cm desiccated ephemeral flowering plant. The downstream site C3veg (13 ka) consists of a single 1-2 m desert scrub bush (see Table 2 and Figure S14 in the Supplemental Items). The bush was light green to yellow, partially desiccated, with woody branches, 1-2 cm thorns, and very narrow (almost needle-like) leaves; this type of plant was commonly encountered,

and it is possibly *Psorothamnus arborescens* (Mojave indigo bush), or *Psorothamnus schottii* (Schott's dalea, personal communication with botanist Jean Pawek).

The ground-based averaged spectra are simplified models that show qualitative effects for how mixtures might manifest in airborne remote sensing spectra that include multiple heterogeneous materials within the 1-m^2 pixel size. We acknowledge that the simplified models presented here are at odds with actual remote sensing spectra (which intrinsically capture greater heterogeneity over a larger sample area), because the latter likely include effects from non-linear mixing of vegetation with a lithologic background (Ray and Murray, 1996). However, these results still give us a broad sense of how the inclusion of vegetation might affect any lithologic signal that is present.

There is a common misconception that vegetation spectra in the thermal infrared wavelength regime (8-14 μm) tend to be flat and featureless (Elvidge, 1988; Ullah et al., 2012). Kahle et al. (1987) did find that desert vegetation had completely flat spectra, but this and other similar observations could be due to the fact that fresh green plant material can contain a significant amount of water weight (40-80%, Elvidge, 1988), and water is flat and featureless in the thermal infrared. We did not make any assumptions about what spectra from vegetation in our study area would look like, but our ground-based measurements for sites Qt4p1 (Figure 12), Qt2p2 and C3veg (Figures S6 and S14 in the Supplemental Items), all show that vegetation spectra are relatively flat and featureless in comparison with the lithologic spectra. Despite the fact that the spectra were collected from distinctly different plants, the five vegetation spectra taken from site Qt4p1 and the single vegetation spectrum taken from site Qt2p2, all are very similar and have very broad emissivity peaks from 8-10 μm wavelengths, which is the specific range where we are looking for distinct emissivity

troughs/minima, and variation in Reststrahlen feature positions (from varying silica-based mineralogy). In our ground-based average spectra that include vegetation, the broad vegetation emissivity peaks from 8-10 μm flatten lithologic Reststrahlen features in the same range, effectively reducing spectral contrast. The similarly flat spectra from C3veg would also produce similar results if incorporated into our models.

The relatively flat ground-based spectra from C3veg (13 ka, Figure S14 in the Supplemental Items), with its needle-like leaves, can be attributed to the cavity effect. In thermal infrared spectroscopy of vegetation, small and/or needle(-like) leaves increase the cavity effect, which, as discussed previously, reduces spectral contrast, especially relative to species with larger and flatter leaves (Ribeiro da Luz and Crowley, 2010; Ullah et al., 2012). Due to higher variability in individual leaf orientations, needle-shaped or needle-like leaves are thought to increase the cavity effect and minimize spectral contrast (Salisbury, 1986; Ribeiro da Luz and Crowley, 2007). Furthermore, there could also be a reduction in spectral contrast due to the cavity effect from microscopic surface roughness on plant surfaces (Ribeiro da Luz and Crowley, 2007).

In considering the effect of vegetation, there also exists the complication that some plant material can be silicified (Ribeiro da Luz and Crowley, 2007; 2010), which could produce the same Reststrahlen features that we are interested in (but from silica-based lithology). Silica present in plants could complicate our spectral analysis, because several specific species (although unlikely to be present in our study area) are known to become silicified and exhibit spectral features in the same 9-10 μm range (Ribeiro da Luz and Crowley, 2010), where we are looking for clay mineral Reststrahlen features.

Because the ground-based vegetation spectra are relatively flat and featureless, we conclude that the effect of vegetation is to reduce the spectral contrast in airborne remote sensing imagery pixels. In the study area, vegetation is more abundant, prominent, and diverse on younger surfaces. Estimates for average spacing of 1-2 m desert scrub bushes generally increase with surface age (Figures 10, 15, and Table 3), so if a silica is present in vegetation and contributing to spectra, we expect a greater contribution to the 9-10 μm feature in younger surfaces. However, we observe that the 9-10 μm spectral feature becomes more prominent in older surfaces with less vegetation. Thus, increased vegetation on younger surfaces is likely responsible for reducing their spectral contrast. It is also plausible that the correlation between increasing band depth at 9.16 μm and surface age can be a manifestation of increased spectral contrast on older surfaces that are more sparsely vegetated. Although this does not directly relate to our hypothesis that clay minerals in desert varnish are mainly responsible for the increase spectral contrast on older surfaces, it still strengthens the positive correlation between increasing spectral contrast and surface age. Therefore, independent of the cause, it is nonetheless still valid that spectral contrast correlates positively with age for geomorphic surfaces in this study area.

The Effect of Rock Area Fraction

Solid and particulate forms of materials exhibit transmission spectra that can vary considerably (Keller and Pickett, 1949), and similarly, when considering the effect of particle size on spectral contrast, the bulk density of the particulate matter must also be taken into account. For example, quartz exhibits greater spectral contrast in Reststrahlen bands not only

when particle size is increased, but also when the particulate is packed as opposed to being left in its loose, unconsolidated form (Salisbury and Eastes, 1985; Salisbury and Wald, 1992). Decrease in either particle size, or in the density of a particulate mass, will result in increased porosity, which can increase the cavity effect (Salisbury and Eastes, 1985) and volume scattering (Salisbury and Wald, 1992), both of which reduce spectral contrast. Therefore, we must also consider the coupled effects that particle size and packing (or density of material) have on our data.

To consider the packing/density effect, we looked at the rock area fraction (minimum, %) at each of our 1-m^2 field sampling sites (Figure 11) (i.e., "solid rock" being larger lithic fragments that represent the material with highest density/lowest porosity, versus smaller, loose sediment grains). On the basis of the arguments stated above and empirical data from previous work, we could hypothesize that the general positive correlation between increasing spectral contrast with surface age in airborne remote sensing spectra might be due to the solid rock (i.e., highest density/lowest porosity) area fraction increasing with surface age. However, we observe no general monotonically increasing trend, or mathematical correlation (Figure 15 and Table 3) for rock area fraction with surface age. Conversely, for the upstream surfaces (upper panel in Figure 11), the highest rock area fraction occurred at a site on the youngest surface (Qt4p2, <11 ka), and the lowest rock area fraction occurred at a site on the oldest surface (Qt0p2, >95 ka). Similarly, for the downstream surfaces, the two sites on the youngest surface (C3, 13 ka) both have rock area fractions that are greater than any of those from the three sites on the oldest surface (C0, >95 ka).

The increased rock area fraction on younger surfaces might be due concentration of larger cobbles and boulders (which quickly add up to a larger fraction), that have not yet been

weathered into smaller clasts. The inherent increase in surface roughness, and subsequent cavity effect, from a greater number of larger clasts, could outweigh the increase in rock area fraction, and ultimately reduce spectral contrast for younger surfaces. In a different way, the older surfaces that have well-developed desert pavement can also have a greater degree of compaction, which also results in higher density/lower porosity. Because increasing spectral contrast can be the effect of increasing density (not necessarily to the point of complete lithification to a solid), it is possible that the increased spectral contrast on older surfaces might be due to the greater degree of compaction found on older surfaces with well-developed desert pavement. Our rock area fraction analysis does not test for this variability, so it is still possible that the greater spectral contrast on older surfaces is caused by decreasing porosity (cavity effect), but not because of a greater rock area fraction.

Other Effects

When analyzed in detail, airborne remote sensing spectra from the downstream C2f (26 ka) surface, were problematic. The C2f surface is located on a steep ridge, directly on the surface trace of the Mission Creek strand (Figures 3 and 4). Not only did we observe the greatest standard deviation in airborne spectra band depth at 9.16 μm (see data point for 26 ka surface age in Figure 6), we also observed great variation when we sampled spectra from the C2f surface by different slope values. With its relatively drastic changes in slope, the C2f surface is dissimilar to any of the other surfaces, with their relatively broad, flat, and stable topography, which is conducive to protracted varnish and pavement development. Recall that in the downstream airborne remote sensing spectra, the oldest C0 (>95 ka) surface is in

position with the greatest band depth at 9.16 μm for three of the five subsets, and for the remaining two sets, C2f (26 ka) has the greatest band depth. This anomaly could be attributed to the spectral variation in C2f caused by increased and variable topographic slope. Thus, we note that the methods used in this research should not be applied to surfaces that lack a relatively broad, flat, and stable topography.

Above, in the Results section (see Ground Truth Field Work: Additional Field Observations), we also noted a distinct, light pink oxidation on clasts at the downstream site C2fp1 (26 ka) site, and a conspicuous higher relative abundance of red-orange oxidation at the upstream site Qt1p2 (87 ka). Oxidization is likely to occur on the buried bottoms of varnished clasts, due to iron oxide formation at soil or sub-soil level (Figures 2 and 3 in Engel and Sharp, 1958; Potter and Rossman, 1977; 1979a). Therefore, it is possible that the greater degree of oxidation observed at these sites represents many of the clasts being flipped over, especially on the steep and topographically unstable downstream C2f (26 ka) surface (see above). Oxides related to desert varnish development likely reduce spectral contrast due to their lack of spectral features in the wavelengths that our data covered (λ = 7.6-13.2 μm, see Figures 3 and 6 in Potter and Rossman, 1979a; Figure 14 in Potter and Rossman, 1979b). This effect could have caused the great spectral variation for the Qt1 and C2f surfaces. In airborne remote sensing spectra, the unexplained variation in the C2f (26 ka) surface was discussed above, and Qt1 (87 ka) was never in position, twice with very shallow band depth at 9.16 μm relative to the other older surfaces. Thus, we note that surfaces with a great degree of iron oxides also might not be suitable for the methods used in this research.

Bishop et al. (1994) observed another factor that could affect spectral contrast for montmorillonite clay: laboratory spectra from montmorillonite clay increased in band depth

with increasing grain size when lab samples were left unpacked, but when packed, the largest size fraction did not display the greatest band depth for a spectral feature at 1.9 μm. Although that wavelength position is outside of the range covered in this research (λ = 7.6-13.2 μm), they mentioned that their packing process resulted in lab samples with a variable degree of alignment and orientation among the particles. Thus, we note that when comparing any spectra to library standards, care should be taken to identify and consider the particle size and degree of packing used for measurements. Namely, when using linear mixture models, particle size should be much larger than the wavelengths in measured spectra (a condition that was met for our models in Figure 2, see caption).

CONCLUSIONS

In airborne remote sensing spectra of geomorphic surfaces along the southern San Andreas fault, we observed positive correlation (R^2 = 0.59) between increasing spectral contrast and band depth at 9.16 μm with surface age (Figures 5, 6, 15, and Table 3). We hypothesized that the increase in band depth at 9.16 μm was related to an increasing relative abundance of clay minerals (clay crystal aggregates) in progressively thicker coatings of desert varnish on older surfaces. To test our hypothesis, we conducted fieldwork to evaluate variation among surfaces in: clast size range, desert varnish and pavement development, vegetation spacing (proxy for abundance or sparsity), and rock area fraction. Of the quantities that we measured, there are no systematic trends related to increasing age for either mean of dominant (>50% relative abundance) clast size range (R^2 = 0.10) or rock area fraction (R^2 = 0.00). The quantities that had a stronger positive correlation with increasing surface age

(Figure 15 and Table 3) were: desert varnish scores (Spearman's rank = 0.90), desert pavement scores (Spearman's rank = 0.90), and vegetation spacing (R^2 = 0.34).

Ground-based field spectra from single lithologic clasts displayed a spectral feature at 9.30 μm that did not generally increase with surface age. While this 9.30 μm ground-based feature is still within the 9.1-9.6 μm range that typifies clay minerals, further analyses will be required to investigate why the main ground-based feature is not at the exact same position as the airborne remote sensing spectral feature at 9.16 μm. Furthermore, ground-based spectra from finer-grained, unconsolidated detrital material did not display increased band depth for the 9.30 μm feature, indicating that clay minerals are not necessarily more prevalent in the smaller clast/particle size fraction. While most of our spectra indicate the presence of some clay mineral(s), the spectra are overprinted with spectral features from common tectosilicate minerals (quartz and feldspars) characteristic of the varnish substrate. Also, ground-based vegetation spectra are very flat and featureless in the thermal wavelengths that correspond to those covered in the airborne remote sensing spectra. Therefore, we conclude that the increasing development of desert varnish and desert pavement, combined with decreasing vegetation, increase spectral contrast in airborne remote sensing spectra. The development of varnish and pavement usually takes a significant amount of time, and often generally decreases vegetation abundance, so an increase in spectral contrast based on these variables is generally related to the passage of time.

While this research does not outline a methodology to derive absolute ages for Quaternary geomorphic surfaces, the ideas presented here might make it possible in the future to determine relative ages, based on relative spectral contrast of geomorphic surfaces. Stricter age constraints could perhaps follow, if an age is known for at least one set of

geomorphic surfaces in a terraced (or otherwise related) series, as a calibration for a larger area or region. The methodology can be expanded to include varying spectral contrast/band depth in spectral features from other minerals (e.g., quartz features at 12.4-13.0 μm), and applied to other known geomorphic surface ages (e.g., see Gray et al., 2014). With the spatial component of tectonic displacement from an overhead perspective (i.e., offset feature identified, then separation distance measured), information derived regarding the time component from relative ages of geomorphic surfaces could potentially be used to estimate a fault slip rate from a single airborne remote sensing image.

ACKNOWLEDGEMENTS

This material is based upon work supported by the National Science Foundation (NSF) Graduate Research Fellowship Program under Grant No. 1144469 awarded to R. Witkosky. Mako airborne hyperspectral imagery was acquired under the auspices of the Aerospace Corporation's Independent Research and Development program. We thank Ginny Short for allowing access to the Thousand Palms Oasis Preserve, Maggie Anderson for processing the ground-based spectral data, and Ryan Gold for creating the DEM of our study area. Reference to any specific commercial products, process, or service by trade name, trademark, manufacturer, or otherwise, does not necessarily constitute or imply its endorsement, recommendation, or favoring by the United States Government. The views and opinions of authors expressed herein do not necessarily state or reflect those of the United States Government, and shall not be used for advertising or product endorsement purposes.

APPENDIX

Literature Review on Seismic Activity along the Southern San Andreas Fault

Paleoseismic Trenching

Paleoseismic trenching along the southern San Andreas fault at sites in the Coachella Valley has yielded recurrence intervals of c. 200 years (Fumal et al., 2002; Philibosian et al., 2011), while a recurrence interval calculated at the Wrightwood site (>100 km to the northwest) is roughly half of that value (Scharer et al., 2007). While it might appear that large, surface-rupturing earthquakes in the Coachella Valley occur less often than on other segments, the paleoseismic data consistently drive the message that the southern San Andreas might be due for a major seismic event soon, since it has been more than 300 years since the most recent large earthquake in the region (Sieh et al., 1989; Sieh and Williams, 1990; Fumal et al., 2002; Philibosian et al., 2011).

Tectonic Geomorphology

Methods in tectonic geomorphology have been used extensively to estimate geologic slip rates for the Coachella Valley segment of the southern San Andreas fault. However, these geologic slip rates can vary widely due to the complexity of the fault zone at some localities. A well-known offset alluvial fan used for fault slip rate analyses is located in the Indio Hills, near Biskra Palms (unfortunately, anthropogenic excavation has now almost

completely obliterated this natural asset). The Biskra Palms site yielded a geologic slip rate of 15.9 ± 3.4 mm/yr (van der Woerd et al., 2006) for the Mission Creek strand of the San Andreas fault. This rate was later updated to about the same central value in a range but with larger uncertainty (12-22 mm/yr), on the basis of greater net slip and more robust age constraints that broadly agreed across multiple independent dating methods (Behr et al., 2010; Fletcher et al., 2010; Benedetti and van der Woerd, 2014). Southeast of Biskra Palms at the Mecca Hills, Shifflett et al. (2002) calculated a significantly slower slip rate of 5-8 mm/yr. To the immediate northwest of Biskra Palms, the overall San Andreas fault structure becomes complex as the parallel Banning strand (located southwest of the Mission Creek strand) comes into play. The slip rate for the Mission Creek strand increases to 22-25 mm/yr at Pushawalla Canyon (Blisniuk and Sharp, 2014), then remarkably decreases to 4 ± 2 mm/yr at Thousand Palms Oasis (Fumal et al., 2002); all of this variation occurs within a distance of <10 km from the Biskra Palms site (Figure 1). Farther to the northwest, the Banning strand has a Holocene slip rate of 4-5 mm/yr (Gold et al., 2015), and the fault structure becomes more complex with the parallel Garnet Hill strand somewhat enigmatically coming into play to the southwest of the Banning strand (e.g., Cardona et al., 2015; Cardona, 2016). At the northwest terminus of the Coachella Valley, the San Andreas fault zone's structure becomes very complex, as multiple strands with opposing left lateral (Kendrick et al., 2015) and oblique right lateral with reverse/thrust (Huerta, 2015; 2017) relative fault motion interact through the San Gorgonio Pass (Yule, 2009).

Tectonic Geodesy

While geologic fault slip rates are averaged over centuries to millennia (or even greater time periods), geodetic fault slip rates are averaged over years to decades. Also, geologic fault slip rates are usually strict minima when based on reconstructing piercing points, such as an offset lithologic contact or stream channel. These fundamental data type differences could perhaps explain why geodetic slip rates for the southern San Andreas fault are generally faster than the geologic rates. A current geodetic slip rate for the southern San Andreas fault from combined InSAR and GPS was 25 ± 3 mm/yr (Fialko, 2006). With that rate significantly higher than those found from the geology, a revised fault geometry in the structural model used slowed the geodetic rate to 18 ± 1 mm/yr (Lindsey and Fialko, 2013), putting it closer to the geologic rates mentioned above (usually <20 mm/yr). Slip rates for the southern San Andreas fault from GPS data agree to some extent with geologic rates because they generally decrease to the northwest from a maximum of c. 23 mm/yr in the southeast (Spinler et al., 2010). Note that this observation only holds if the aforementioned result of Shifflett et al. (2002) is ignored.

REFERENCES CITED

Aulinas, M., Garcia-Valles, M., Fernandez-Turiel, J.L., Gimeno, D., Saavedra, J., and Gisbert, G., 2015, Insights into the formation of rock varnish in prevailing dusty regions: Earth Surface Process and Landforms, v. 40, p. 447-458, doi: 10.1002/esp.3644.

Bartholomew, M.J., Kahle, A.B., and Hoover, G., 1989, Infrared spectroscopy (2.3-20 μm) for the geological interpretation of remotely-sensed multispectral thermal infrared data: International Journal of Remote Sensing, v. 10, n. 3, p. 529-544.

Beck, W., Donahue, D.J., Jull, A.J.T., Burr, G., Broecker, W.S., Bonani, G., Hajdas, I., and Malotki, E., 1998, Ambiguities in direct dating of rock surfaces using radiocarbon measurements: Science, v. 280, 2132-2139, doi: 10.1126/science.280.5372.2132.

Behr, W.M., Rood, D.H., Fletcher, K.E., Guzman, N., Finkel, R., Hanks, T.C., Hudnut, K.W., Kendrick, K.J., Platt, J.P., Sharp, W.D., Weldon, R.J., and Yule, J.D., 2010, Uncertainties in slip-rate estimates for the Mission Creek strand of the southern San Andreas fault at Biskra Palms Oasis, southern California: Geological Society of America Bulletin, v. 122, n. 9/10, p. 1360-1377, doi: 10.1130/B30020.1.

Benedetti, L.C., and van der Woerd, J., 2014, Cosmogenic nuclide dating of earthquakes, faults, and toppled blocks: Elements, v. 10, n. 5, p. 357-361, doi: 10.2113/gselements.10.5.357.

Bishop, J.L, Pieters, C.M., and Edwards, J.O., 1994, Infrared spectroscopic analyses on the nature of water in montmorillonite: Clays and Clay Minerals, v. 42, n. 6, p. 702-716.

Bishop, J., Madejová, J., Komadel, P., and Fröschl, H., 2002a, The influence of structural Fe, Al, and Mg on the infrared OH bands in spectra of dioctahedral smectites: Clay Minerals, v. 37, p. 607-616.

Bishop, J., Murad, E., and Dyar, M.D., 2002b, The influence of octahedral and tetrahedral cation substitution on the structure of smectites and serpentines as observed through infrared spectroscopy: Clay Minerals, v. 37, p. 617-628.

Bishop, J.L., Lane, M.D., Dyar, M.D., and Brown, A.J., 2008, Reflectance and emission spectroscopy study of four groups of phyllosilicates: smectites, kaolinite-serpentines, chlorites and micas: Clay Minerals, v. 43, p. 35-54, doi: 10.1180/claymin.20080.43.1.03.

Blisniuk, K., and Sharp, W.D., 2014, Estimating geologic slip rates on the southern San Andreas Fault, California: U-series and ^{10}Be dating: U.S. Geological Survey Final Technical Report for USGS Award No. G13AP00031, 9 p.

Boggs, S., Jr., 2012, Principles of sedimentology and stratigraphy, fifth edition: New Jersey, Pearson Education Inc., 585 p.

Buckland, K.N., Young, S.J., Keim, E.R., Johnson, B.R., Johnson, P.D., and Tratt, D.M, 2017, Tracking and quantification of gaseous chemical plumes from anthropogenic emission sources within the Los Angeles Basin: Remote Sensing of Environment, v. 201, p. 275- 296, doi: 10.1016/j.rse.2017.09.012.

Bull, W.B., 1991, Geomorphic responses to climate change: New York, Oxford University Press, 326 p.

Bürgmann, R., 1991, Transpression along the southern San Andreas fault, Durmid Hill, California: Tectonics, v. 10, n. 6, p. 1152-1163.

Cardona, J.E., Yule, D., Scharer, K., and Huerta, B., Constraining the most recent surface rupture on the Garnet Hill fault, Coachella Valley, CA, *in* Proceedings, Southern California Earthquake Center Annual Meeting, Palm Springs: California, Volume XXV, p 138-139.

Cardona, J.E., 2016, Constraining the most recent surface rupture on the Garnet Hill strand, San Andreas fault, Coachella Valley, California [M.S. thesis]: Northridge, California State University, 67 p.

Christensen, P.R., and Harrison, S.T., 1993, Thermal infrared emission spectroscopy of natural surfaces: application to desert varnish coatings on rocks: Journal of Geophysical Research, v. 98, n. B11, p. 19819-19834.

Christensen, P.R., Bandfield, J.L., Hamilton, V.E., Howard, D.A., Lane, M.D., Piatek, J.L., Ruff, S.W., and Stefanov, W.L., 2000, A thermal emission spectral library of rock-forming minerals: Journal of Geophysical Research, v. 105, n. E4, p. 9735-9739.

Clark, R.N., and Roush, T.L., 1984, Reflectance spectroscopy: Quantitative analysis techniques for remote sensing applications: Journal of Geophysical Research, v. 89, n. B7, p. 6329-6340.

Compton, R.R., 1985, Geology in the Field: New York, John Wiley and Sons, Inc., 398 p.

Conel, J.E., 1969, Infrared emissivities of silicates: experimental results and a cloudy atmosphere model of spectral emission from condensed particulate mediums: Journal of Geophysical Research, v. 74, n. 6, p. 1614-1634.

Cooper, C.D., and Mustard, J.F., 1999, Effects of very fine particle size on reflectance spectra of smectite and palagonitic soil: Icarus, v. 142, p. 557-570, doi: 10.1006/icar.1999.6221.

Cyr, A.J., Miller, D.M., Menges, C., Schmidt, K.M., Mahan, S.A., Maher, K., and Liu, T., 2016, Paleoclimatic controls on Pleistocene alluvial fan deposition in the Mojave and Colorado deserts and southern Great Basin, southwestern USA: Geological Society of America Abstracts with Programs, v. 48, n. 7, doi: 10.1130/abs/2016AM-285938.

Davis, C., and O'Rourke, T., 2011, 2011, Shakeout Scenario: water system impacts from a M_w 7.8 San Andreas earthquake: Earthquake Spectra, v. 27, n. 2, p. 459-476.

Deer, W.A., Howie, R.A., and Zussman, J., 1992, An introduction to the rock-forming minerals, second edition: England, Pearson Education Limited, 696 p.

Dibblee, T.W., Jr., 2008, Geologic map of the Thousand Palms and Lost Horse Mountain 15 minute quadrangles, Riverside County, California (edited by John A. Minch): Santa Barbara Museum of Natural History, Dibblee Geology Center Map #DF-372, scale 1:62500, 1 sheet.

Ehlmann, B.L., et al., 2009, Identification of hydrated silicate minerals on Mars using MRO-CRISM: Geologic context near Nili Fossae and implications for aqueous alteration: Journal of Geophysical Research, v. 114, n. E00D08, doi:10.1029/2009JE003339.

Elvidge, C.D., 1988, Thermal infrared reflectance of dry plant materials: 2.5-20.0 μm: Remote Sensing of Environment, v. 26, p. 265-285.

Engel, C.G., and Sharp, R.P, 1958, Chemical data in desert varnish: Bulletin of the Geological Society of America, v. 69, p. 487-518.

Farmer, V.C., 1974, Chapter 15, The layer silicates, *in* Farmer, V.C., ed., The infra-red spectra of minerals: London, Mineralogical Society Monograph 4, p. 331-363.

Farr, T.G., and Chadwick, O.A., 1996, Geomorphic processes and remote sensing signatures of alluvial fans in the Kun Lun Mountains, China: Journal of Geophysical Research, v. 101, n. E10, p. 23091-23100.

Fialko, Y., 2006, Interseismic strain accumulation and the earthquake potential on the southern San Andreas fault system: Nature, v. 44, p. 968-971, doi:10.1038/nature04797.

Fletcher, K.E.K., Sharp, W.D., Kendrick, K.J., Behr, W.M., Hudnut, K.W., and Hanks, T.C., 2010, ^{230}Th/U dating of a late Pleistocene alluvial fan along the southern San Andreas fault: Geological Society of America Bulletin, v. 122, n. 9/10, p. 1347-1359, doi: 10.1130/B30018.1.

Frankel, K.L., and Dolan, J.F., 2007, Characterizing arid region alluvial fan surface roughness with airborne laser swath mapping digital topographic data: Journal of Geophysical Research, v. 112, n. F02025, doi:10.1029/2006JF000644.

Frankel, K.L., et al., 2007, Cosmogenic 10Be and 36Cl geochronology of offset alluvial fans along the northern Death Valley fault zone: Implications for transient strain in the eastern California shear zone: Journal of Geophysical Research, v. 112, n. B06407, doi: 10.1029/2006JB004350.

Friedrich, A.M., Wernicke, B.P., Niemi, N.A., Bennett, R.A., and Davis, J.L., 2003, Comparison of geodetic and geologic data from the Wasatch region, Utah, and implications for the spectral character of Earth deformation at periods of 10 to 10 million years: Journal of Geophysical Research, v. 118, n. B4, 2199, doi:10.1029/2001JB000682.

Frost, R.L., Kloprogge, J.T., and Ding, Z., 2002, Near-infrared spectroscopic study of nontronites and ferruginous smectite: Spectrochimica Acta Part A: Molecular and Biomolecular Spectroscopy, v. 58, n. 8, p. 1657-1668, doi: 10.1016/S1386- 1425(01)00637-0.

Fumal, T.E., Rymer, M.J., and Seitz, G.G., 2002, Timing of large earthquakes since A.D. 800 on the Mission Creek strand of the San Andreas fault zone at Thousand Palms Oasis, near Palm Springs, California: Bulletin of the Seismological Society of America, v. 92, n. 7, p. 2841-2860.

Garvie, L.A.J., Burt, D.M., and Buseck, P.R., 2008, Nanometer-scale complexity, growth, and diagenesis in desert varnish: Geology, v. 36, n. 3, p. 215-218, doi: 10.1130/G24409A.1.

Gillespie, A.R., Kahle, A.B., and Palluconi, F.D., 1984, Mapping alluvial fans in Death Valley, California, using multichannel thermal infrared images: Geophysical Research Letters, v. 11, n. 11, p. 1153-1156.

Gillespie, A.R, Kahle, A.B., and Walker, R.E., 1987, Color enhancement of highly correlated images. II. Channel ratio and “chromaticity” transformation techniques: Remote Sensing of Environment, v. 22, p. 343-365.

Gold, P.O., Behr, W.M., Rood, D., Sharp, W.D., Rockwell, T.K., Kendrick, K., and Salin, A., 2015, Holocene geologic slip rate for the Banning strand of the southern San Andreas

fault, southern California: Journal of Geophysical Research: Solid Earth, v. 120, doi: 10.1002/2015JB012004.

Green, A.A., Berman, M., Switzer, P., and Craig, M.D., 1988, A transformation for ordering multispectral data in terms of image quality with implications for noise removal: IEEE Transactions on Geoscience and Remote Sensing, v. 26, no. 1, p. 65-74.

Hall, J.L., Boucher, R.H., Gutierrez, D.J., Hansel, S.J., Kasper, B.P., Keim, E.R., Moreno, N.M., Polak, M.L., Sivjee, M.G., Tratt, D.M., and Warren, D.W., 2011, First flights of a new airborne thermal infrared imaging spectrometer with high area coverage, *in* Andresen, B.F., Fulop, G.F., and Norton, P.R., eds., Infrared Technology and Applications XXXVII, Proceedings of SPIE, v. 8012, p. 8012031- 8012037.

Helms, J.G., McGill, S.F., and Rockwell, T.K., 2003, Calibrated, late Quaternary age indices using clast rubification and soil development on alluvial surfaces in Pilot Knob Valley, Mojave Desert, southeastern California: Quaternary Research, v. 60, p. 377-393, doi:10.1016/j.yqres.2003.08.002.

Hook, S.J., Dmochowski, J.E., Howard, K.A., Rowan, L.C., Karlstrom, K.E., and Stock, J.M., 2005, Mapping variations in weight percent silica measured from multispectral thermal infrared imagery—Examples from the Hiller Mountains, Nevada, USA, and Tres Virgenes-La Reforma, Baja California Sur, Mexico: Remote Sensing of Environment v. 95, p. 273-289.

Horgan, B.H., Bell, J.F. III, Noe Dobrea, E.Z., Cloutis, E.A., Bailey, D.T., Craig, M.A., Roach, L.H., and Mustard, J.F., 2009, Distribution of hydrated minerals in the north polar region of Mars: Journal of Geophysical Research, v. 114, n. E01005, doi: 10.1029/2008JE003187.

Huerta, B., Yule, D., and Heermance, R., 2015, Structure and geomorphology of Whitewater Hill and slip transfer from the Banning and Garnet Hill strands of the San Andreas fault, *in* Proceedings, Southern California Earthquake Center Annual Meeting, Palm Springs: California, Volume XXV, p 156.

Huerta, B.E., 2017, Structure and geomorphology of west Whitewater Hill, a compressive stepover between the Banning and Garnet Hill strands of the San Andreas fault, Whitewater, CA [M.S. thesis]: Northridge, California State University, 64 p.

Hunt, J.M., Wisherd, M.P., Bonham, L.C., 1950, Infrared absorption spectra of minerals and other inorganic compounds: Analytical Chemistry, v. 22, n. 12, p. 1478-1497, doi: 10.1021/ac60048a006.

Hunt, C.B., 1954, Desert varnish: Science, v. 120, n. 3109, p. 183-184.

Hunt, C.B., and Mabey, D.R., 1966, Stratigraphy and structure, Death Valley, California: United States Geological Survey Professional Paper 494-A, 162 p.

Hunt, G.R., and Vincent, R.K., 1968, The behavior of spectral features in the infrared emission from particulate surfaces of various grain sizes: Journal of Geophysical Research, v. 73, n. 18, p. 6039-6046.

Jayko, A.S., Menges, C.M., and Thompson, R.A., 2005, Digital method for regional mapping of surficial basin deposits in arid regions, example from central Death Valley, Inyo County, California: United States Geological Survey Open-File Report 2005-1445, 31 p.

Jones, L.M., et al., 2008, The ShakeOut Scenario: United States Geological Survey Open-File Report 2008-1150, 308 p.

Kahle, A.B., 1987, Surface emittance, temperature, and thermal inertia derived from Thermal Infrared Multispectral Scanner (TIMS) data for Death Valley, California: Geophysics, v. 52, n. 7, p. 858-874.

Kahle, A.B., Madura, D.P., and Soha, J.M., 1980, Middle infrared multispectral aircraft scanner data: analysis for geological applications: Applied Optics, v. 19, n. 14, p. 2279-2290.

Kahle, A.B., and Goetz, A.F.H., 1983, Mineralogic information from a new airborne thermal infrared multispectral scanner: Science, v. 222, n. 4619, p. 24-27.

Kahle, A.B., Gillespie, A.R., Abbott, E.A., Abrams, M.J., Walker, R.E., and Hoover, G., 1988, Relative dating of Hawaiian lava flows using multispectral thermal infrared images: A new tool for geologic mapping of young volcanic terranes: Journal of Geophysical Research, v. 93, n. B12, p. 15239-15251.

Kealy, P.S., and Hook, S.J., 1993, Separating temperature and emissivity in thermal infrared multispectral scanner data: implications for recovery of land surface temperatures: IEEE Transactions on Geoscience and Remote Sensing, v. 31, n. 6, p. 1155-1164.

Keller, W.D., and Pickett, E.E., 1949, Absorption of infrared radiation by powdered silica minerals: American Mineralogist, v. 34, n. 11-1, p. 855-868.

Keller, W.D., and Pickett, E.E., 1950, The absorption of infrared radiation by clay minerals: American Journal of Science, v. 248, n. 4, p. 264-273.

Keller, E.A., Bonkowski, M.S., Korsch, R.J., and Shlemon, R.J., 1982, Tectonic geomorphology of the San Andreas fault zone in the southern Indio Hills, Coachella Valley, California: Geological Society of America Bulletin, v. 93, p. 46-56.

Kendrick, K.J., Matti, J.C., and Mahan, S.A., 2015, Late Quaternary slip history of the Mill Creek strand of the San Andreas fault in San Gorgonio Pass, southern California: The role of a subsidiary left-lateral fault in strand switching: Geological Society of America Bulletin, v. 127, n. 5/6, p. 825-849, doi:10.1130/B31101.1.

Kirkland, L., Herr, K., Keim, E., Adams, P., Salisbury, J., Hackwell, J., and Treiman, A., 2001, First use of an airborne infrared hyperspectral scanner for compositional mapping: Remote Sensing of Environment, v. 80, p. 447-459.

Krinsley, D.H., Dorn, R.I., DiGregorio, B.E., Langworthy, K.A., and Ditto, J, 2012, Rock varnish in New York: An accelerated snapshot of accretionary processes: Geomorphology, v. 138, p. 339-351, doi:10.1016/j.geomorph.2011.09.022.

Lancaster, J.T., Hayhurst, C.A., and Bedrossian, T.L., 2012, Preliminary geologic map of Quaternary surficial deposits in southern California, Palm Springs 30’ X 60’ quadrangle: Geologic compilation of Quaternary surficial deposits in southern California, California Geological Survey Special Report 217, Plate 24, scale 1:100,000.

Launer, P.J., 1952, Regularities in the infrared absorption spectra of the silicate minerals: American Mineralogist, v. 37, n. 9-10, p. 764-784.

Lee, J.B., Woodyatt, S., and Berman, M., 1990, Enhancement of high spectral resolution remote- sensing data by a noise-adjusted principal components transform: IEEE Transactions on Geoscience and Remote Sensing, v. 28, n. 3, p. 295-304.

Lindsey, E.O., and Fialko, Y., 2013, Geodetic slip rates in the southern San Andreas Fault system: effects of elastic heterogeneity and fault geometry: Journal of Geophysical Research: Solid Earth, v. 118, p. 689-697, doi:10.1029/2012JB009358.

Lippincott, E.R., Valkenburg, A.V., Weir, C.E., and Bunting, E.N., 1958, Infrared studies on polymorphs of silicon dioxide and germanium oxide: Journal of Research of the National Bureau of Standards, v. 61, n. 1, p. 61-70.

Liu, T., 2003, Blind testing of rock varnish microstratigraphy as a chronometric indicator: results on late Quaternary lava flows in the Mojave Desert, California: Geomorphology, v. 53, p. 209-234, doi:10.1016/S0169-555X(02)00331-8.

Liu, T., and Broecker, W.S., 2000, How fast does rock varnish grow?: Geology, v. 28, n. 2, p. 183-186.

Liu, T., and Broecker, W.S., 2013, Millennial-scale varnish microlamination dating of late Pleistocene geomorphic features in the drylands of western USA: Geomorphology, v. 187, p. 38-60, doi: 10.1016/j.geomorph.2012.12.034.

Lyon, R.J.P., 1965, Analysis of rocks by spectral infrared emission (8 to 25 microns): Economic Geology, v. 60, p. 715-736.

Macholdt, D.S., et al., 2015, Microanalytical methods for in-situ high-resolution analysis of rock varnish at the micrometer to nanometer scale: Chemical Geology, v. 411, p. 57-68, doi: 10.1016/j.chemgeo.2015.06.023.

Marston, R.A., 2003, Editorial note: Geomorphology, v. 53, p. 197, doi: 10.1016/S0169-555X(02)00329-X.

McFadden, L.D., Wells, S.G., and Jercinovich, M.J., 1987, Influences of eolian and pedogenic processes on the origin and evolution of desert pavements: Geology, v. 15, p. 504-508.

Michalski, J.R., Kraft, M.D., Sharp, T.G., Williams, L.B., and Christensen, P.R., 2006, Emission spectroscopy of clay minerals and evidence for poorly crystalline aluminosilicates on Mars from Thermal Emission Spectrometer data: Journal of Geophysical Research, v. 111, n. E03004, doi: 10.1029/2005JE002438.

Moersch, J.E., and Christensen, P.R., 1995, Thermal emission from particulate surfaces: A comparison of scattering models with measured spectra: Journal of Geophysical Research, v. 100, n. E4, p. 7465-7477.

Mushkin, A., Sagy, A., Trabelci, E., Amit, R., and Porat, N., 2014, Measuring the time and scale- dependency of subaerial rock weathering rates over geologic time scales with ground-based lidar: Geology, v. 42, n. 12, p. 1063-1066, doi:10.1130/G35866.1.

Owen, L.A., Clemmens, S.J., Finkel, R.C., and Gray, H., 2014, Late Quaternary alluvial fans at the eastern end of the San Bernardino Mountains, southern California: Quaternary Science Reviews, v. 87, p. 114-134, doi: 10.1016/j.quascirev.2014.01.003.

Pazzaglia, F.J., 2013, Fluvial terraces, *in* Schroder, J., and Wohl, E., eds., Treatise on Geomorphology: Academic Press, San Diego, California, v. 9, Fluvial Geomorphology, p. 379-412, http://dx.doi.org/10.1016/B978-0-12-374739-6.00248-7.

Perry, R.S., and Adams, J.B., 1978, Desert varnish: evidence for cyclic deposition of manganese: Nature, v. 276, p. 489-491.

Perry, R.S., Lynne, B.Y., Sephton, M.A., Kolb, V.M., Perry, C.C., and Staley, J.T., 2006, Baking black opal in the desert sun: the importance of silica in desert varnish: Geology, v. 34, n. 7, p. 537-540, doi: 10.1130/G22352.1.

Philibosian, B., Fumal, T., and Weldon, R., 2011, San Andreas fault earthquake chronology and Lake Cahuilla history at Coachella, California: Bulletin of the Seismological Society of America, v. 101, n. 1, p. 13-38, doi: 10.1785/0120100050.

Porter, et al., 2011, The ShakeOut Scenario: a hypothetical M_W 7.8 earthquake of the southern San Andreas fault: Earthquake Spectra, v. 27, n. 2, p. 239-261.

Potter, R.M., and Rossman, G.R., 1977, Desert varnish: the importance of clay minerals: Science, v. 196, n. 4297, p. 1446-1448, doi: 10.1126/science.196.4297.1446.

Potter, R.M., and Rossman, G.R., 1979a, The manganese- and iron-oxide mineralogy of desert varnish: Chemical Geology, v. 25, p. 79-94.

Potter, R.M., and Rossman, G.R., 1979b, The tetravalent manganese oxides: identification, hydration, and structural relationships by infrared spectroscopy: American Mineralogist, v. 64, p. 119-1218.

Phillips, F.M., 2003, Cosmogenic ^{36}Cl ages of Quaternary basalt flows in the Mojave Desert, California, USA: Geomorphology, v. 53, p. 199-208, doi: 10.1016/S0169-555X(02)00328-8.

QGIS Development Team, 2018, QGIS Geographic Information System, Open Source Geospatial Foundation Project: https://qgis.org/en/site/ (accessed September 2017).

Quade, J., 2001, Desert pavements and associated rock varnish in the Mojave Desert: how old can they be?: Geology, v. 29, n. 9, p. 855-858.

Ramsey, M.S., and Fink, J.H., 1999, Estimating silicic lava vesicularity with thermal remote sensing: a new technique for volcanic mapping and monitoring: Bulletin of Volcanology, v. 61, p. 32-39.

Ray, T.W., and Murray, B.C., 1996, Nonlinear spectral mixing in desert vegetation: Remote Sensing of Environment, v. 55, p. 59-64.

Reheis, M.C., Slate, J.L., Throckmorton, C.K., McGeehin, J.P., Sarna-Wojcicki, A.M., and Dengler, L., 1996, Late Quaternary sedimentation on the Leidy Creek fan, Nevada-California: geomorphic responses to climate change: Basin Research, v. 12, p. 279-299.

Reneau, S.L., Raymond, R., Jr., and Harrington, C.D., 1992, Elemental relationships in rock varnish stratigraphic layers, Cima volcanic field, California: implications for varnish development and the interpretation of varnish chemistry: American Journal of Science, v. 292, p. 684-723.

Ribeiro da Luz, B., and Crowley, J.K., 2007, Spectral reflectance and emissivity features of broad leaf plants: Prospects for remote sensing in the thermal infrared (8.0-14.0 μm): Remote Sensing of Environment, v. 109, p. 393-405, doi:10.1016/j.rse.2007.01.008.

Ribeiro da Luz, B., and Crowley, J.K., 2010, Identification of plant species by using high spatial and spectral resolution thermal infrared (8.0-13.5 μm) imagery: Remote Sensing of Environment, v. 114, p. 404-413, doi:10.1016/j.rse.2009.09.019.

Rivard, B., Petroy, S.B., and Miller, J.R., 1993, Measured effects of desert varnish on the mid- infrared spectra of weathered rocks as an aid to TIMS imagery interpretation: IEEE transactions on Geoscience and Remote Sensing, v. 31, n. 1, p. 284-291.

Robitaille, P. -M., 2009, Kirchhoff's law of thermal emission: 150 years: Progress in Physics, v. 4, p. 3-13.

Salisbury, J.W., and Eastes, J.W., 1985, The effect of particle size and porosity on spectral contrast in the mid-infrared: Icarus, v. 64, p. 586-588.

Salisbury, J.W., 1986, Preliminary measurements of leaf spectral reflectance in the 8-14 μm region: International Journal of Remote Sensing, v. 7, n. 12, p. 1879-1886.

Salisbury, J.W., Walter, L.S., and Vergo, N., 1987, Mid-infrared (2.1-25 μm) spectra of minerals: First edition: United States Geological Survey Open-File Report 87-263, 389 p., https://pubs.er.usgs.gov/publication/ofr87263 (accessed April 2018).

Salisbury, J.W., and Walter, L.S., 1989, Thermal infrared (2.5-13.5 μm) spectroscopic remote sensing of igneous rock types on particulate planetary surfaces: Journal of Geophysical Research, v. 94, n. B7, p. 9192-9202.

Salisbury, J.W., Wald, A., and D'Aria, D.M., 1994, Thermal-infrared remote sensing and Kirchhoff's law 1. Laboratory measurements: Journal of Geophysical Research, v. 99, n. B6, p. 11897-11911.

Salisbury, J.W., and Wald, A., 1992, The role of volume scattering in reducing spectral contrast of Reststrahlen bands in spectra of powdered minerals: Icarus, v. 96, p. 121-128.

Schaepman-Strub, G., Schaepman, M.E., Painter, T.H., Dangel, S., and Martonchik, J.V., 2006, Reflectance quantities in optical remote sensing-definitions and case studies: Remote Sensing of Environment, v. 103, p. 27-42, doi:10.1016/j.rse.2006.03.002.

Scharer, K.M., Weldon, R.J., Fumal, T.E., and Biasi, G.P., 2007, Paleoearthquakes on the southern San Andreas fault, Wrightwood, California, 3000 to 1500 B.C.: a new method for evaluating paleoseismic evidence and earthquake horizons: Bulletin of the Seismological Society of America, v. 97, n. 4, p. 1054-1093, doi: 10.1785/0120060137.

Schneider, C.A., Rasband, W.S., and Eliceiri, K.W., 2012, NIH Image to ImageJ: 25 years of image analysis: Nature Methods, v. 9, n. 7, p. 671-675.

Shifflett, H.S., Gray, M.G., Grannell, R., and Ingram, B. L., 2002, New evidence on the slip rate, renewal time, and late Holocene surface displacement, southernmost San Andreas fault, Mecca Hills, California: Bulletin of the Seismological Society of America, v. 92, n. 7, p. 2861-2877.

Sieh, K., Stuiver, M., and Brillinger, D., 1989, A more precise chronology of earthquakes produced by the San Andreas fault in southern California: Journal of Geophysical Research, v. 94, n. B1, p. 603-623.

Sieh, K.E., and Williams, P.L., ,1990, Behavior on the southernmost San Andreas fault during the past 300 years: Journal of Geophysical Research, v. 95, n. B5, p. 6629-6645.

Simpson, S.H., 2015, Creating a data analysis plan: what to consider when choosing statistics for a study: Canadian Journal of Hospital Pharmacy, v. 68, n. 4, p. 311-317.

Spilde, M.N., Melim, L.A., Northup, D.E., and Boston, P.J., 2013, Anthropogenic lead as a tracer of rock varnish growth: Implications for rates of formation: Geology, v. 41, n. 2, p. 263-266, doi:10.1130/G33514.1.

Spinler, J.C., Bennett, R.A., Anderson, M.L., McGill, S.F., Hreinsdóttir, S., and McCallister, A., 2010, Present-day strain accumulation and slip rates associated with southern San Andreas and eastern California shear zone faults: Journal of Geophysical Research, v. 115, B11407, doi:10.1029/2010JB007424.

Sposito, G., Prost, R., and Gaultier, J.-P., 1983, Infrared spectroscopic study of adsorbed water on reduced-charge Na/Li-montmorillonites: Clays and Clay minerals, v. 31, n. 1, p. 9-16.

Thiagarajan, N., and Lee, C.-T.A., 2004, Trace-element evidence for the origin of desert varnish by direct aqueous atmospheric deposition: Earth and Planetary Science Letters, v. 224, p. 131-141, doi:10.1016/j.epsl.2004.04.038.

Thomson, J.L., and Salisbury, J.W., 1993, The mid-infrared reflectance of mineral mixtures (7-14 μm): Remote Sensing of Environment, v. 45, p. 1-13.

Ullah, S., Schlerf, M., Skidmore, A.K., and Hecker, C., 2012, Identifying plant species using mid-wave infrared (2.5-6 μm) and thermal infrared (8-14 μm) emissivity spectra: Remote Sensing of Environment, v. 118, p. 95-102, doi:10.1016/j.rse.2011.11.008.

Van de Kamp, P.C., 1973, Holocene continental sedimentation in the Salton basin, California: a reconnaissance: Geological Society of America Bulletin, v. 84, p. 827-848.

van der Woerd, J., Klinger, Y., Sieh, K., Tapponnier, P., Ryerson, F.J., and Mériaux, A.-S., 2006, Long-term slip rate of the southern San Andreas Fault from ^{10}Be-^{26}Al surface exposure dating of an offset alluvial fan: Journal of Geophysical Research, v. 111, n. B04407, doi:10.1029/2004JB003559.

Watchman, A., 2000, A review of the history of dating rock varnishes: Earth-Science Reviews, v. 49, p. 261-277.

Wells, S.G., Dohrenwend, J.C., McFadden, L.D., Turrin, B.D., and Mahrer, K.D., 1985, Late Cenozoic landscape evolution on lava flow surfaces of the Cima volcanic field, Mojave Desert, California: Geological Society of America Bulletin, v. 96, p. 1518-1529.

Wells, S.G., McFadden, L.D., Poths, J., and Olinger, C.T., 1995, Cosmogenic ^{3}He surface-exposure dating of stone pavements: Implications for landscape evolution in deserts: Geology, v. 23, n. 7, p. 613-616.

Whitley, D.S., and Dorn, R.I., 1987, Rock art chronology in eastern California: World Archaeology, v. 19, n. 2, p. 150-164, doi: 10.1080/00438243.1987.9980031.

Young, S.J., Johnson, B.R., and Hackwell, J.A., 2002, An in-scene method for atmospheric compensation of thermal hyperspectral data: Journal of Geophysical Research, v. 107, no. D24, p. 4774-4793.

Yule, D., 2009, The enigmatic San Gorgonio Pass: Geology, v. 37, n. 2, p. 191-192, doi: 10.1130/focus022009.1

FIGURE CAPTIONS

Figure 1 (p. 349): Overview map of the study area, which is located in the Coachella Valley of southern California. Base map is Google Earth satellite imagery in true color (imagery date: 14 July 2016). Image was annotated to show the main strands of the southern San

Andreas fault (arrows represent relative fault motion), which is the main boundary between the Pacific and North American tectonic plates at this location. The rectangle is the footprint of the thermal hyperspectral airborne imagery used for this research. Interstate 10, and the Palm Springs International Airport are shown for geographic markers. BP: Biskra Palms; IH: Indio Hills; PC: Pushawalla Canyon; SAF-B: San Andreas fault, Banning strand; SAF-MC: San Andreas fault, Mission Creek strand; THAIF: thermal hyperspectral airborne imagery footprint; TPO: Thousand Palms Oasis.

Figure 2 (p. 350): Examples of laboratory thermal infrared emission spectra, and linear spectral mixture models for minerals relevant to this research. Spectra used here are from the library of Christensen et al. (2000), and mineral names are accompanied by the sample numbers (in parentheses) from that library. We used the linear "checkerboard" model (Christensen and Harrison, 1993) to calculate spectra for the mixtures shown. (A) Single tectosilicate mineral components combined to make a synthetic "granite," which represents a typical desert varnish coating substrate lithology found in the study area. Ratio of quartz/andesine/microcline is 33/34/33, and particle size ranges are: quartz = 125-2000 μm; andesine = 710-1000 μm; microcline = 710-1000 μm. (B) Montmorillonite clay (proxy for desert varnish coating) combined with the "granite" substrate to model the anticipated effect of a progressively heavier desert varnish coating ("granite/mont" is the mixing ratio for the two endmember components). The clay's major absorption feature at 9.36 um begins to dominate the spectrum as more is added to the mixture. The montmorillonite sample was a pressed pellet (Cooper and Mustard, 1999, noted that clay crystal aggregates behave spectrally like larger particles). (C) Field photograph (for scale, hammer is 33 cm long) that

exemplifies the variable degree of varnish development observed on clasts. Some of the clasts are circled and labeled to relate physical specimens to the spectral models shown in (A) and (B): the synthetic "granite" spectrum could represent the clast labeled "'granite' endmember" (which is not varnished); the granite/mont = 67/33 (or 33/67) spectra could represent the clasts labeled "intermediate mixtures" (which have light/moderate varnish); and the montmorillonite spectrum could represent the clast labeled "montmorillonite endmember" (i.e., with its heavy varnish coating, a spectrum of this clast might resemble the spectrum for montmorillonite clay, which can be a significant component in a typical varnish, see text for further explanation and references). As heavier varnish coatings tend to have greater physical thickness, a roughly linear relationship between increasing spectral band depth and varnish thickness has been observed in laboratory spectra of varnish-coated samples (Christensen and Harrison, 1993), which supports the linear spectral mixture models in (A) and (B).

Figure 3 (p. 351): Thermal hyperspectral airborne imagery of the Thousand Palms Oasis area, Coachella Valley, southern California (for larger spatial context, imagery footprint can be seen in Figure 1). The complete image scene is shown here, and displayed in false colors assigned to band ratios, which remove the effects of varying illumination due to topography (Kahle et al., 1980; Gillespie et al., 1987). Band ratio assignments are: red, 11.1/9.5; green, 11.5/9.1; blue, 12.4/8.6 (all values are wavelengths in microns). The false color assignments highlight geological features (such as the varnish we are studying), and other forms of land surface cover. General false color interpretation is as follows: red represents younger sediments, green represents older varnished surfaces, and blue represents vegetation. Thick

black lines are faults: only the main splays are shown here, so the imagery is not overly obscured. Arrows indicate relative fault motion. PC: Pushawalla Canyon; SAFMCS: San Andreas fault, Mission Creek strand; SAFBS: San Andreas fault, Banning strand; TPO: Thousand Palms Oasis. Lower left photograph is of Mako, the Aerospace Corporation's thermal hyperspectral sensor, mounted in the belly of an airplane and ready to fly (photo taken by David Tratt). Mako is essentially a large camera that takes aerial images of thermal radiation emitted by land surfaces. Lower left illustration shows the Mako sensor's viewing geometry. Base map is an SRTM 1 arc-second DEM hillshade (from the USGS Earth Resources Observation and Science website, https://eros.usgs.gov/, accessed on 09/02/2017). Map was produced using QGIS software (QGIS, 2018).

Figure 4 (p. 352): Same as Figure 3, but with color-coded digitized polygons for the mapped and dated geomorphic surfaces (Kate Scharer, personal communication; Blisniuk and Sharp, 2014) that we used for this research. The surface ages were derived with a combination of methods: cosmogenic exposure (beryllium-10) dating, and also uranium-series dating (ages shown in lower left key; ka: kiloannum). To the north east, upstream from where the San Andreas fault, Mission Creek strand, intersects Pushawalla Canyon, we grouped the cluster of surfaces for analyses, and we referred to this group as the "upstream" set of surfaces (or surface deposits). Similarly, to the south west, downstream from the San Andreas fault, Mission Creek strand, we grouped all of these other surfaces, and referred to this group as the "downstream" set of surfaces (or surface deposits).

Figure 5 (p. 353): Airborne remote sensing emissivity spectra of the geomorphic surfaces (for surface names and ages, see Table 1, for locations, see Figure 4). To display spectral variability, there are five subsets of randomly generated spectra for each of the upstream and downstream sets of surfaces (single spectra shown here are the average of multiples, see text). The continuum has been removed from all spectra, and they were also smoothed over a three band interval.

Figure 6 (p. 354): Airborne spectra band depth at 9.16 μm versus surface age. Error bars in surface age are from values in Table 1. Error bars in band depth are from the standard deviation of values calculated from all of the spectra in Figure 5.

Figure 7 (p. 355): Dominant (>50% relative abundance) clast size range plots for field sites on the upstream (upper panel) and downstream (lower panel) sets of surfaces. Clast sizes were not measured at the downstream sites C3sand and C3veg.

Figure 8 (p. 356): Desert varnish scores for field sites on the upstream (upper panel) and downstream (lower panel) sets of surfaces. A higher number is a greater degree of development, as follows: 1 = absent/rare, 2 = light/weak, 3 = moderate, and 4 = heavy/strong.

Figure 9 (p. 357): Desert pavement scores for field sites on the upstream (upper panel) and downstream (lower panel) sets of surfaces. A higher number is a greater degree of development, as follows: 1 = absent/rare, 2 = light/weak, 3 = moderate, and 4 = heavy/strong.

Figure 10 (p. 358): Vegetation spacing estimates for field sites on the upstream (upper panel) and downstream (lower panel) sets of surfaces. The values for upstream sites Qt0p1 and Qt0p2 are off the chart, and noted numerically (30 and 50 m, respectively). The higher spacing means that older surfaces are less vegetated.

Figure 11 (p. 359): "Rock" area fraction values for field sites on the upstream (upper panel) and downstream (lower panel) sets of surfaces. Values are minimums, in percent.

Figure 12 (p. 360): Upstream field site Qt4p1 (<11.3 ka). (A) sample square meter field photograph (frame is 1 meter on edge, with a thickness of 2.5 cm). Site name/age seen on clipboard (lower right) is obsolete. Gray card (upper right) is present for a potential color analysis that was not completed for this study. Clasts on clipboard and gray card are not representative, but were placed to secure items from heavy wind. (B) Site overview field photograph (sample frame is 1 meter on edge). (C) Ground-based spectra are from sand and vegetation samples. Site name and age are in the upper right corner. The final, thicker spectrum is the site average (arithmetic mean) for all spectra.

Figure 13 (p. 361): Downstream field site C0p1 (>94.5 ka). (A) sample square meter field photograph (frame is 1 meter on edge, with a thickness of 2.5 cm). Site name/age seen on clipboard (lower right) is obsolete. Gray card (upper right) is present for a potential color analysis that was not completed for this study. Clasts on clipboard and gray card are not representative, but were placed to secure items from heavy wind. (B) Site overview field photograph (sample frame is 1 meter on edge). (C) Ground-based spectra are from arbitrarily

chosen lithologic clast samples that were distributed across the sampling area. Site name and age are in the upper right corner. The final, thicker spectrum is the site average (arithmetic mean) for all spectra.

Figure 14 (p. 362): Airborne (blue) and ground-based (red) spectra plotted on the same axes to show the systematic difference in shape and position of the emissivity minimum for each of the data sets. The emissivity minimum is at 9.16 μm in airborne spectra, and 9.30 μm in ground-based spectra. Airborne spectra are from Figure 5: "Airborne 1" is Qt0 (>95 ka), from the second of the five (counting down from the top) upstream sets, and "Airborne 2" is C0 (>95 ka), from the first of the five downstream sets. "Ground 1" is the field site Qt0p2 (>95 ka, Figure S10) average spectrum, and "Ground 2" is the field site C0p1 (>95 ka, Figure 13) average. For the most direct comparison, we performed the exact same processing steps on the ground-based spectra as we did on the airborne spectra (ground-based spectra resampled to the airborne wavelengths, continuum removal performed, then smoothed). We also vertically scaled (stretched) all of the spectra shown here to the one that had the greatest emissivity range (which was Qt0p2).

Figure 15 (p. 363): Summary of correlation coefficients between each parameter and surface age. All values are R^2, except for those for desert varnish and desert pavement scores, which are Spearman's rank correlation coefficient (used for categorical variables, see Simpson, 2015). Exact numerical values are in Table 3.

TABLES

Table 1: Geomorphic surface names and ages[1]			
Surface names			
Upstream[2]	Downstream[2]	Age (ka)	Age (ka) used in text[3]
Qt4	-	<11.3	<11
Qt3	C3	12.7 ± 1.4	13
-	C2f	26.00 ± 7.55	26
Qt2	C2	74.40 ± 5.15	74
Qt1	C1	87.3 ± 7.2	87
Qt0	C0	>94.5	>95

[1]Names and ages are from Blisniuk and Sharp (2014), and Kate Scharer, personal communication. See Table 4 in Owen et al. (2014) for a detailed comparison of the nomenclature of geomorphic surfaces and their ages, and how they compare from area to area in the desert southwest.
[2]Upstream and downstream are relative to the Mission Creek strand of the southern San Andreas fault, see Figures 3 and 4.
[3]In most cases where the name of a surface is cited in the text, the age is also included for reference, with the age rounded to the nearest whole number, in ka units, and the uncertainty discarded, for brevity.

Table 2: Summary of ground-based spectra							
Field site	Age (ka) used in text[1]	GPS easting[2]	GPS northing[2]	Single clast spectra #'s	"Sand"[3] spectra #'s	Vegetation spectra #'s	Total usable spectra (not including site average)
Qt4p1[4]	<11	0566905	3743636	-	1-5	6-10	10
Qt4p2	<11	0566647	3743466	1-10	-	-	10
Qt3p1	13	0566949	3743509	1-10	-	-	10
Qt3p2	13	0566794	3743443	1-9	-	-	9
Qt2p1	74	0567024	3743301	1-10	-	-	10
Qt2p2	74	0567019	3743375	2-9	-	1	9
Qt1p1	87	0567179	3743334	1-10	-	-	10
Qt1p2	87	0567122	3743351	1-9	-	-	9
Qt0p1	>95	0567424	3743166	1-10	-	-	10
Qt0p2	>95	0567455	3742949	1-10	-	-	10
C3p1	13	0564570	3741612	2-7	1,8,9	-	9
C3p2	13	0565467	3742974	1-9	-	-	9
C3sand	13	0564681	3741973	-	1-10	-	10
C3veg	13	0565037	3742861	-	-	1-4	4
C2fp1	26	0565089	3743300	1-10	-	-	10
C2fp2	26	0564947	3743239	1-8	-	-	8
C2fp3	26	0564803	3743250	1-10	-	-	10
C2fp4	26	0564885	3743129	1-3	4-9	-	9
C2p1	74	0564630	3742626	1-10	-	-	10
C2p2	74	0564533	3742720	1-9	-	-	9
C2p3	74	0564731	3743148	1-9	-	-	9
C2p4	74	0564482	3743238	1-10	-	-	10
C1p1	87	0564226	3743652	1-9	-	-	9
C1p2	87	0564299	3743682	1-10	-	-	10
C0p1[5]	>95	0564320	3743216	1-10	-	-	10
C0p2	>95	0564223	3743046	1-10	-	-	10
C0p3	>95	0564039	3743231	1-10	-	-	10

[1]See Table 1.
[2]All GPS locations are given in UTM coordinates, zone 11S.
[3]"Sand" refers to spectra measured from samples of finer, unconsolidated lithologic detrital material, and does not imply a technical definition of grain size.
[4]Figure 12.
[5]Figure 13.

Table 3: Summary of correlation coefficients[1] between each parameter and surface age	
Parameter (units)	Correlation coefficient
Mean of dominant (>50%) clast size ranges (cm)	0.10
Varnish score (dimensionless)[2]	0.90
Pavement score (dimensionless)[2]	0.90
Vegetation spacing (m)	0.34
“Rock” area fraction (percent)	0.00
Airborne spectra band depth at 9.16 μm (emissivity, dimensionless)	0.59
Ground-based spectra band depth at 9.30 μm (emissivity, dimensionless)	0.04

[1]All values are R^2, unless otherwise specified.
[2]Spearman’s rank correlation coefficient.

FIGURES

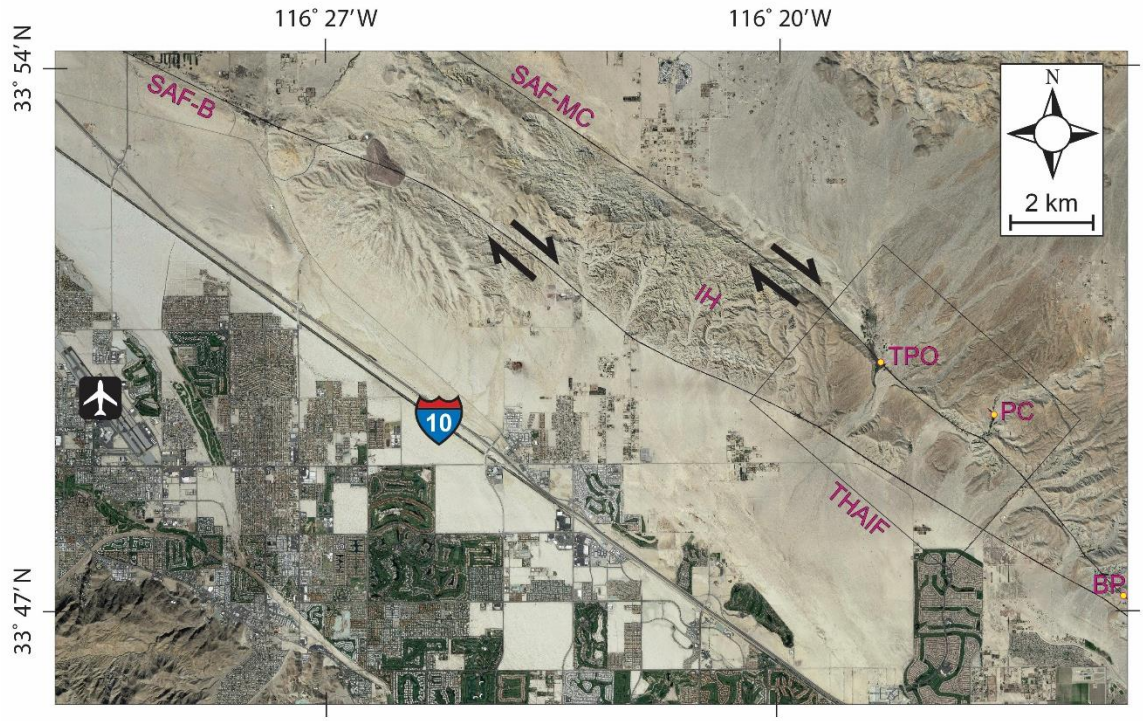

Figure 1

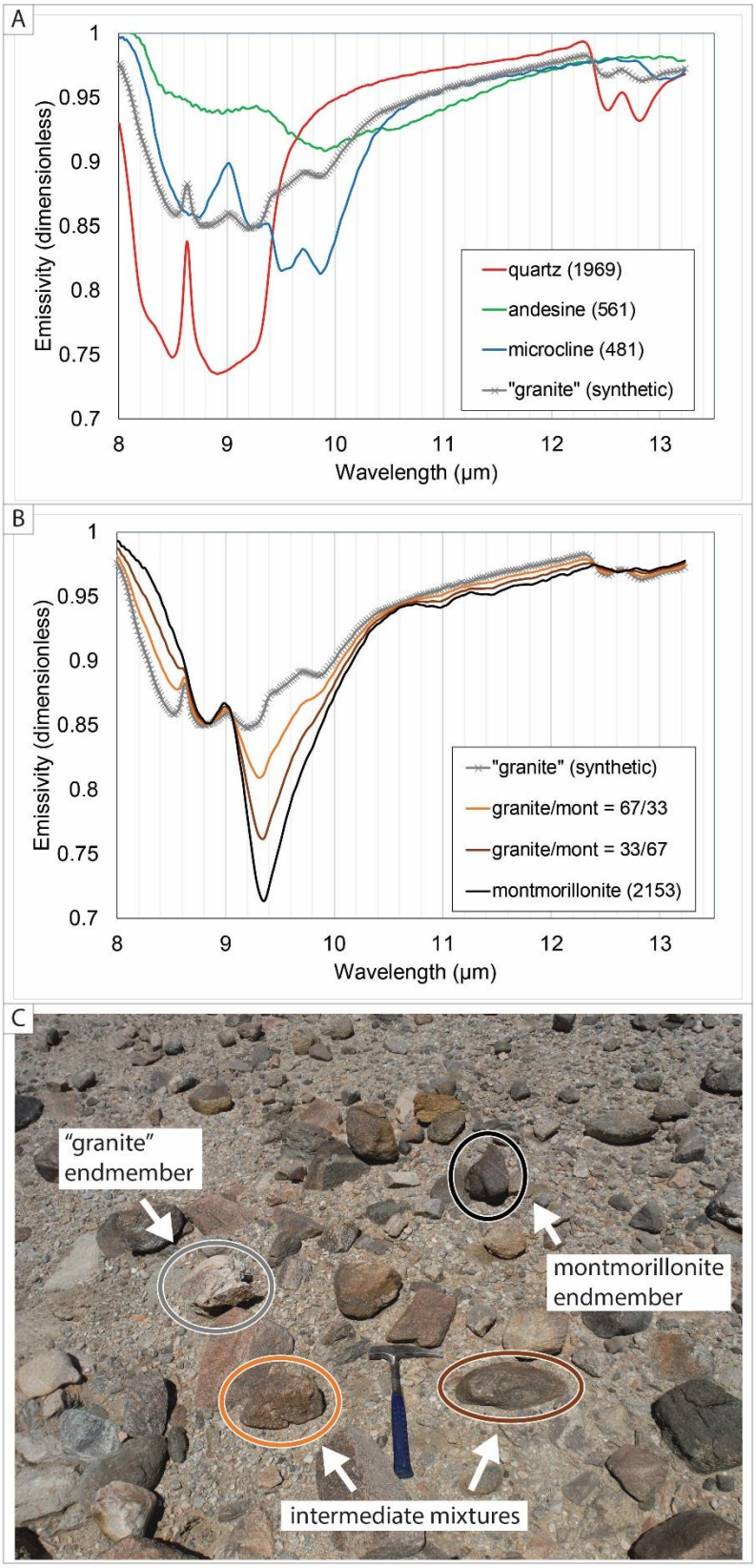
A
Emissivity (dimensionless)
1
0.95
0.9
0.85
0.8
0.75
0.7
8
9
10
11
12
13
Wavelength (μm)
quartz (1969)
andesine (561)
microcline (481)
"granite" (synthetic)
B
Emissivity (dimensionless)
Wavelength (μm)
"granite" (synthetic)
granite/mont = 67/33
granite/mont = 33/67
montmorillonite (2153)
C
"granite" endmember
montmorillonite endmember
intermediate mixtures

Figure 2

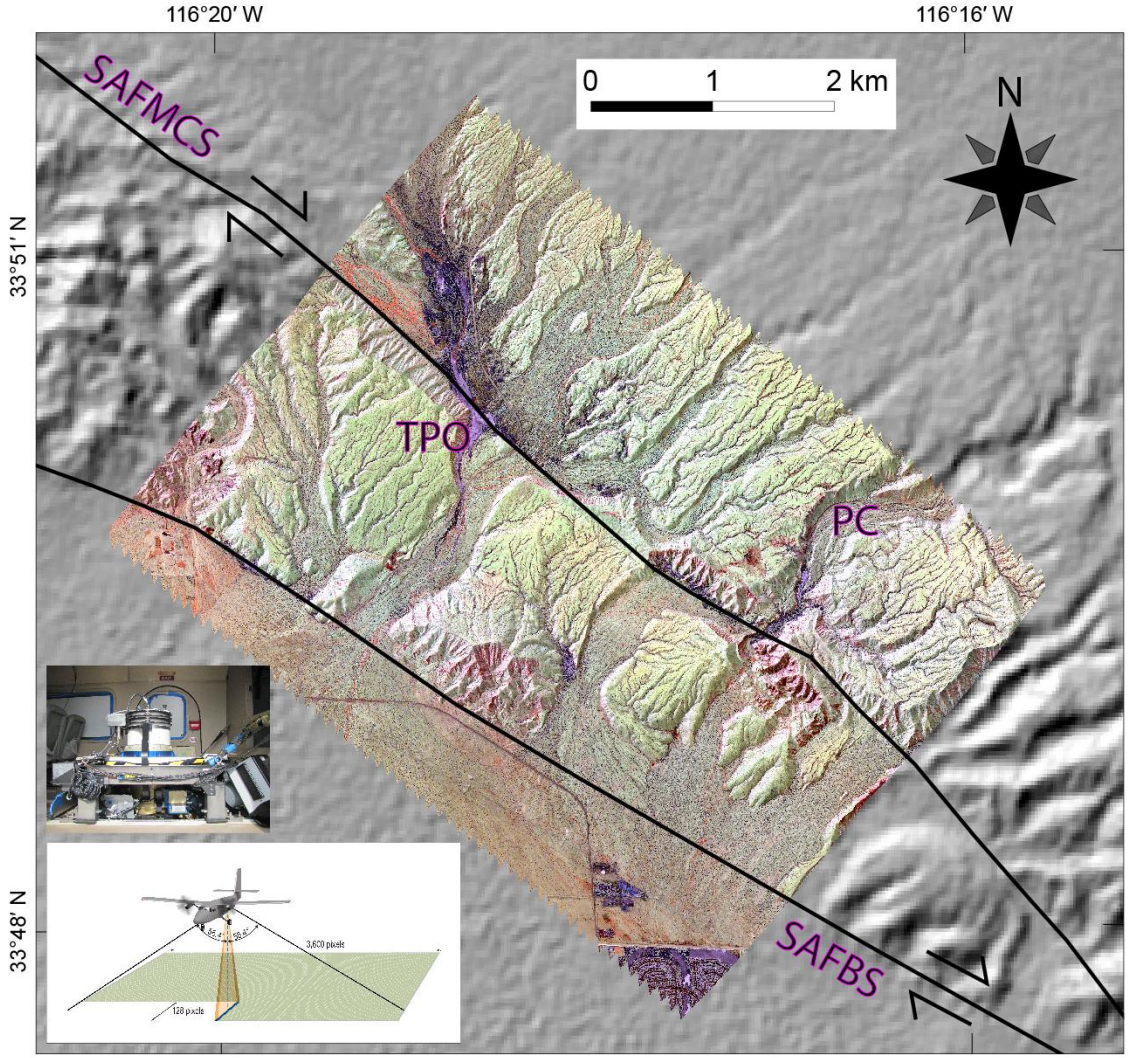
116°20′ W
116°16′ W
33°51′ N
33°48′ N
SAFMCS
TPO
PC
SAFBS
0
1
2 km
N
3,600 pixels
128 pixels

Figure 3

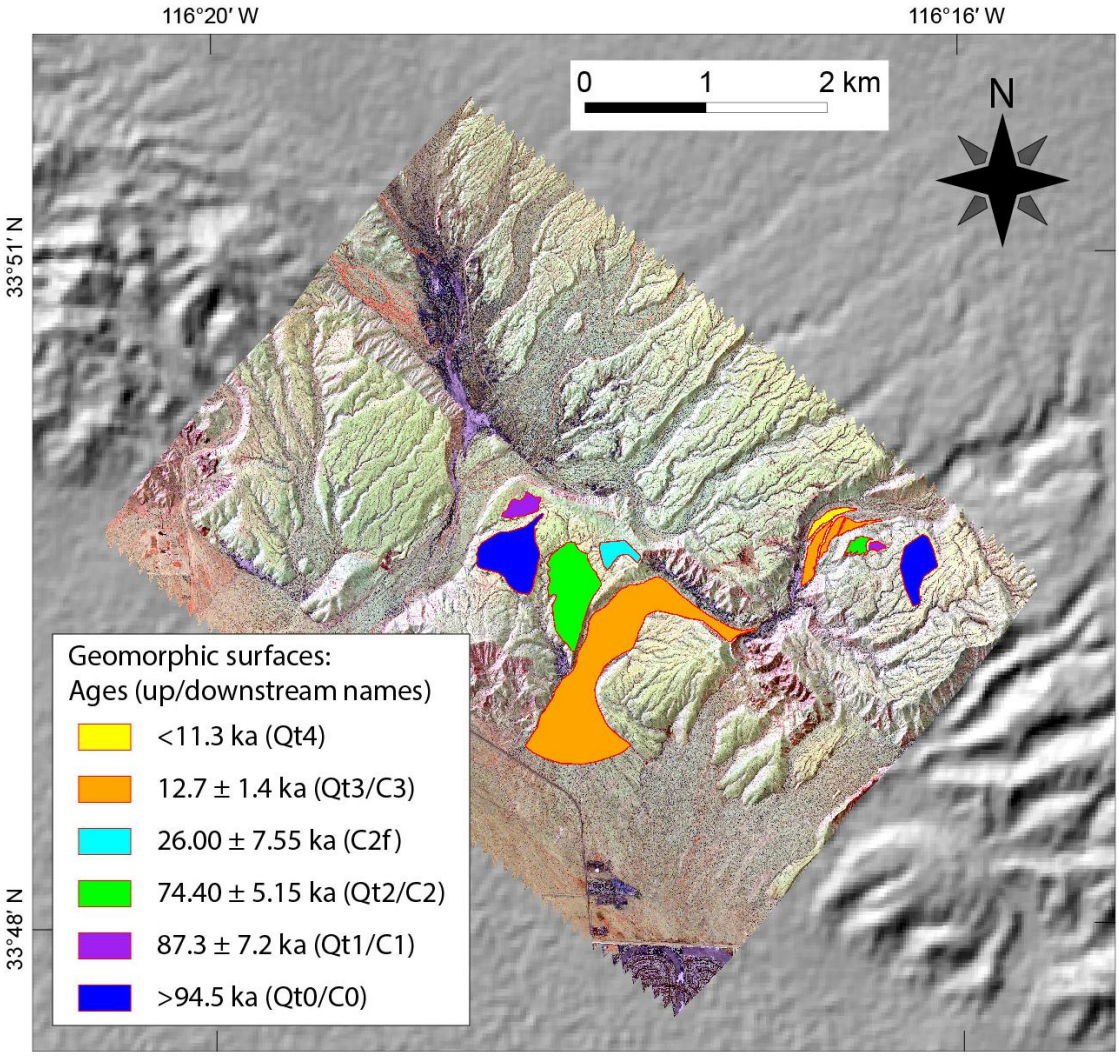
116°20′ W
116°16′ W
33°51′ N
33°48′ N
0
1
2 km
N
Geomorphic surfaces:
Ages (up/downstream names)
<11.3 ka (Qt4)
12.7 ± 1.4 ka (Qt3/C3)
26.00 ± 7.55 ka (C2f)
74.40 ± 5.15 ka (Qt2/C2)
87.3 ± 7.2 ka (Qt1/C1)
>94.5 ka (Qt0/C0)

Figure 4

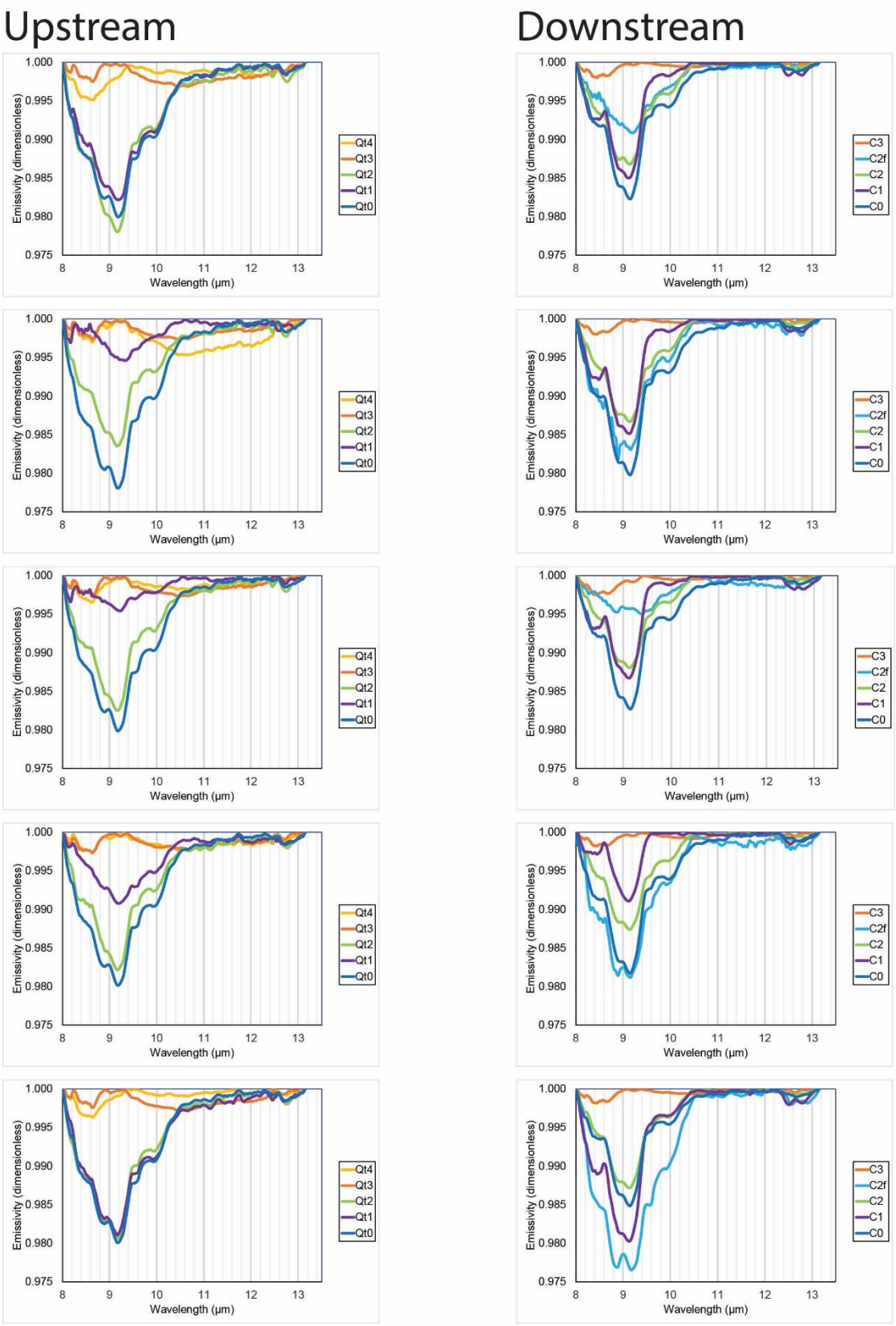
Upstream
Downstream
Emissivity (dimensionless)
Wavelength (μm)
1.000
0.995
0.990
0.985
0.980
0.975
8
9
10
11
12
13
Qt4
Qt3
Qt2
Qt1
Qt0
C3
C2f
C2
C1
C0

Figure 5

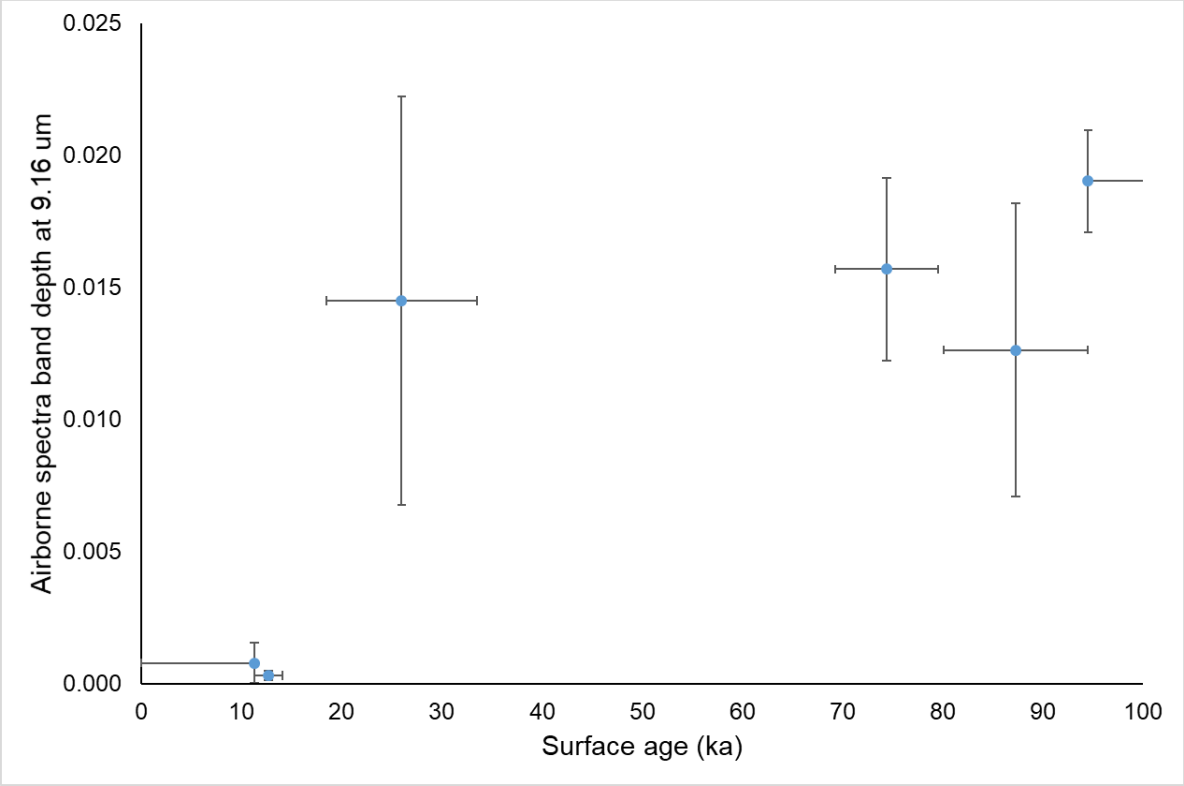
0.025
0.020
0.015
0.010
0.005
0.000
Airborne spectra band depth at 9.16 um
0
10
20
30
40
50
60
70
80
90
100
Surface age (ka)

Figure 6

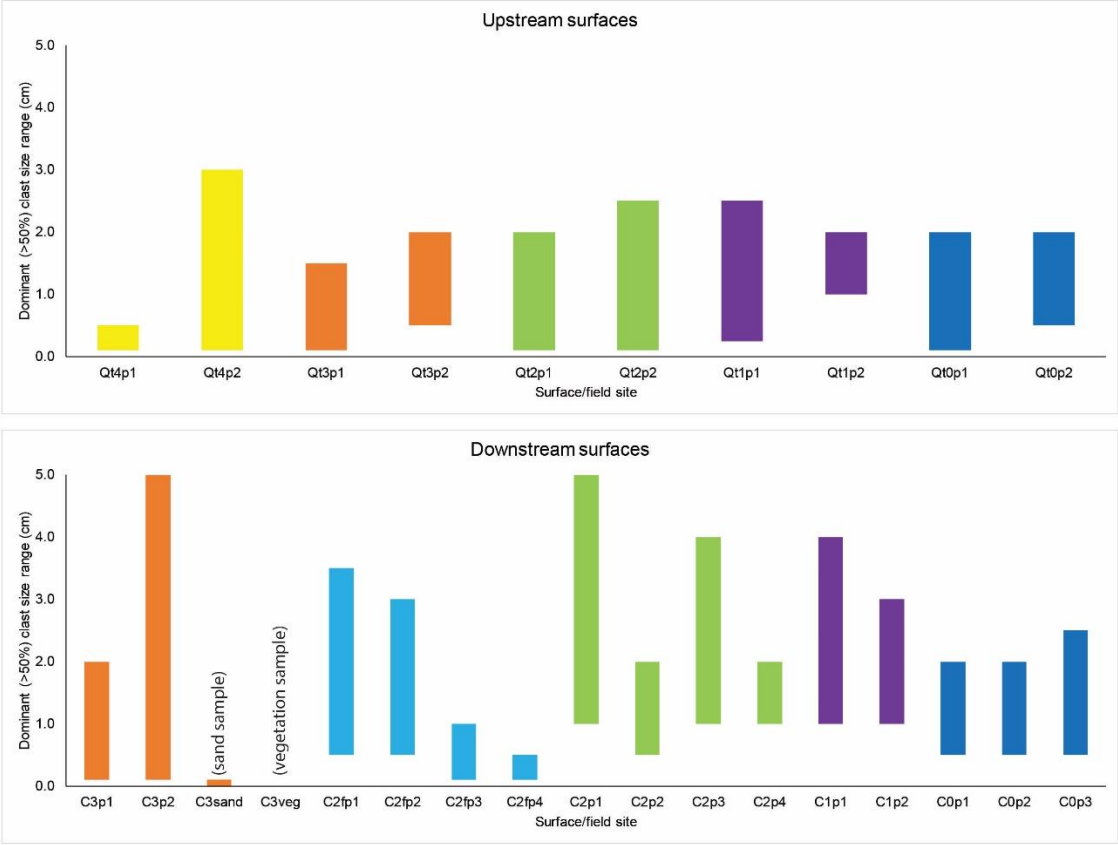
Upstream surfaces
Dominant (>50%) clast size range (cm)
5.0
4.0
3.0
2.0
1.0
0.0
Qt4p1
Qt4p2
Qt3p1
Qt3p2
Qt2p1
Qt2p2
Qt1p1
Qt1p2
Qt0p1
Qt0p2
Surface/field site
Downstream surfaces
Dominant (>50%) clast size range (cm)
(sand sample)
(vegetation sample)
C3p1
C3p2
C3sand
C3veg
C2fp1
C2fp2
C2fp3
C2fp4
C2p1
C2p2
C2p3
C2p4
C1p1
C1p2
C0p1
C0p2
C0p3
Surface/field site

Figure 7

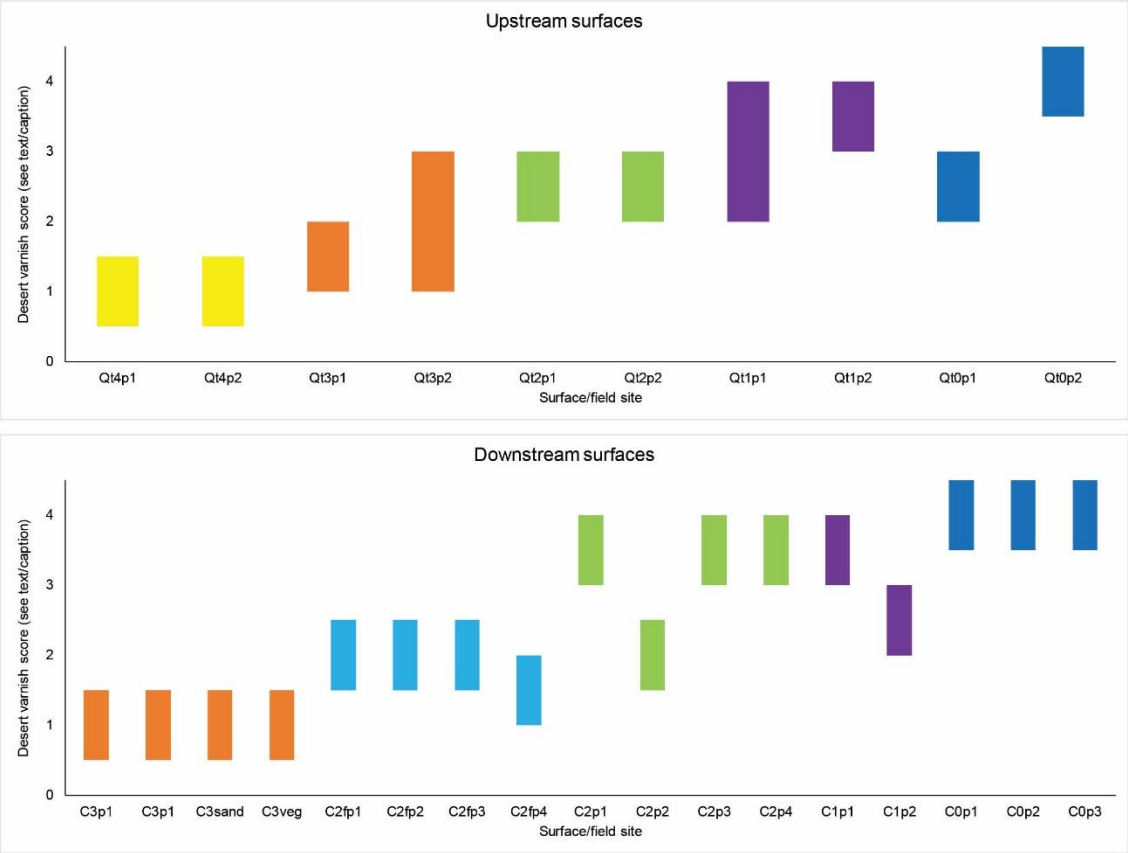
Upstream surfaces
Desert varnish score (see text/caption)
0
1
2
3
4
Qt4p1
Qt4p2
Qt3p1
Qt3p2
Qt2p1
Qt2p2
Qt1p1
Qt1p2
Qt0p1
Qt0p2
Surface/field site
Downstream surfaces
Desert varnish score (see text/caption)
0
1
2
3
4
C3p1
C3p1
C3sand
C3veg
C2fp1
C2fp2
C2fp3
C2fp4
C2p1
C2p2
C2p3
C2p4
C1p1
C1p2
C0p1
C0p2
C0p3
Surface/field site

Figure 8

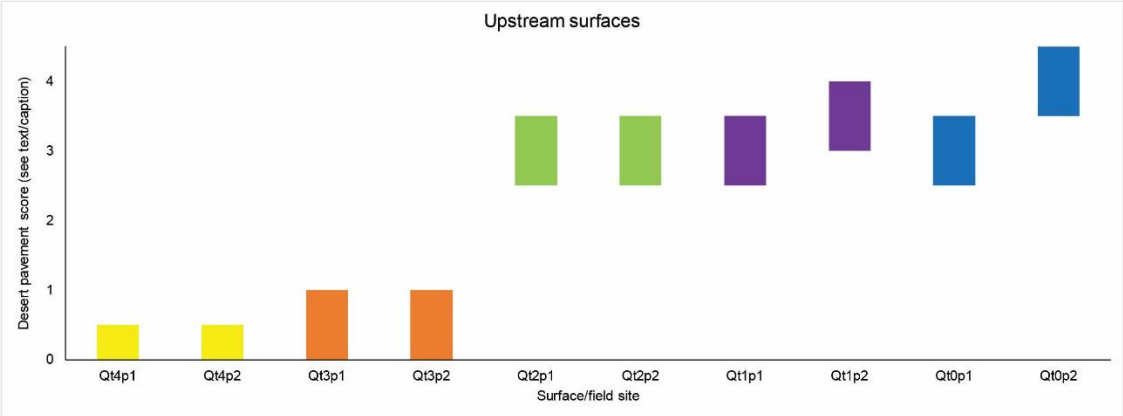
Upstream surfaces
Desert pavement score (see text/caption)
0
1
2
3
4
Qt4p1
Qt4p2
Qt3p1
Qt3p2
Qt2p1
Qt2p2
Qt1p1
Qt1p2
Qt0p1
Qt0p2
Surface/field site

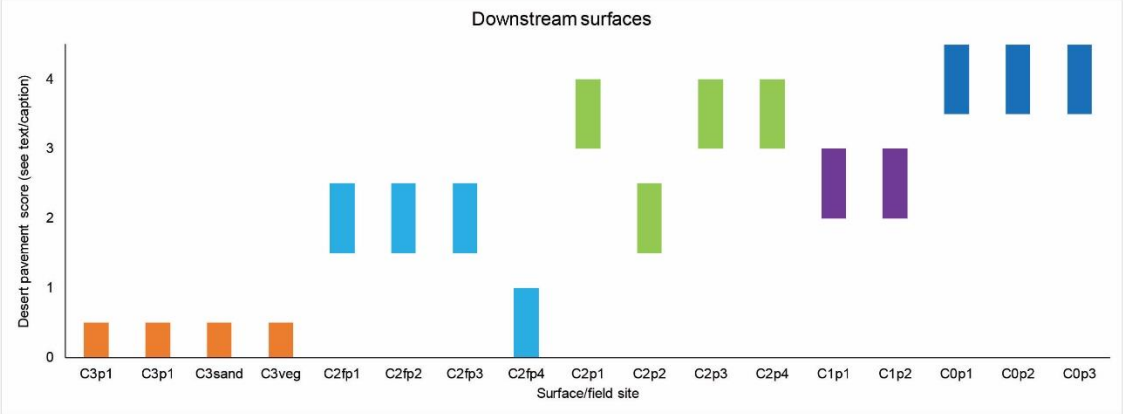
Downstream surfaces
Desert pavement score (see text/caption)
0
1
2
3
4
C3p1
C3p1
C3sand
C3veg
C2fp1
C2fp2
C2fp3
C2fp4
C2p1
C2p2
C2p3
C2p4
C1p1
C1p2
C0p1
C0p2
C0p3
Surface/field site

Figure 9

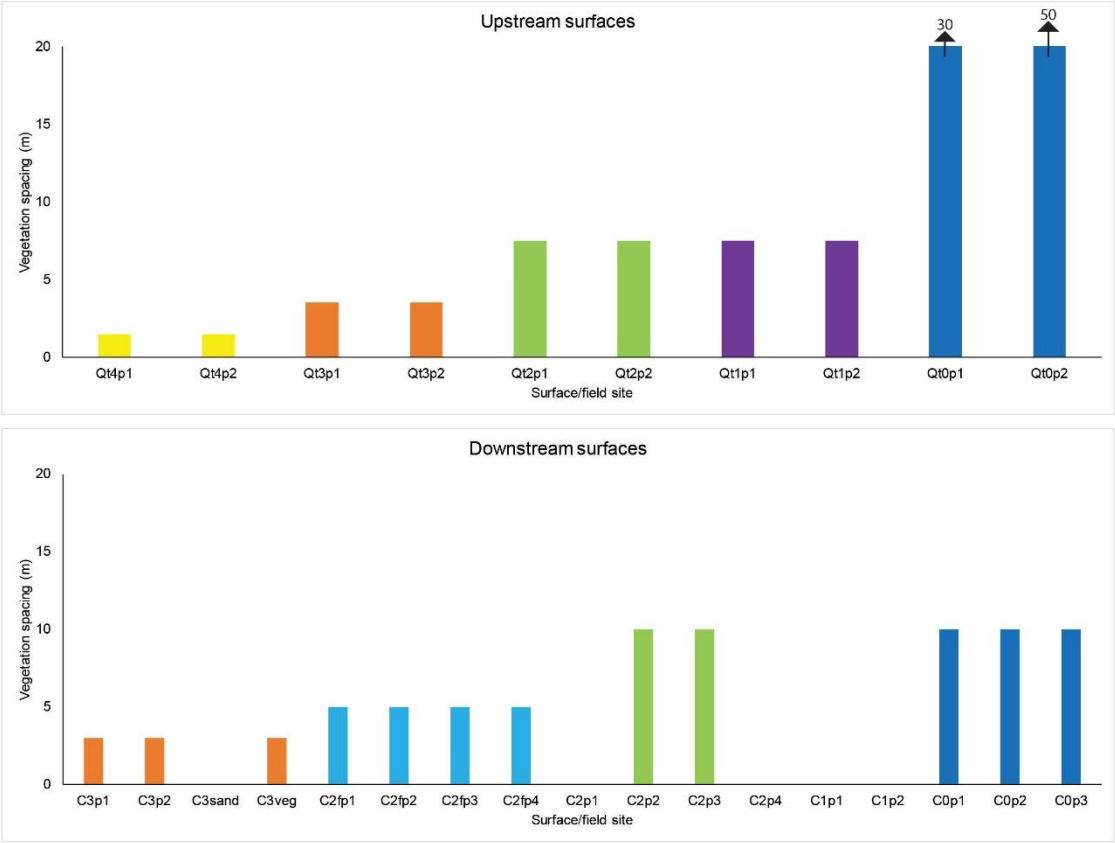
Upstream surfaces
Vegetation spacing (m)
20
15
10
5
0
30
50
Qt4p1
Qt4p2
Qt3p1
Qt3p2
Qt2p1
Qt2p2
Qt1p1
Qt1p2
Qt0p1
Qt0p2
Surface/field site
Downstream surfaces
Vegetation spacing (m)
20
15
10
5
0
C3p1
C3p2
C3sand
C3veg
C2fp1
C2fp2
C2fp3
C2fp4
C2p1
C2p2
C2p3
C2p4
C1p1
C1p2
C0p1
C0p2
C0p3
Surface/field site

Figure 10

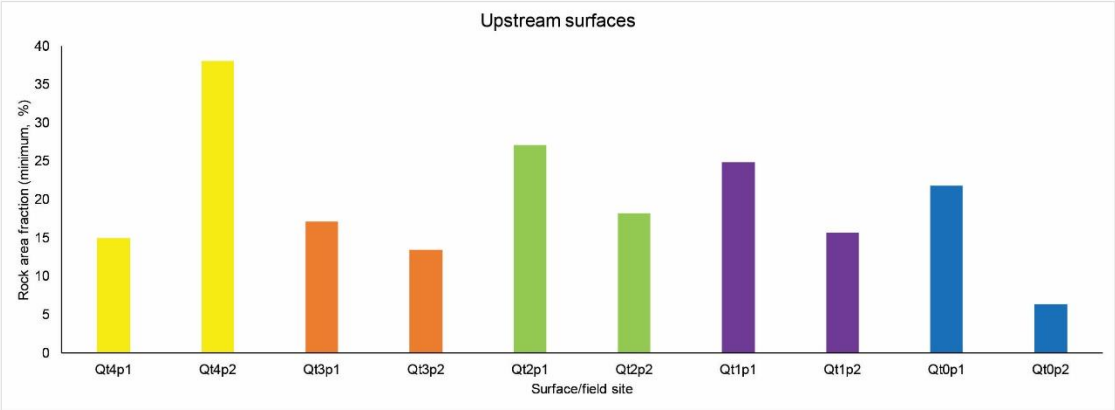
Upstream surfaces
Rock area fraction (minimum, %)
0
5
10
15
20
25
30
35
40
Qt4p1
Qt4p2
Qt3p1
Qt3p2
Qt2p1
Qt2p2
Qt1p1
Qt1p2
Qt0p1
Qt0p2
Surface/field site

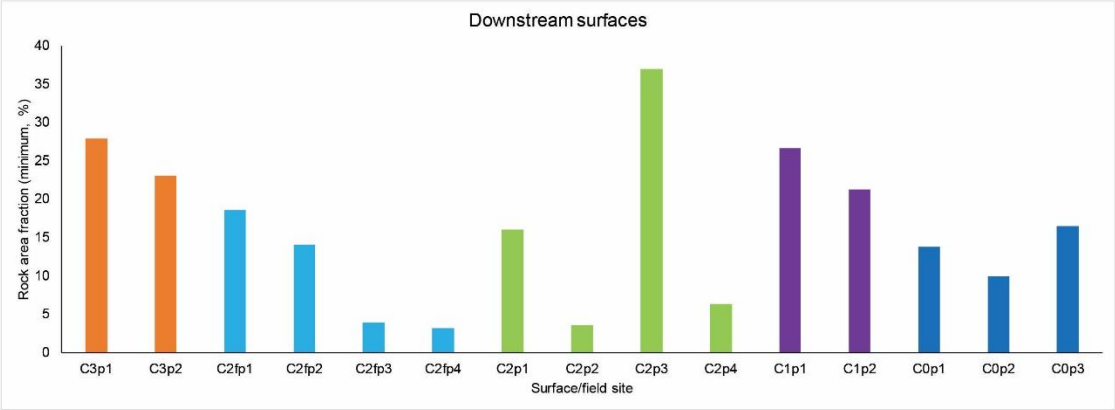
Downstream surfaces
Rock area fraction (minimum, %)
0
5
10
15
20
25
30
35
40
C3p1
C3p2
C2fp1
C2fp2
C2fp3
C2fp4
C2p1
C2p2
C2p3
C2p4
C1p1
C1p2
C0p1
C0p2
C0p3
Surface/field site

Figure 11

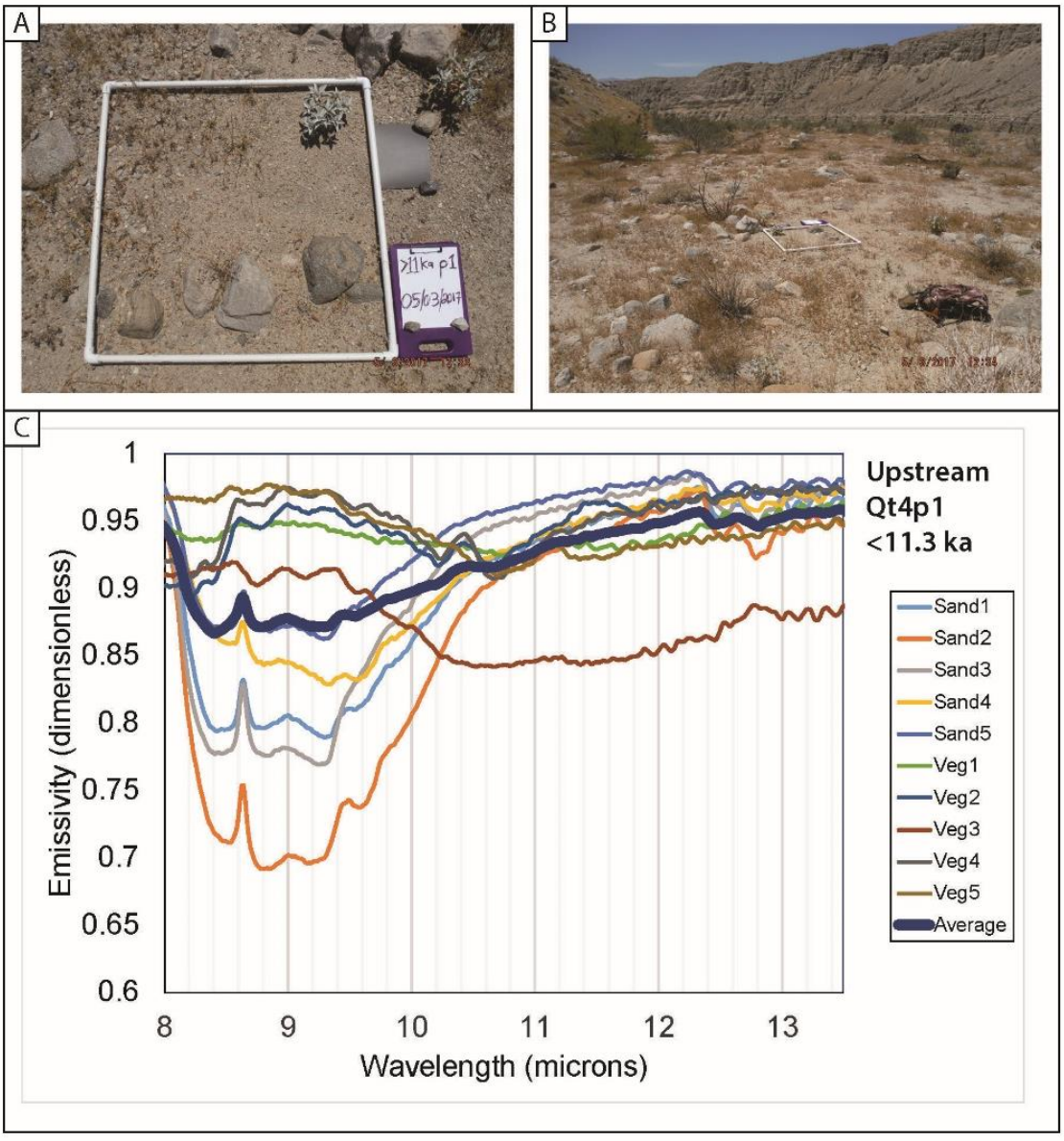
A
B
C
Upstream
Qt4p1
<11.3 ka
Emissivity (dimensionless)
Wavelength (microns)
1
0.95
0.9
0.85
0.8
0.75
0.7
0.65
0.6
8
9
10
11
12
13
Sand1
Sand2
Sand3
Sand4
Sand5
Veg1
Veg2
Veg3
Veg4
Veg5
Average

Figure 12

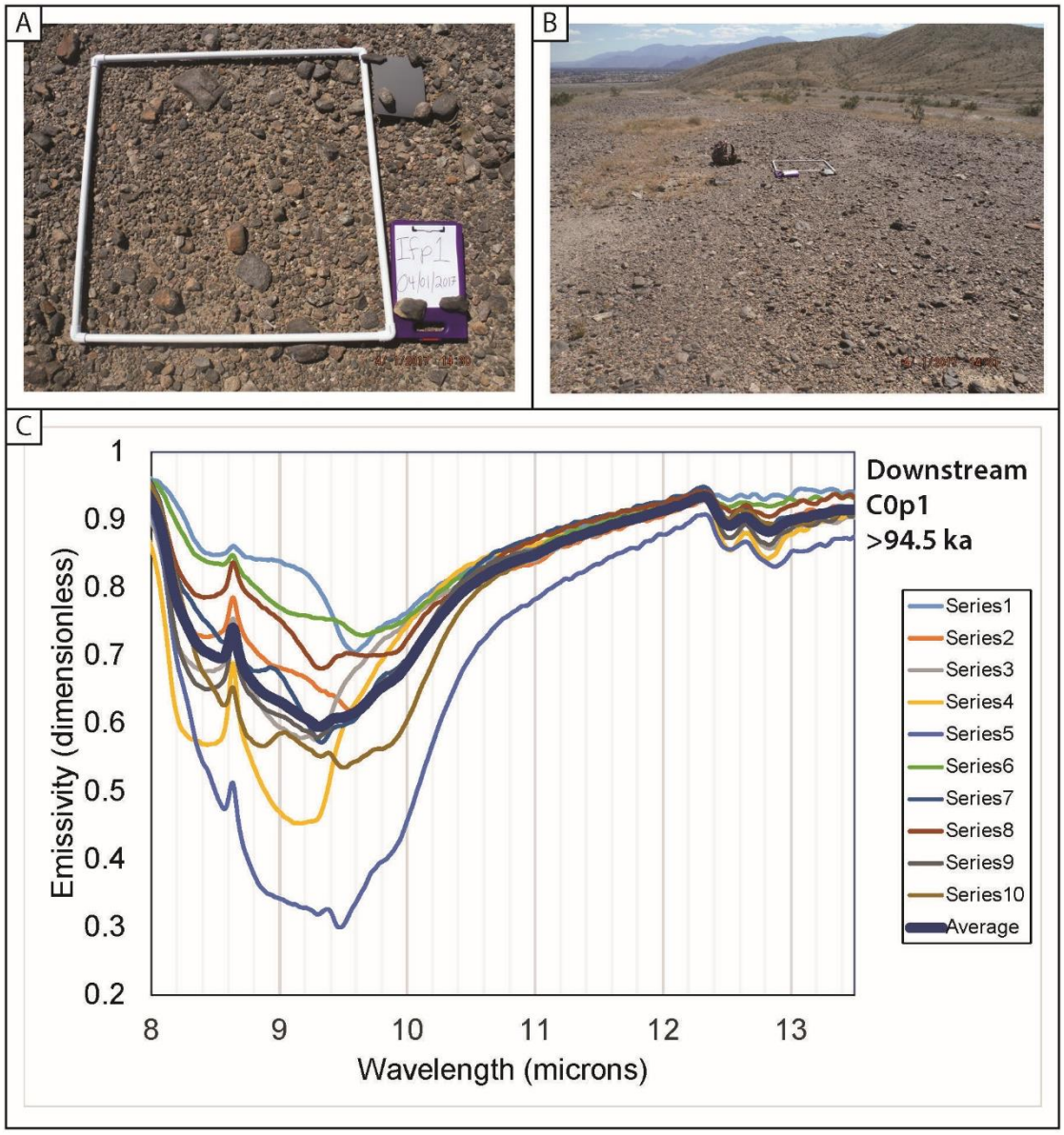
A
B
C
IFp1
04/01/2017
Downstream
C0p1
>94.5 ka
Emissivity (dimensionless)
1
0.9
0.8
0.7
0.6
0.5
0.4
0.3
0.2
8
9
10
11
12
13
Wavelength (microns)
Series1
Series2
Series3
Series4
Series5
Series6
Series7
Series8
Series9
Series10
Average

Figure 13

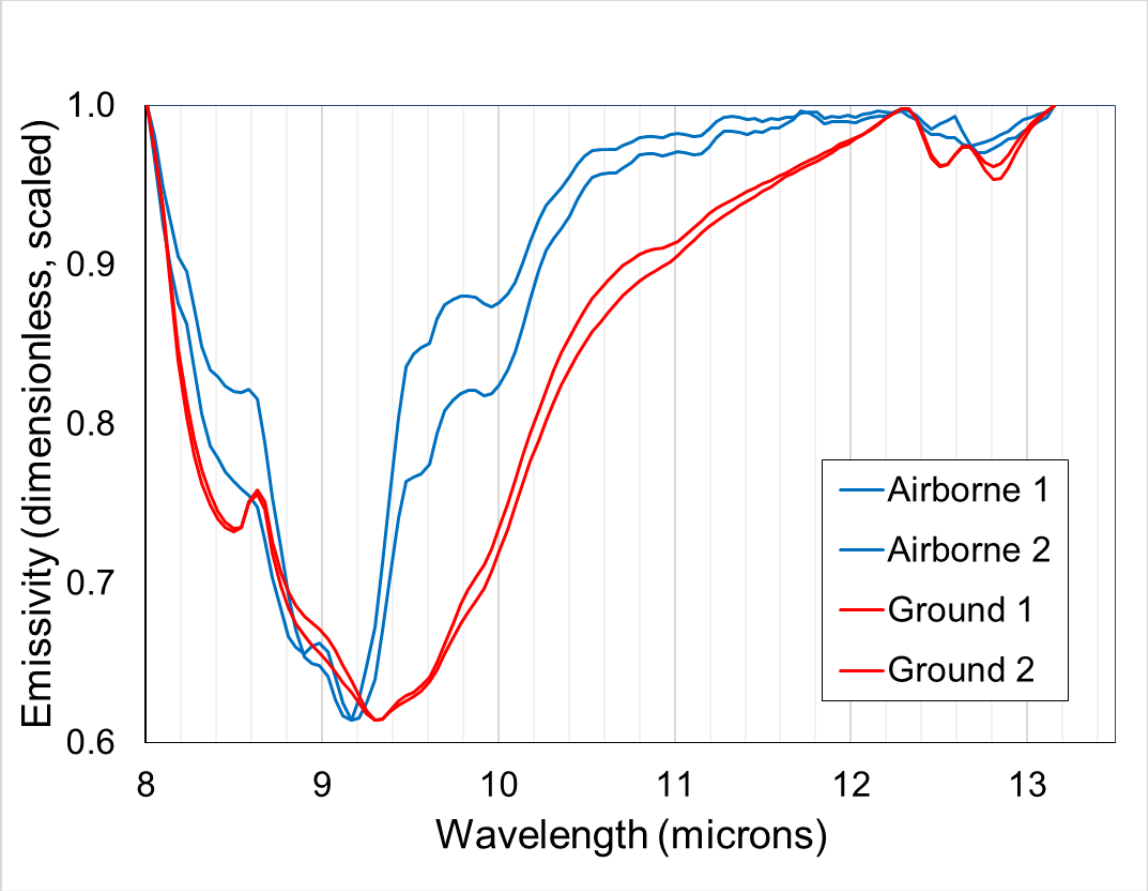
Emissivity (dimensionless, scaled)
1.0
0.9
0.8
0.7
0.6
8
9
10
11
12
13
Wavelength (microns)
Airborne 1
Airborne 2
Ground 1
Ground 2

Figure 14

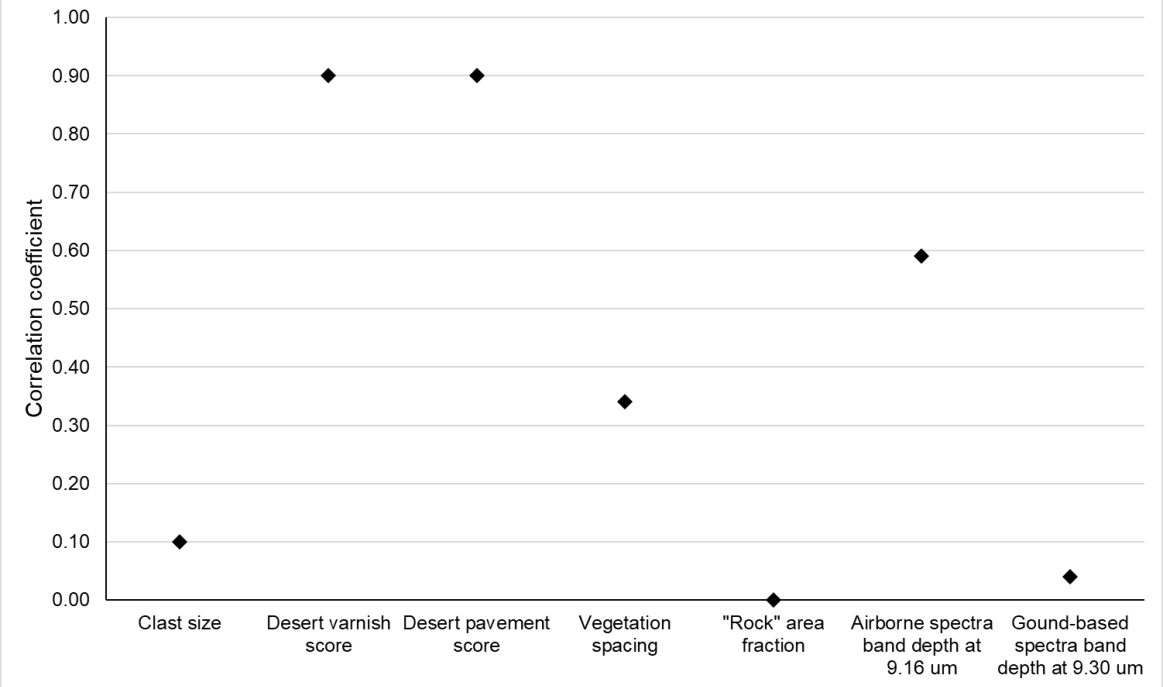
1.00
0.90
0.80
0.70
0.60
0.50
0.40
0.30
0.20
0.10
0.00
Correlation coefficient
Clast size
Desert varnish score
Desert pavement score
Vegetation spacing
"Rock" area fraction
Airborne spectra band depth at 9.16 um
Gound-based spectra band depth at 9.30 um

Figure 15

SUPPLEMENTAL ITEMS

Figure Captions

Figures S1-S27 (pp. 365-391): Field photographs and ground-based spectra for all 27 field sites (see Tables 1 and 2 in main text, site locations included in Table 2). (S1)-(S10), upstream field sites, in chronological order from youngest to oldest. (S11)-(S27), downstream field sites ordered from youngest to oldest. For each supplementary figure: (A) sample square meter field photograph (frame is 1 meter on edge, with a thickness of 2.5 cm). Site name/age seen on clipboard (lower right) is obsolete. Gray card (upper right) is present for a potential color analysis that was not completed for this study. Clasts on clipboard and gray card are not representative, but were placed to secure items from heavy wind. (B) Site overview field photograph (sample frame is 1 meter on edge). (C) Ground-based spectra. The accurate site name and age are in the upper right corner. The final, thicker spectrum is the site average (arithmetic mean) for all spectra.

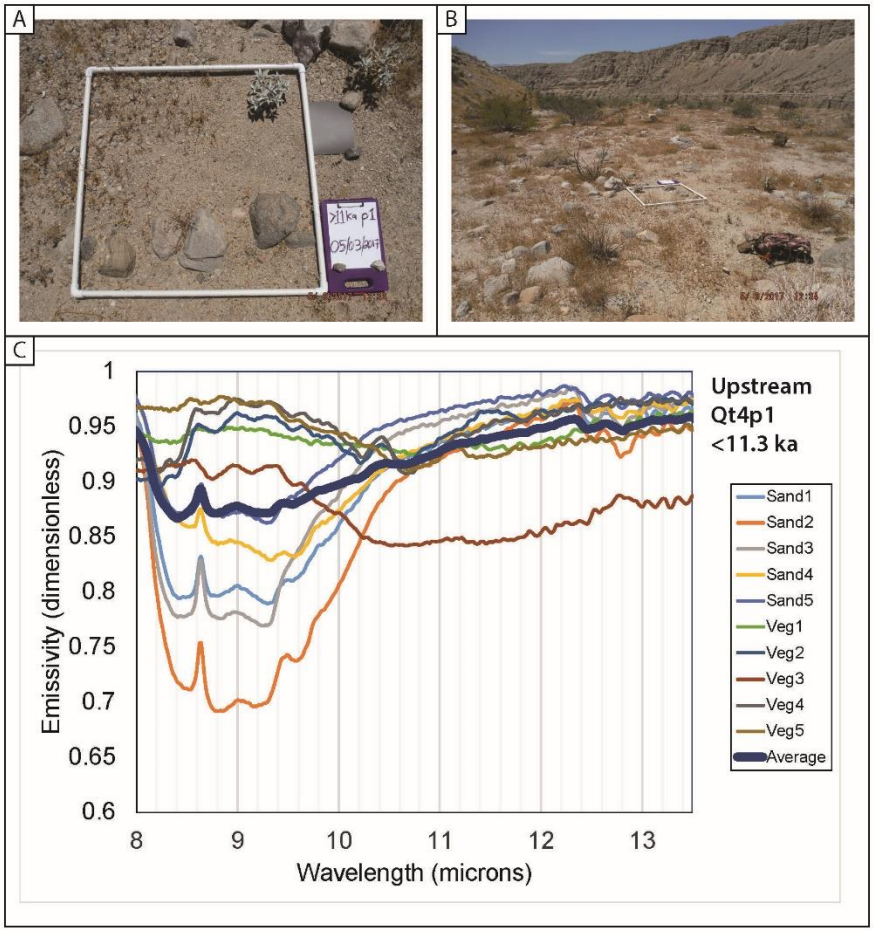
A
B
C
Emissivity (dimensionless)
1
0.95
0.9
0.85
0.8
0.75
0.7
0.65
0.6
8
9
10
11
12
13
Wavelength (microns)
Upstream
Qt4p1
<11.3 ka
Sand1
Sand2
Sand3
Sand4
Sand5
Veg1
Veg2
Veg3
Veg4
Veg5
Average

Figure S1

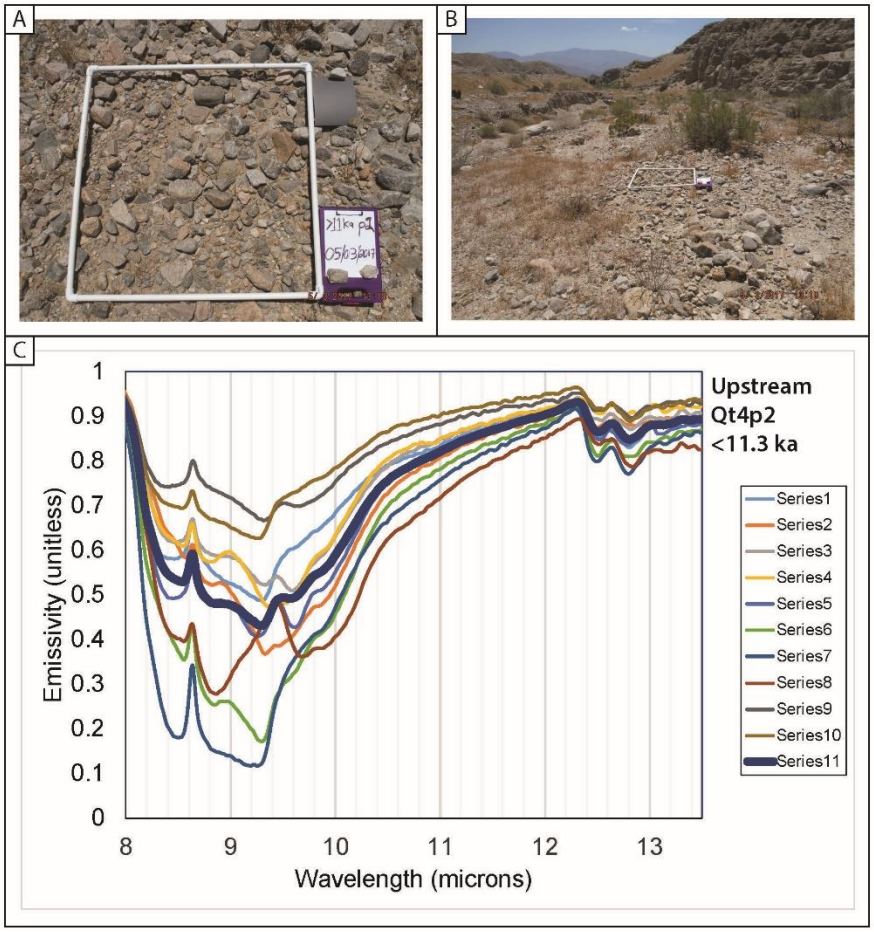
A
B
C
Upstream
Qt4p2
<11.3 ka
Emissivity (unitless)
Wavelength (microns)
Series1
Series2
Series3
Series4
Series5
Series6
Series7
Series8
Series9
Series10
Series11

Figure S2

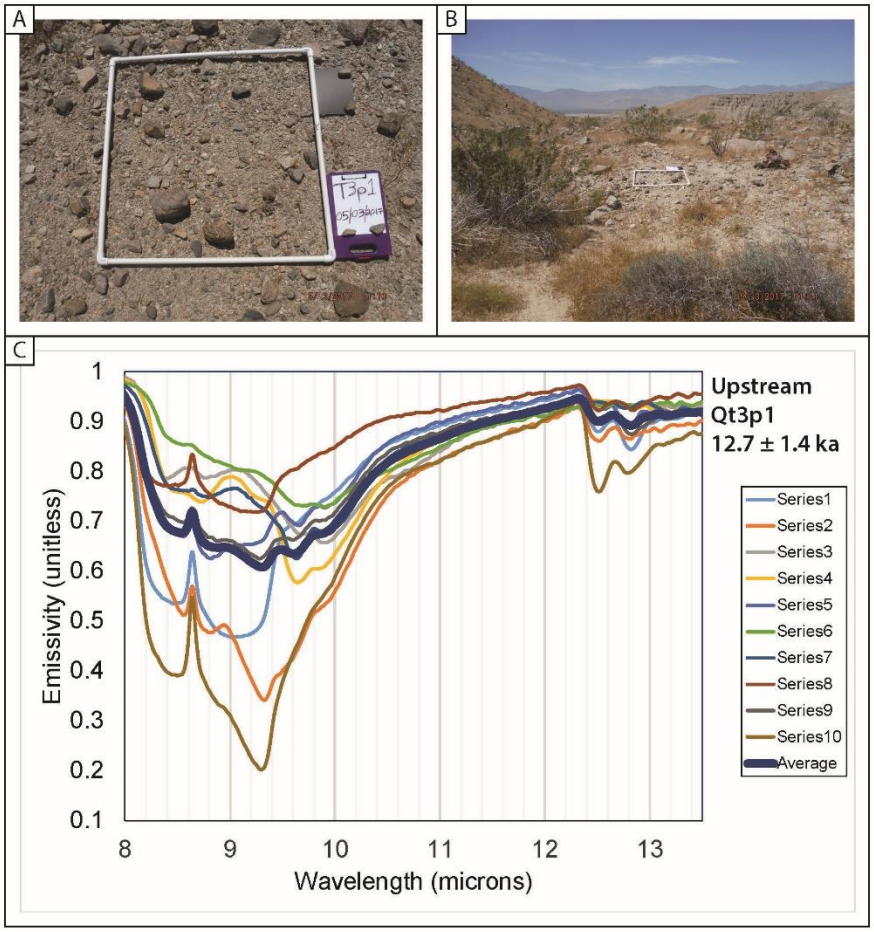
A
B
C
T3p1
Upstream
Qt3p1
12.7 ± 1.4 ka
Emissivity (unitless)
Wavelength (microns)
1
0.9
0.8
0.7
0.6
0.5
0.4
0.3
0.2
0.1
8
9
10
11
12
13
Series1
Series2
Series3
Series4
Series5
Series6
Series7
Series8
Series9
Series10
Average

Figure S3

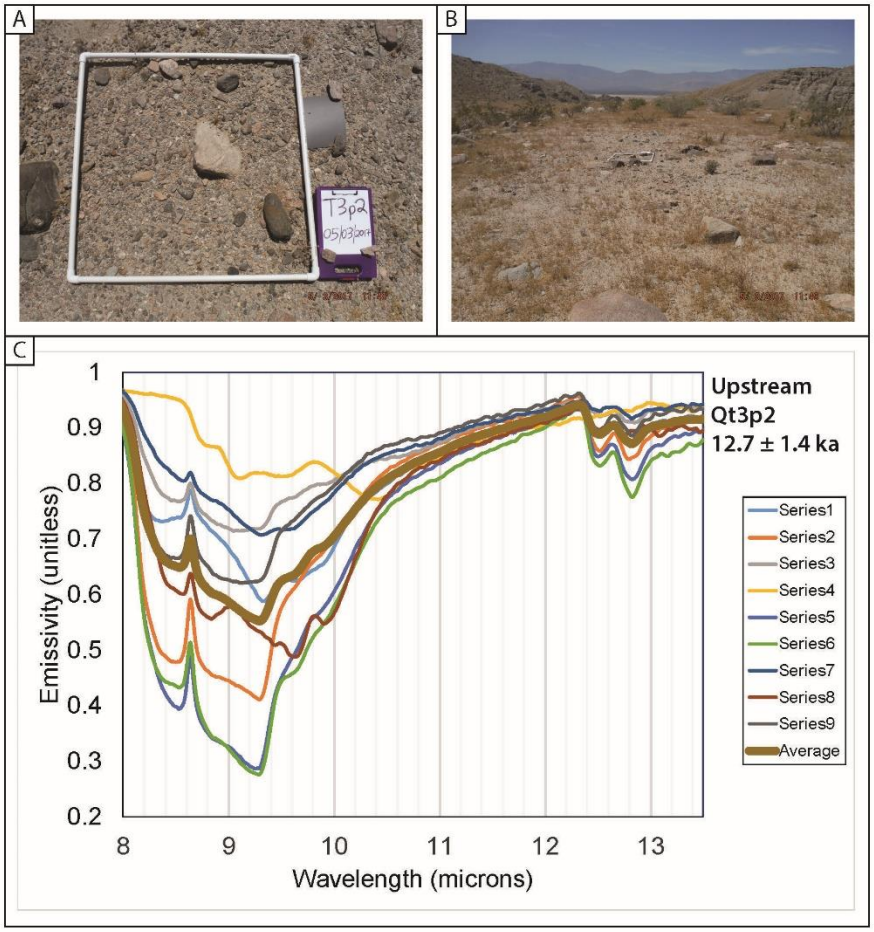
A
B
C
T3p2
05/03/2011
Upstream
Qt3p2
12.7 ± 1.4 ka
Emissivity (unitless)
1
0.9
0.8
0.7
0.6
0.5
0.4
0.3
0.2
8
9
10
11
12
13
Wavelength (microns)
Series1
Series2
Series3
Series4
Series5
Series6
Series7
Series8
Series9
Average

Figure S4

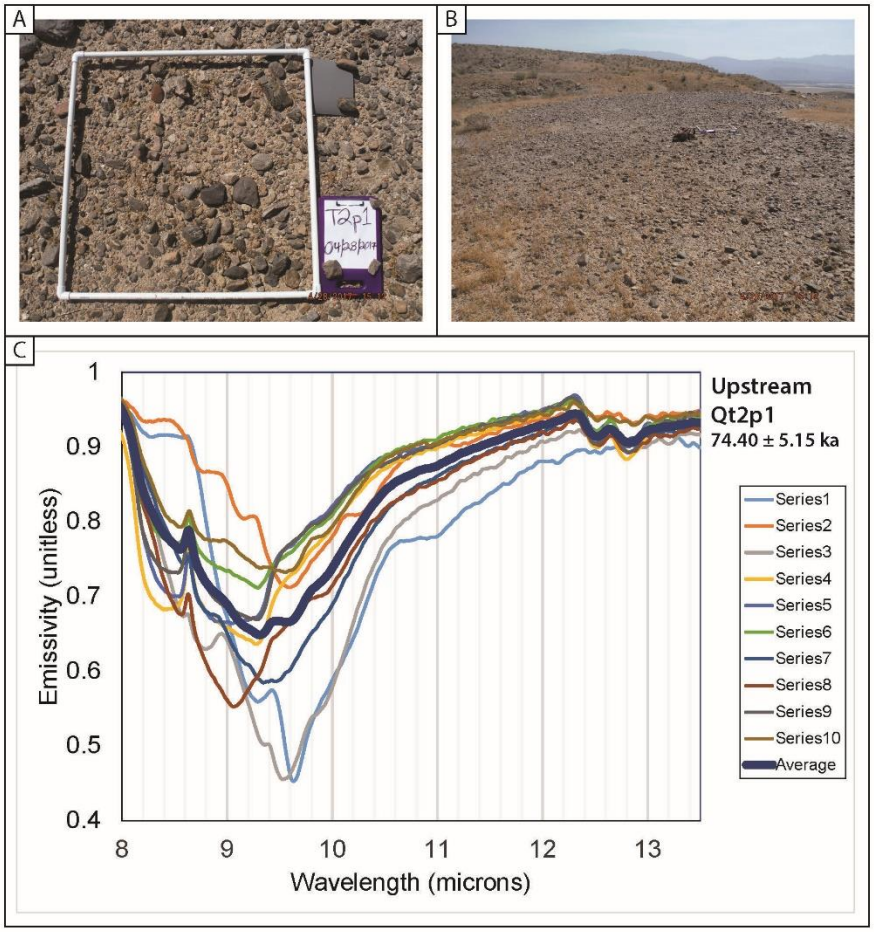
A
B
C
Upstream
Qt2p1
74.40 ± 5.15 ka
Emissivity (unitless)
Wavelength (microns)
1
0.9
0.8
0.7
0.6
0.5
0.4
8
9
10
11
12
13
Series1
Series2
Series3
Series4
Series5
Series6
Series7
Series8
Series9
Series10
Average

Figure S5

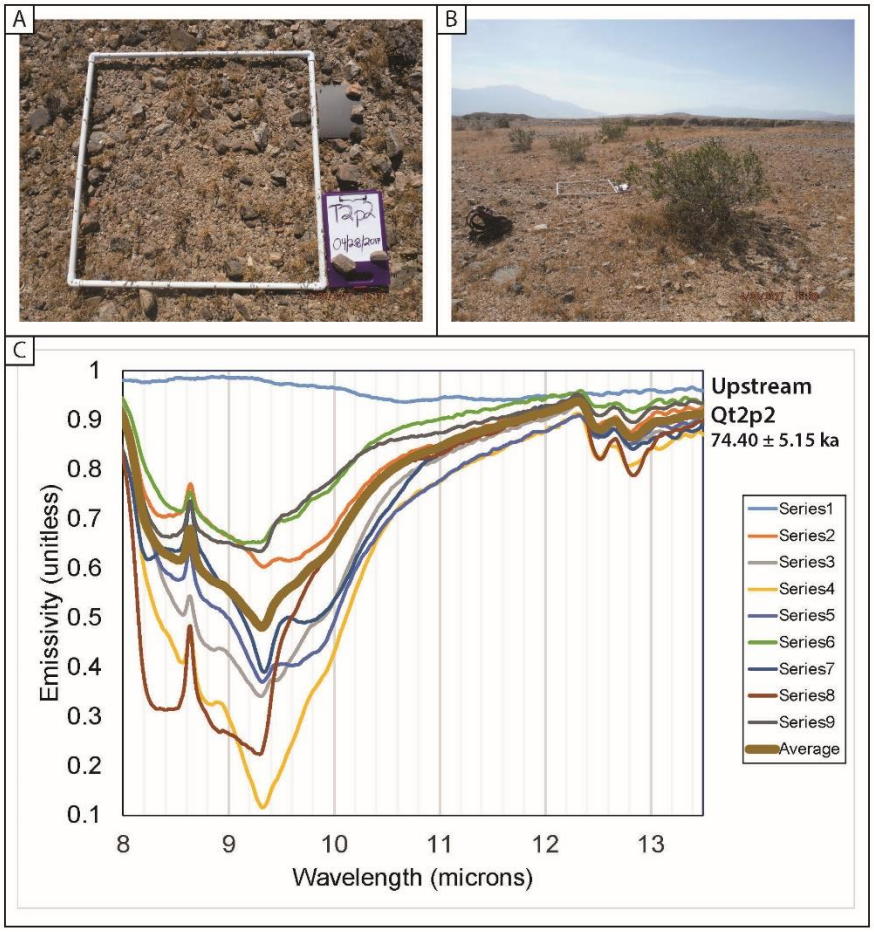
A
B
C
Upstream
Qt2p2
74.40 ± 5.15 ka
Emissivity (unitless)
Wavelength (microns)
Series1
Series2
Series3
Series4
Series5
Series6
Series7
Series8
Series9
Average

Figure S6

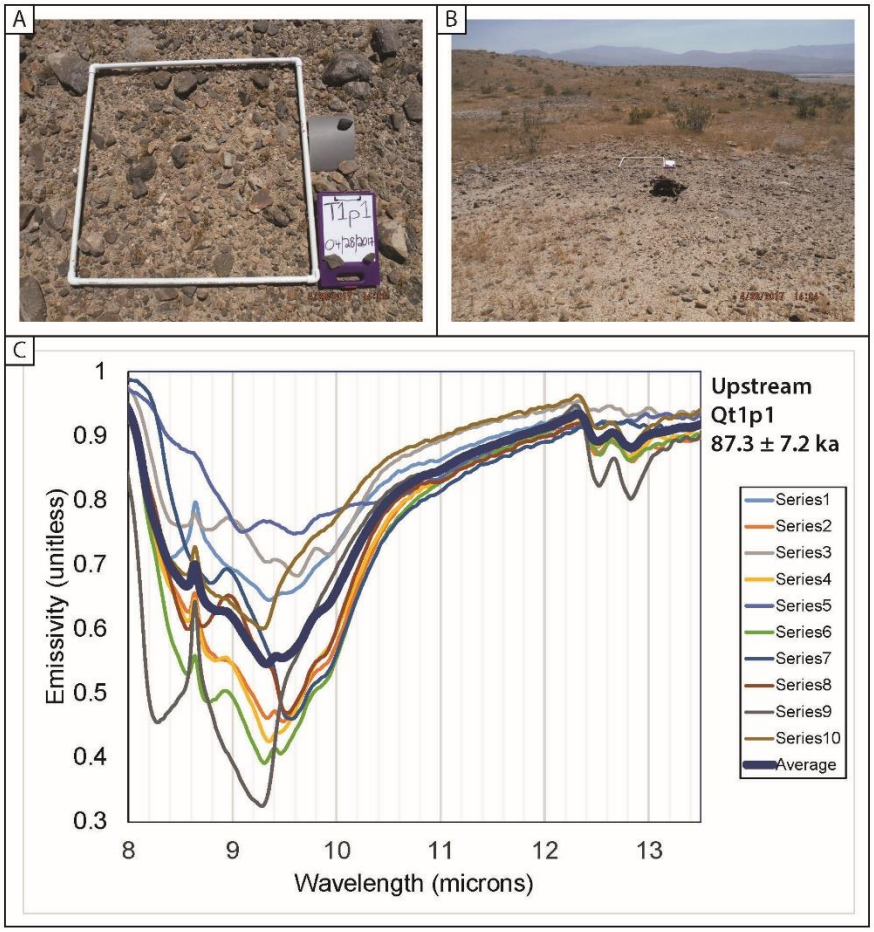
A
B
C
Upstream
Qt1p1
87.3 ± 7.2 ka
Emissivity (unitless)
Wavelength (microns)
1
0.9
0.8
0.7
0.6
0.5
0.4
0.3
8
9
10
11
12
13
Series1
Series2
Series3
Series4
Series5
Series6
Series7
Series8
Series9
Series10
Average

Figure S7

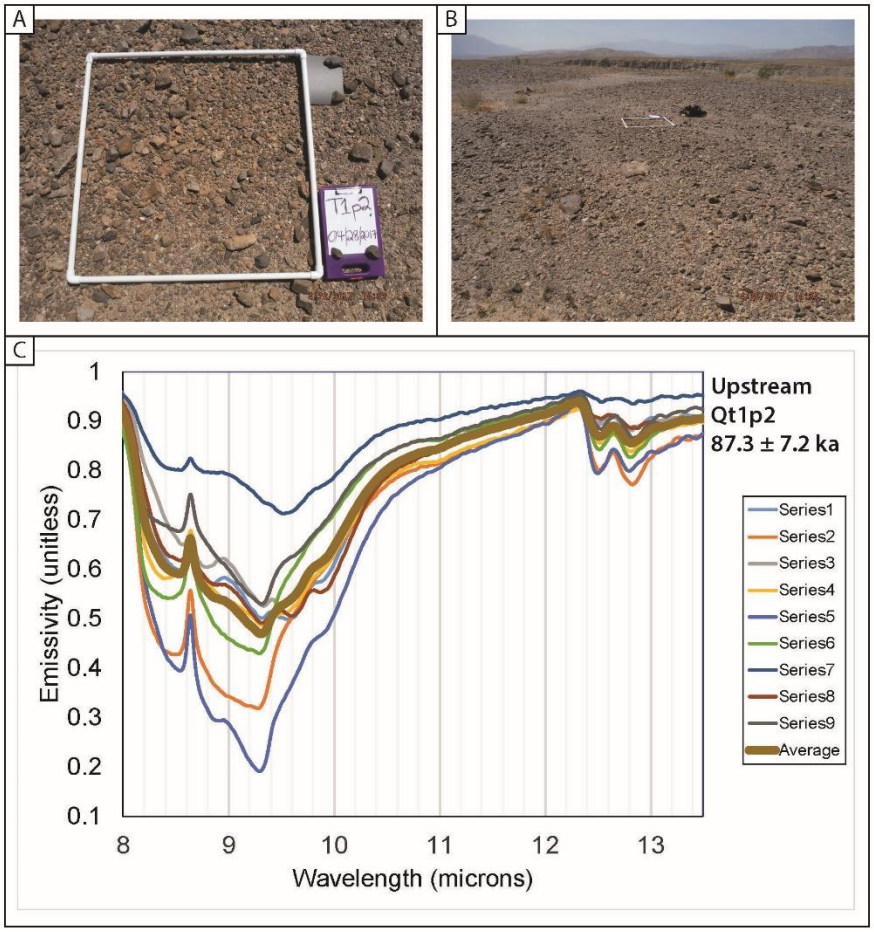
A
B
C
Upstream
Qt1p2
87.3 ± 7.2 ka
Emissivity (unitless)
Wavelength (microns)
Series1
Series2
Series3
Series4
Series5
Series6
Series7
Series8
Series9
Average

Figure S8

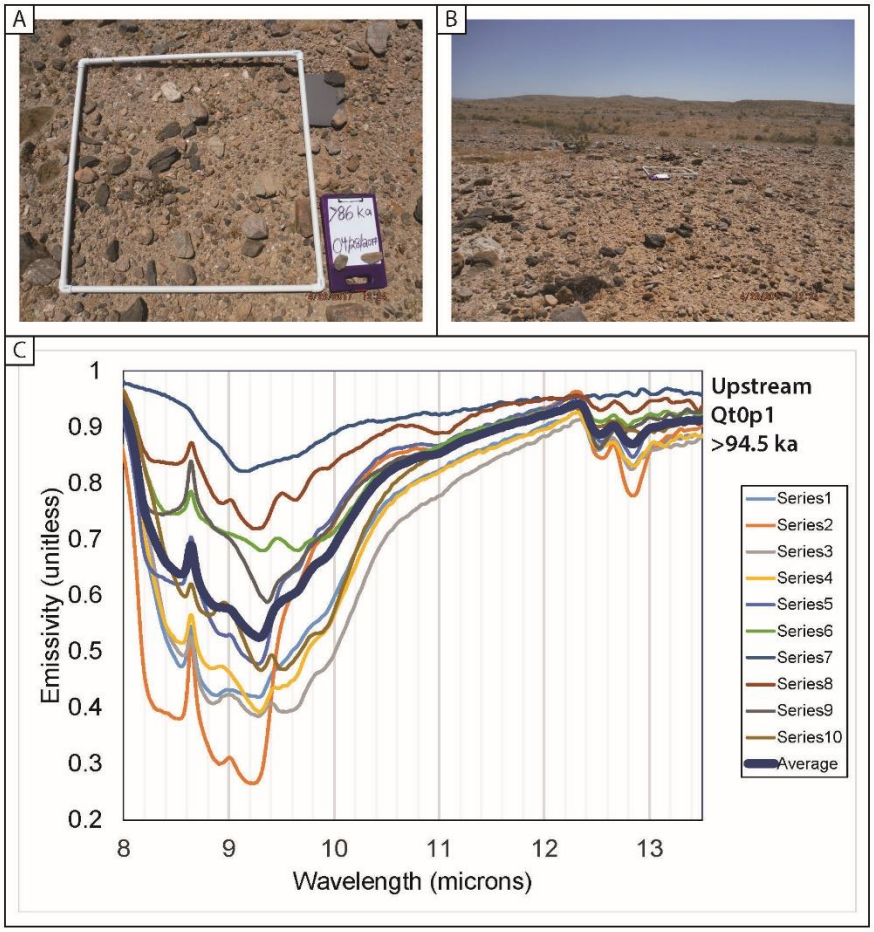
A
B
C
>86 ka
Upstream
Qt0p1
>94.5 ka
Emissivity (unitless)
Wavelength (microns)
1
0.9
0.8
0.7
0.6
0.5
0.4
0.3
0.2
8
9
10
11
12
13
Series1
Series2
Series3
Series4
Series5
Series6
Series7
Series8
Series9
Series10
Average

Figure S9

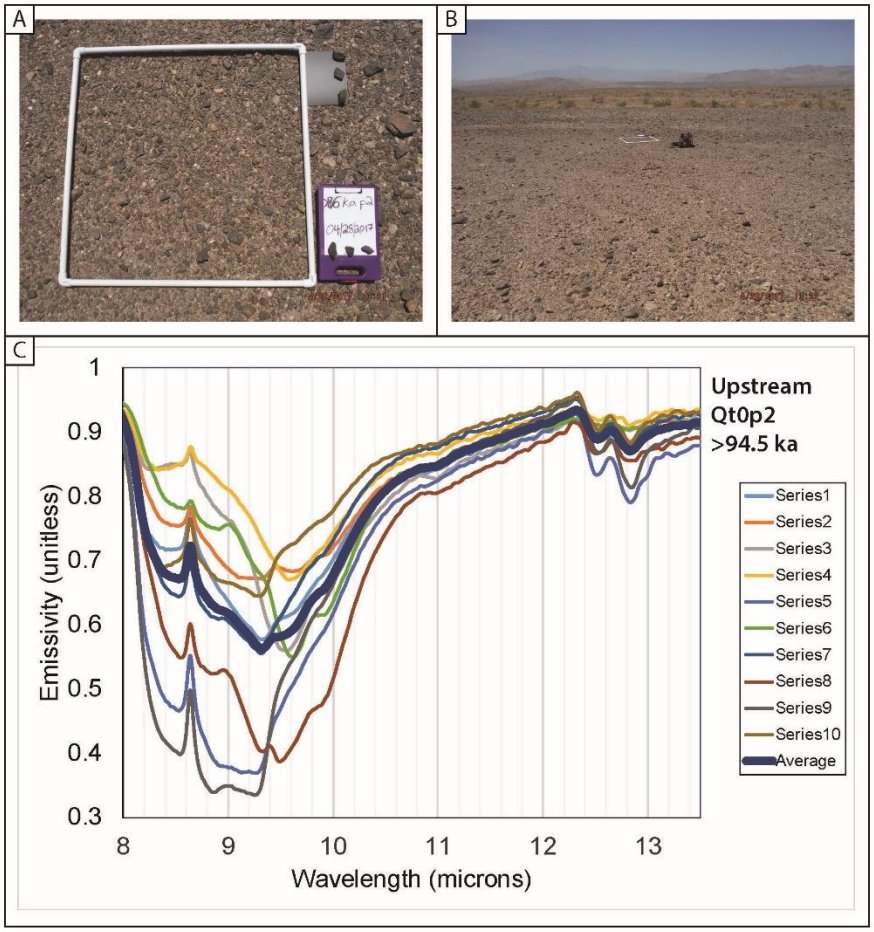
A
B
C
Upstream
Qt0p2
>94.5 ka
Emissivity (unitless)
Wavelength (microns)
1
0.9
0.8
0.7
0.6
0.5
0.4
0.3
8
9
10
11
12
13
Series1
Series2
Series3
Series4
Series5
Series6
Series7
Series8
Series9
Series10
Average

Figure S10

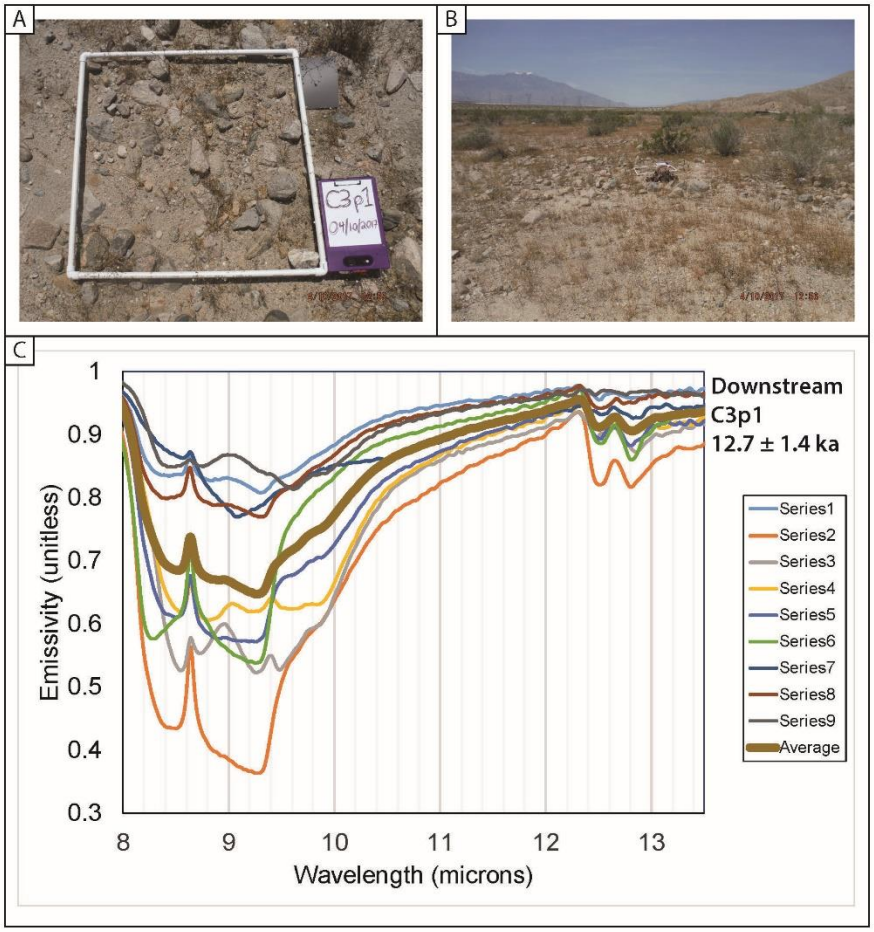
A
B
C3p1
04/10/2007
C
Emissivity (unitless)
1
0.9
0.8
0.7
0.6
0.5
0.4
0.3
8
9
10
11
12
13
Wavelength (microns)
Downstream
C3p1
12.7 ± 1.4 ka
Series1
Series2
Series3
Series4
Series5
Series6
Series7
Series8
Series9
Average

Figure S11

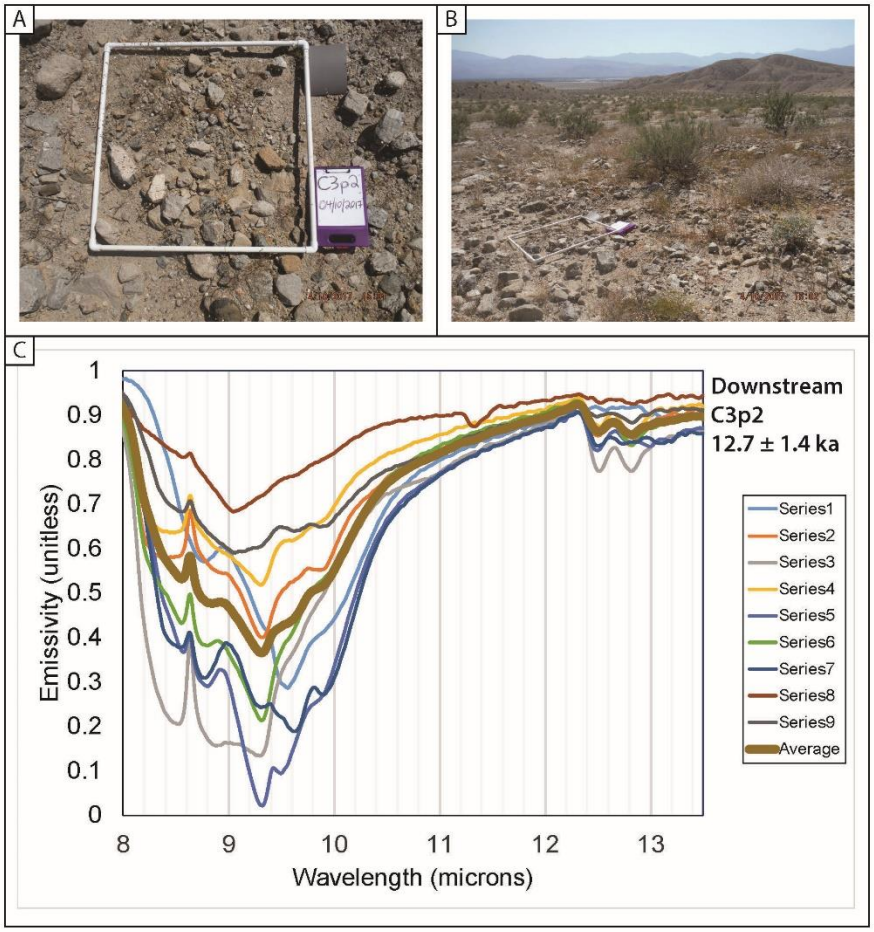
A
B
C
C3p2
Downstream
C3p2
12.7 ± 1.4 ka
Emissivity (unitless)
Wavelength (microns)
Series1
Series2
Series3
Series4
Series5
Series6
Series7
Series8
Series9
Average

Figure S12

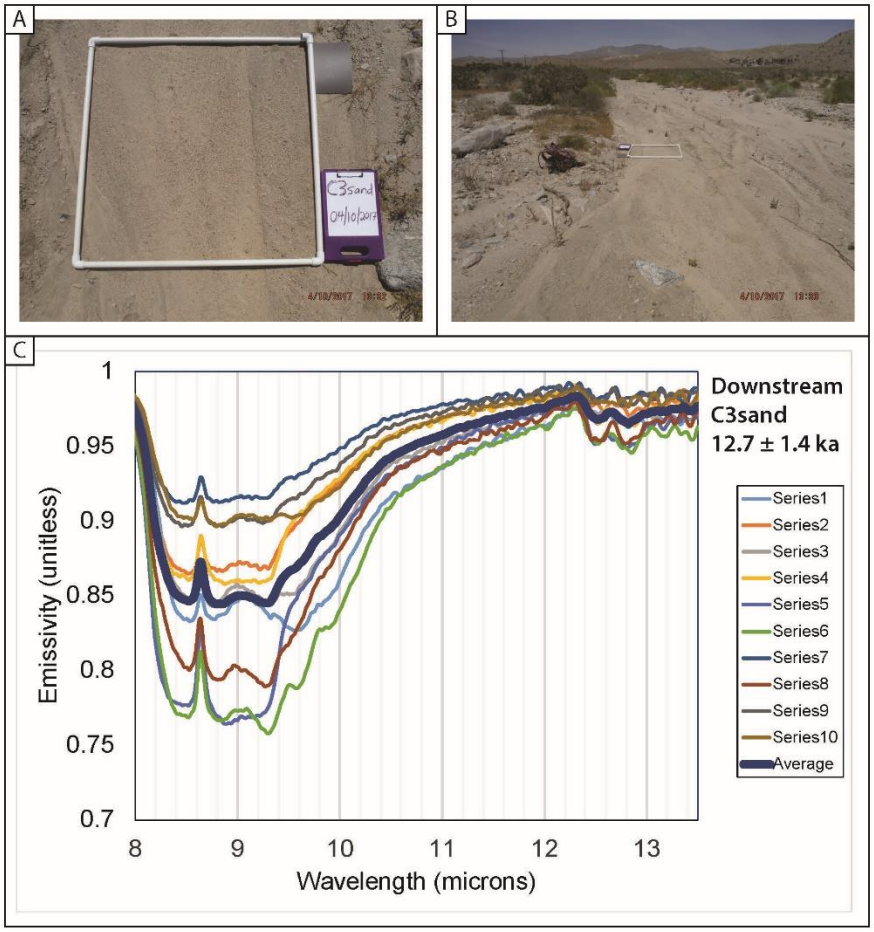
A
B
C3sand
04/10/2017
C
Emissivity (unitless)
1
0.95
0.9
0.85
0.8
0.75
0.7
8
9
10
11
12
13
Wavelength (microns)
Downstream
C3sand
12.7 ± 1.4 ka
Series1
Series2
Series3
Series4
Series5
Series6
Series7
Series8
Series9
Series10
Average

Figure S13

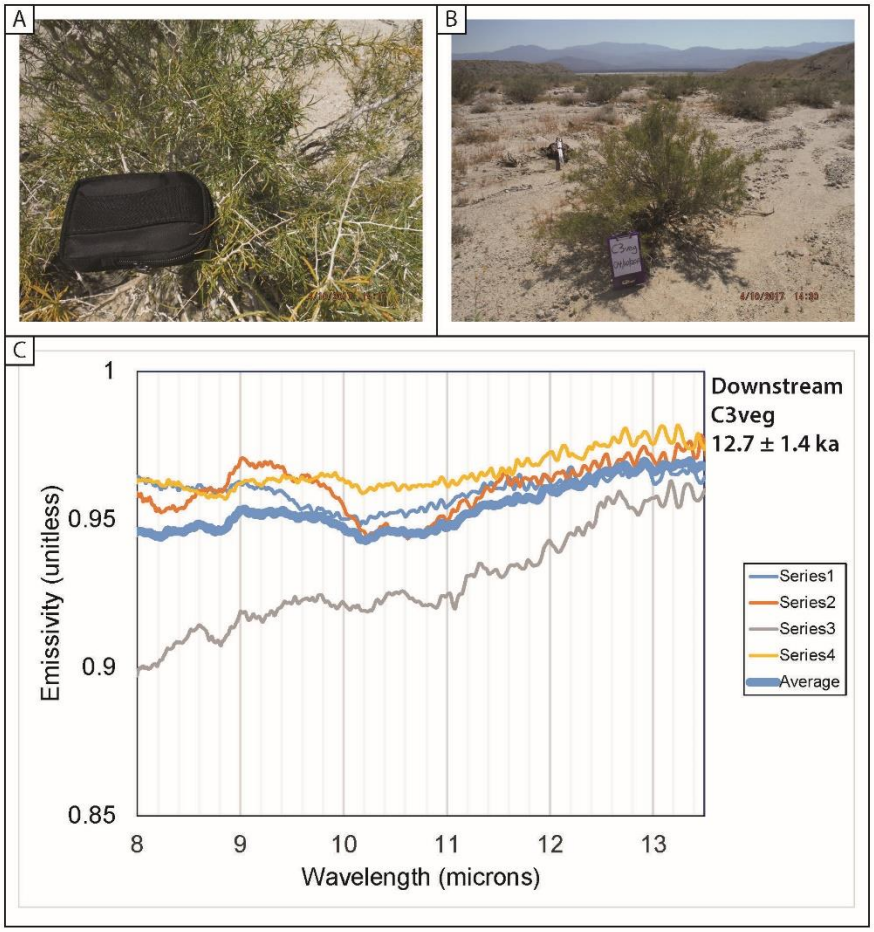
A
B
C
Downstream
C3veg
12.7 ± 1.4 ka
Emissivity (unitless)
1
0.95
0.9
0.85
8
9
10
11
12
13
Wavelength (microns)
Series1
Series2
Series3
Series4
Average

Figure S14

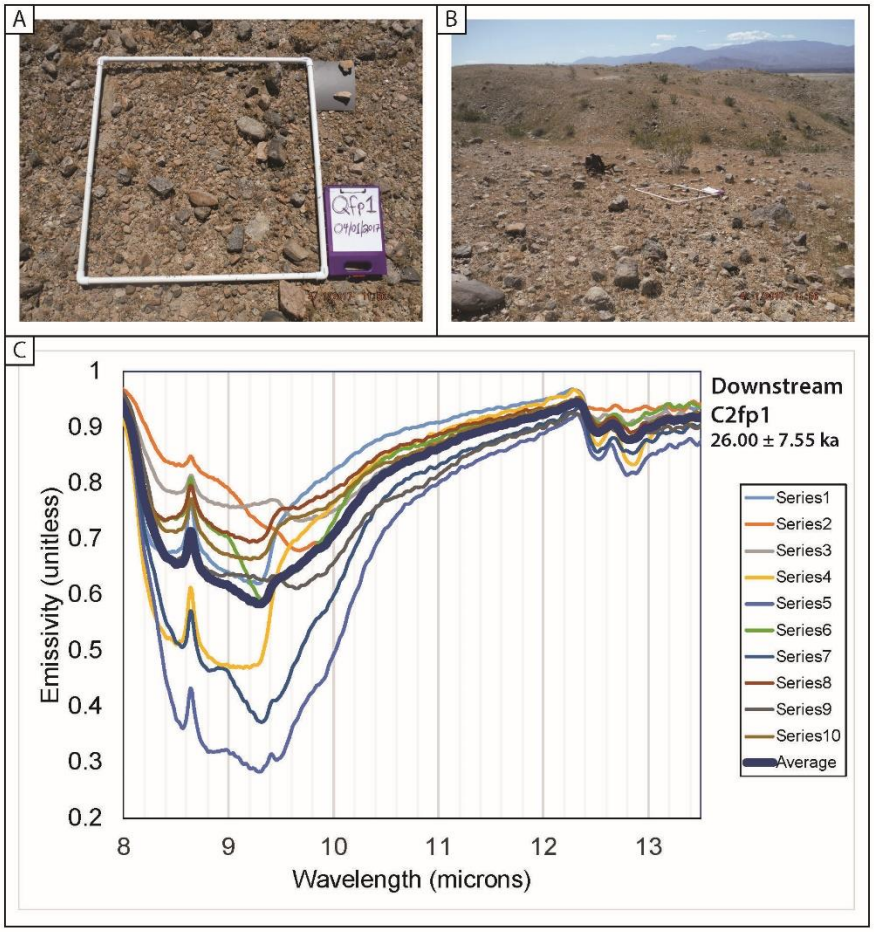
A
B
C
Qfp1
Downstream
C2fp1
26.00 ± 7.55 ka
Emissivity (unitless)
Wavelength (microns)
1
0.9
0.8
0.7
0.6
0.5
0.4
0.3
0.2
8
9
10
11
12
13
Series1
Series2
Series3
Series4
Series5
Series6
Series7
Series8
Series9
Series10
Average

Figure S15

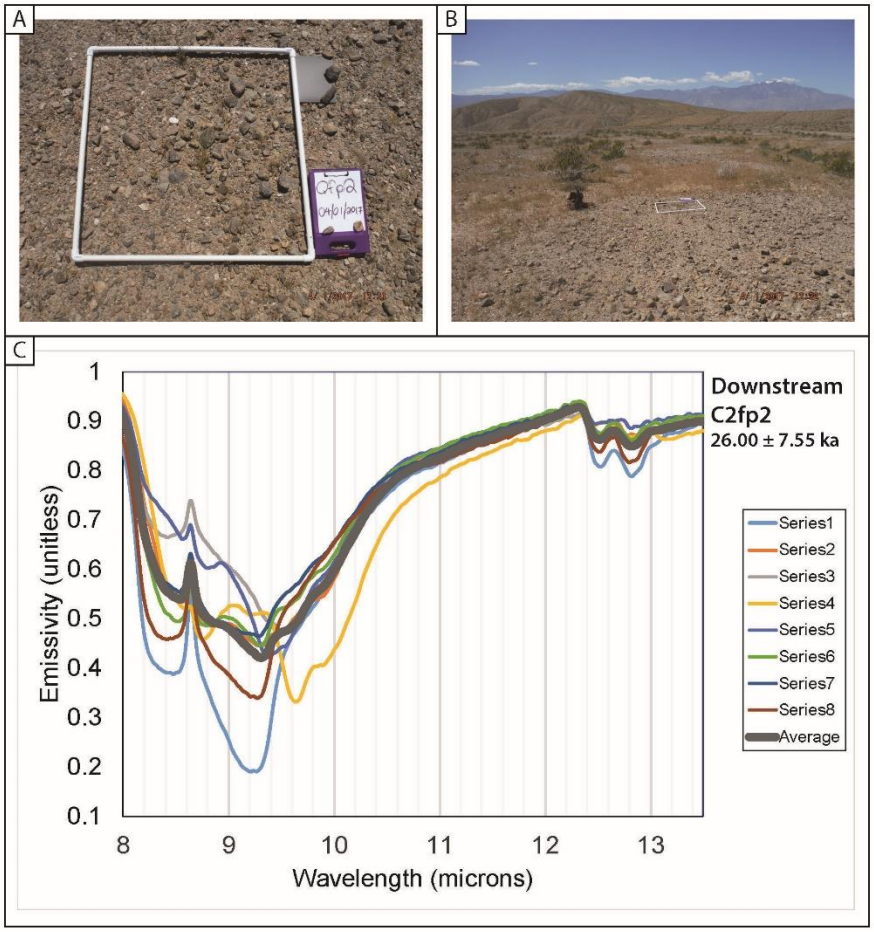
A
B
C
Downstream
C2fp2
26.00 ± 7.55 ka
Emissivity (unitless)
Wavelength (microns)
1
0.9
0.8
0.7
0.6
0.5
0.4
0.3
0.2
0.1
8
9
10
11
12
13
Series1
Series2
Series3
Series4
Series5
Series6
Series7
Series8
Average

Figure S16

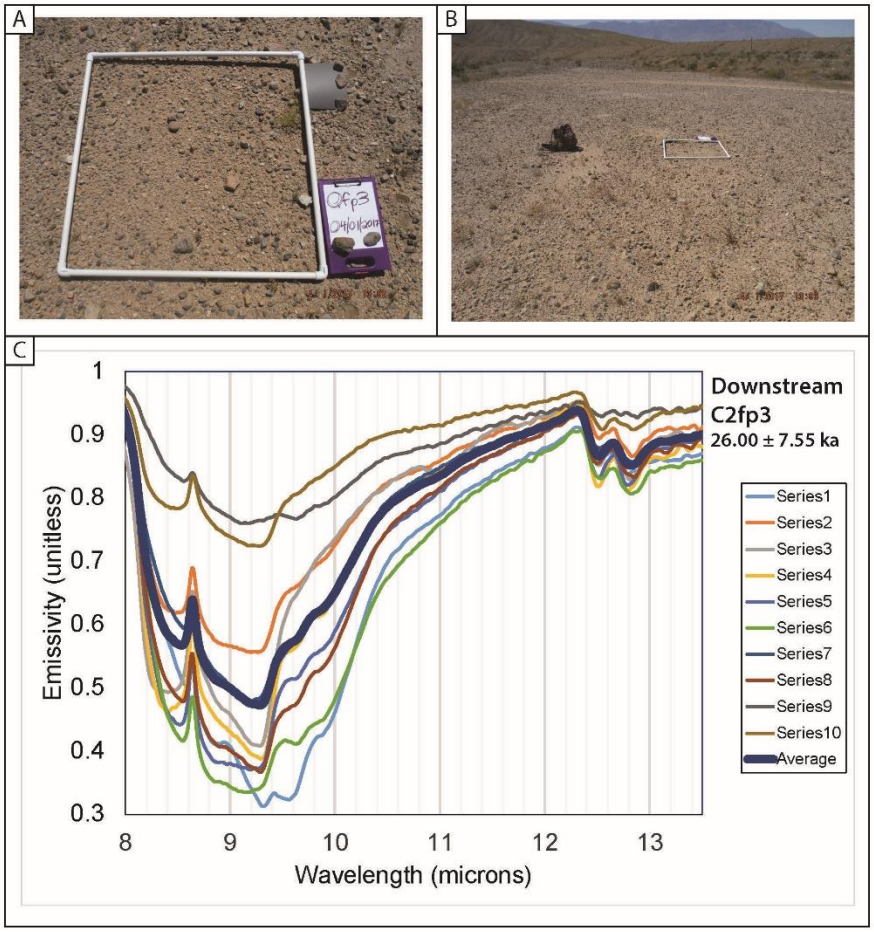
A
B
C
Qfp3
Downstream
C2fp3
26.00 ± 7.55 ka
Emissivity (unitless)
Wavelength (microns)
1
0.9
0.8
0.7
0.6
0.5
0.4
0.3
8
9
10
11
12
13
Series1
Series2
Series3
Series4
Series5
Series6
Series7
Series8
Series9
Series10
Average

Figure S17

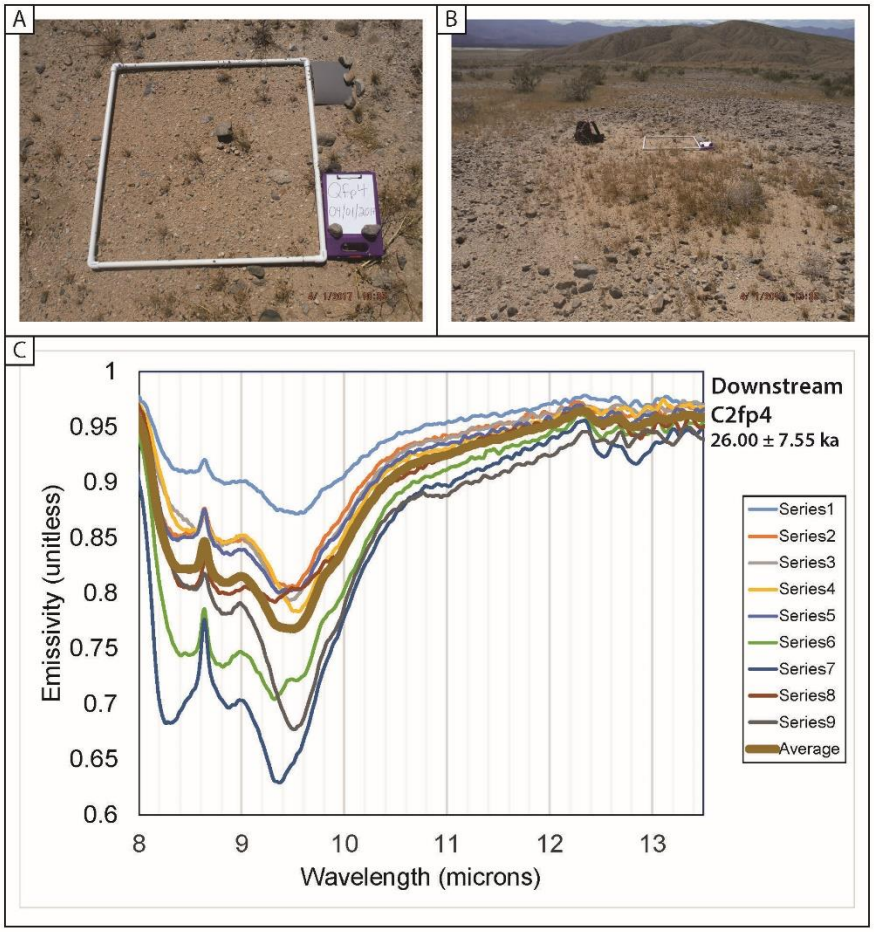
A
B
C
Downstream
C2fp4
26.00 ± 7.55 ka
Emissivity (unitless)
Wavelength (microns)
1
0.95
0.9
0.85
0.8
0.75
0.7
0.65
0.6
8
9
10
11
12
13
Series1
Series2
Series3
Series4
Series5
Series6
Series7
Series8
Series9
Average

Figure S18

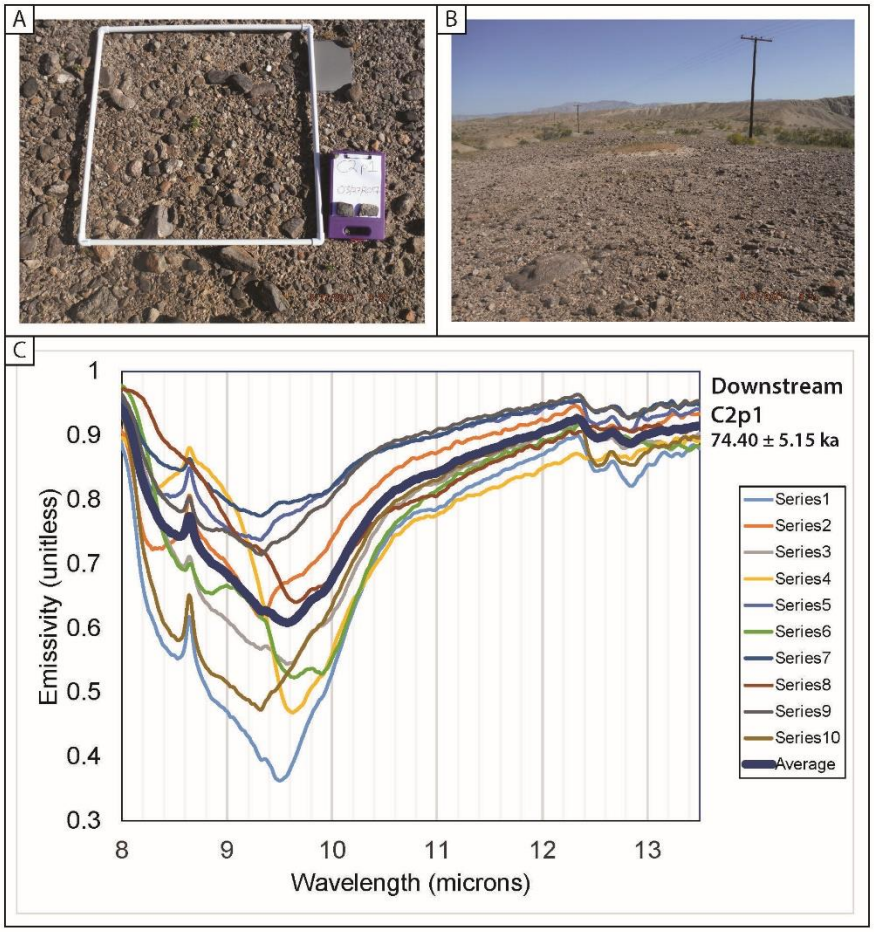
A
B
C
Downstream
C2p1
74.40 ± 5.15 ka
Emissivity (unitless)
1
0.9
0.8
0.7
0.6
0.5
0.4
0.3
8
9
10
11
12
13
Wavelength (microns)
Series1
Series2
Series3
Series4
Series5
Series6
Series7
Series8
Series9
Series10
Average

Figure S19

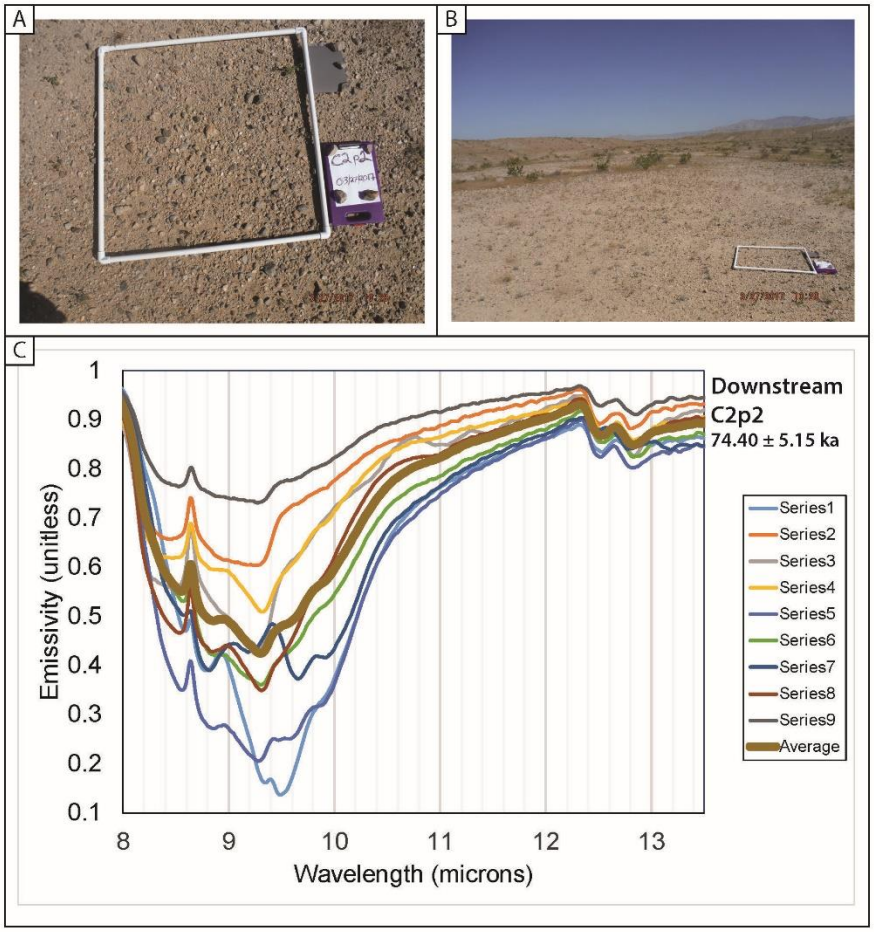
A
B
C
Downstream
C2p2
74.40 ± 5.15 ka
Emissivity (unitless)
Wavelength (microns)
1
0.9
0.8
0.7
0.6
0.5
0.4
0.3
0.2
0.1
8
9
10
11
12
13
Series1
Series2
Series3
Series4
Series5
Series6
Series7
Series8
Series9
Average

Figure S20

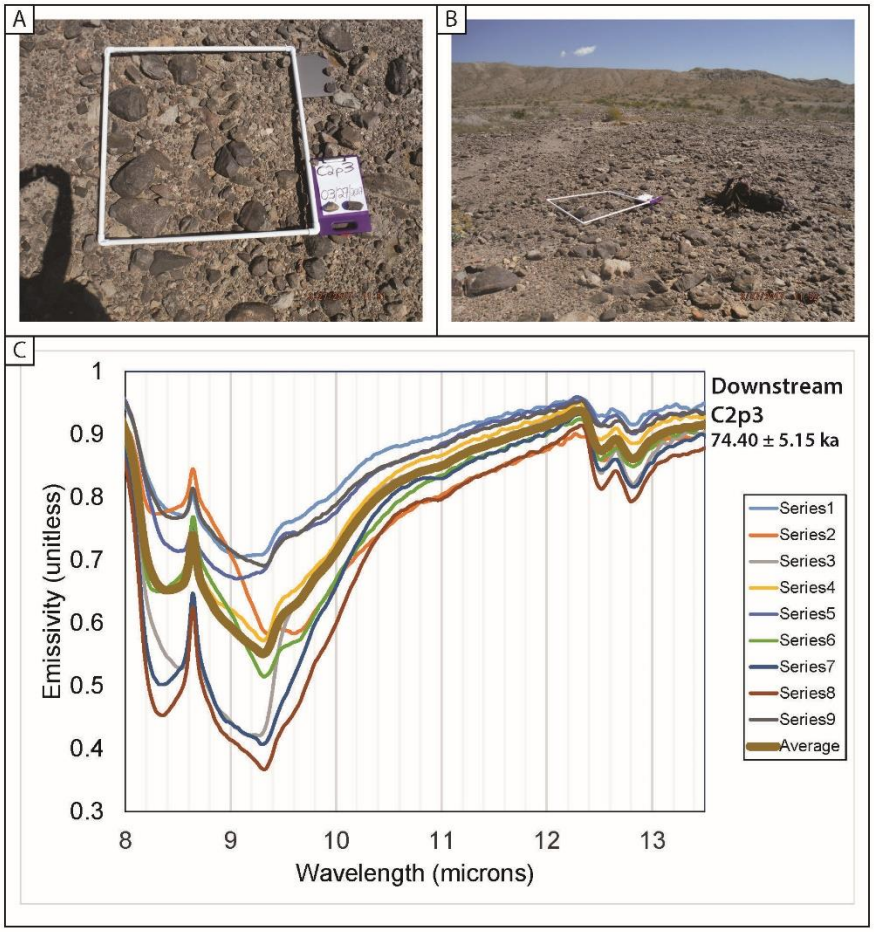
A
B
C
Downstream
C2p3
74.40 ± 5.15 ka
Emissivity (unitless)
Wavelength (microns)
1
0.9
0.8
0.7
0.6
0.5
0.4
0.3
8
9
10
11
12
13
Series1
Series2
Series3
Series4
Series5
Series6
Series7
Series8
Series9
Average

Figure S21

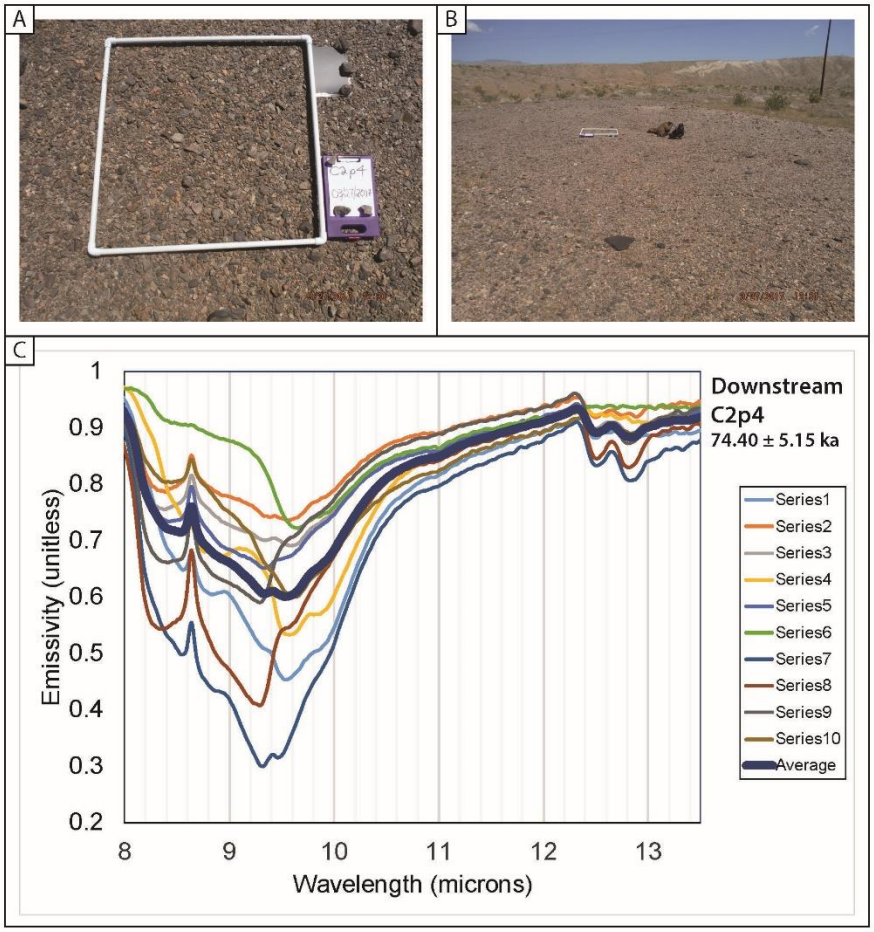
A
B
C
Downstream
C2p4
74.40 ± 5.15 ka
Emissivity (unitless)
Wavelength (microns)
1
0.9
0.8
0.7
0.6
0.5
0.4
0.3
0.2
8
9
10
11
12
13
Series1
Series2
Series3
Series4
Series5
Series6
Series7
Series8
Series9
Series10
Average

Figure S22

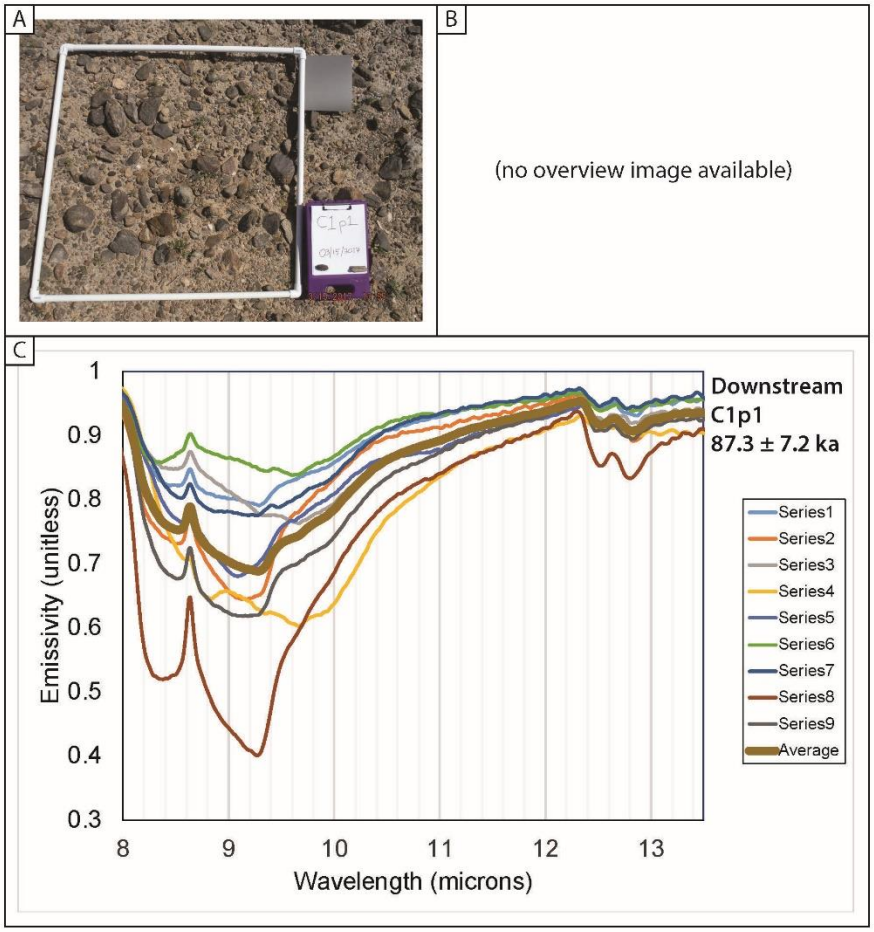
A
B
(no overview image available)
C
C1p1
Emissivity (unitless)
1
0.9
0.8
0.7
0.6
0.5
0.4
0.3
8
9
10
11
12
13
Wavelength (microns)
Downstream
C1p1
87.3 ± 7.2 ka
Series1
Series2
Series3
Series4
Series5
Series6
Series7
Series8
Series9
Average

Figure S23

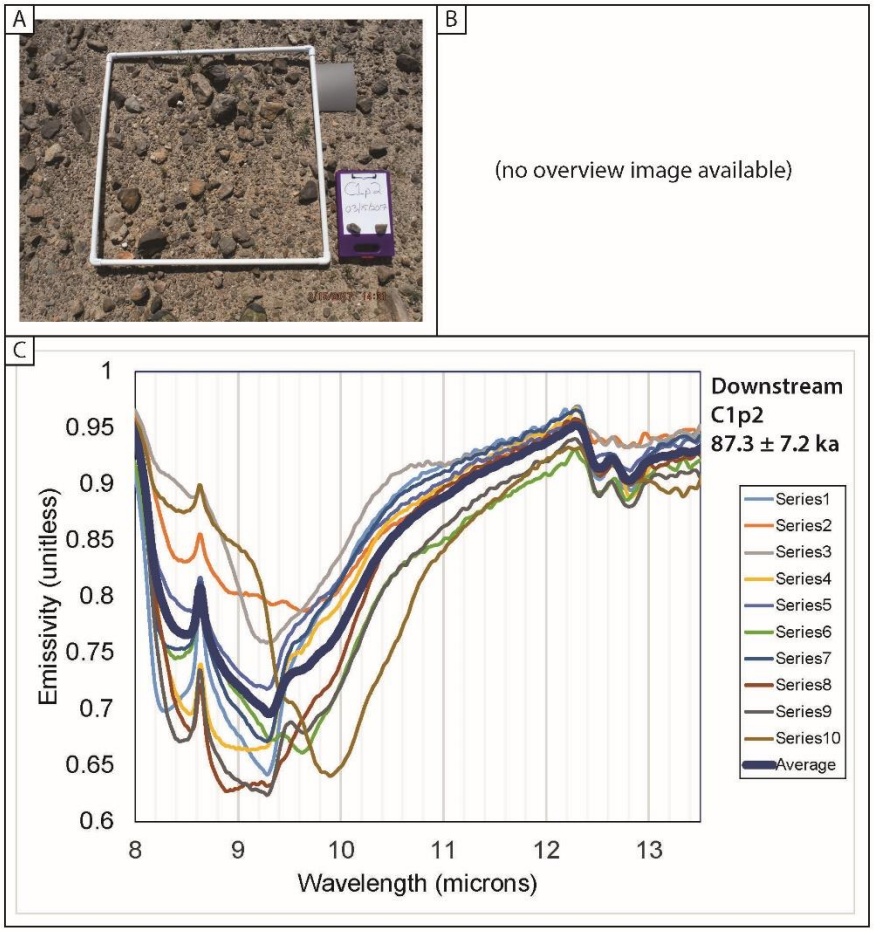
A
B
(no overview image available)
C
Downstream
C1p2
87.3 ± 7.2 ka
Emissivity (unitless)
Wavelength (microns)
1
0.95
0.9
0.85
0.8
0.75
0.7
0.65
0.6
8
9
10
11
12
13
Series1
Series2
Series3
Series4
Series5
Series6
Series7
Series8
Series9
Series10
Average

Figure S24

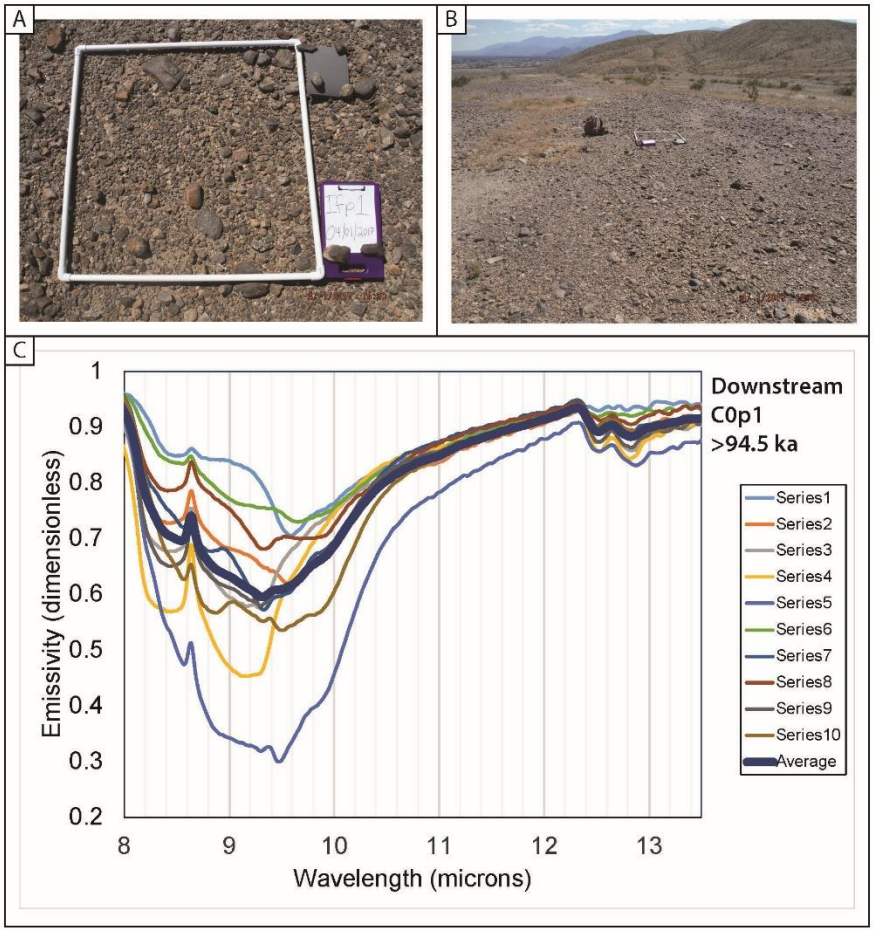
A
B
C
Downstream
C0p1
>94.5 ka
Emissivity (dimensionless)
Wavelength (microns)
1
0.9
0.8
0.7
0.6
0.5
0.4
0.3
0.2
8
9
10
11
12
13
Series1
Series2
Series3
Series4
Series5
Series6
Series7
Series8
Series9
Series10
Average

Figure S25

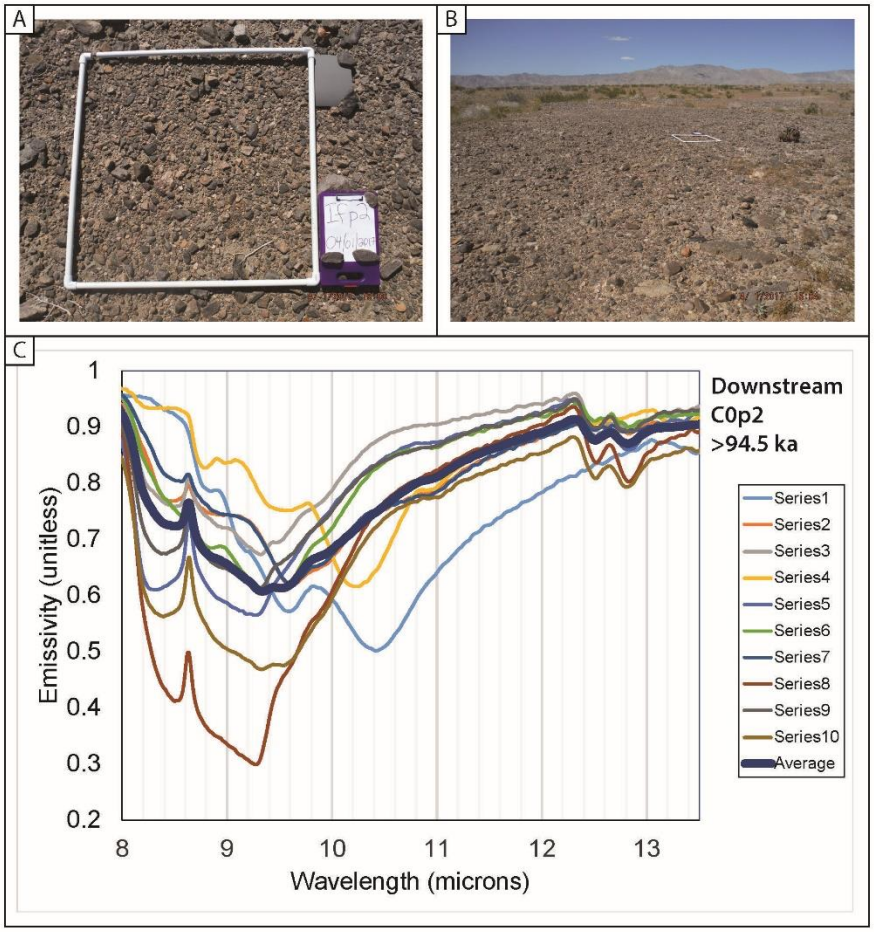
A
B
C
Emissivity (unitless)
1
0.9
0.8
0.7
0.6
0.5
0.4
0.3
0.2
8
9
10
11
12
13
Wavelength (microns)
Downstream
C0p2
>94.5 ka
Series1
Series2
Series3
Series4
Series5
Series6
Series7
Series8
Series9
Series10
Average

Figure S26

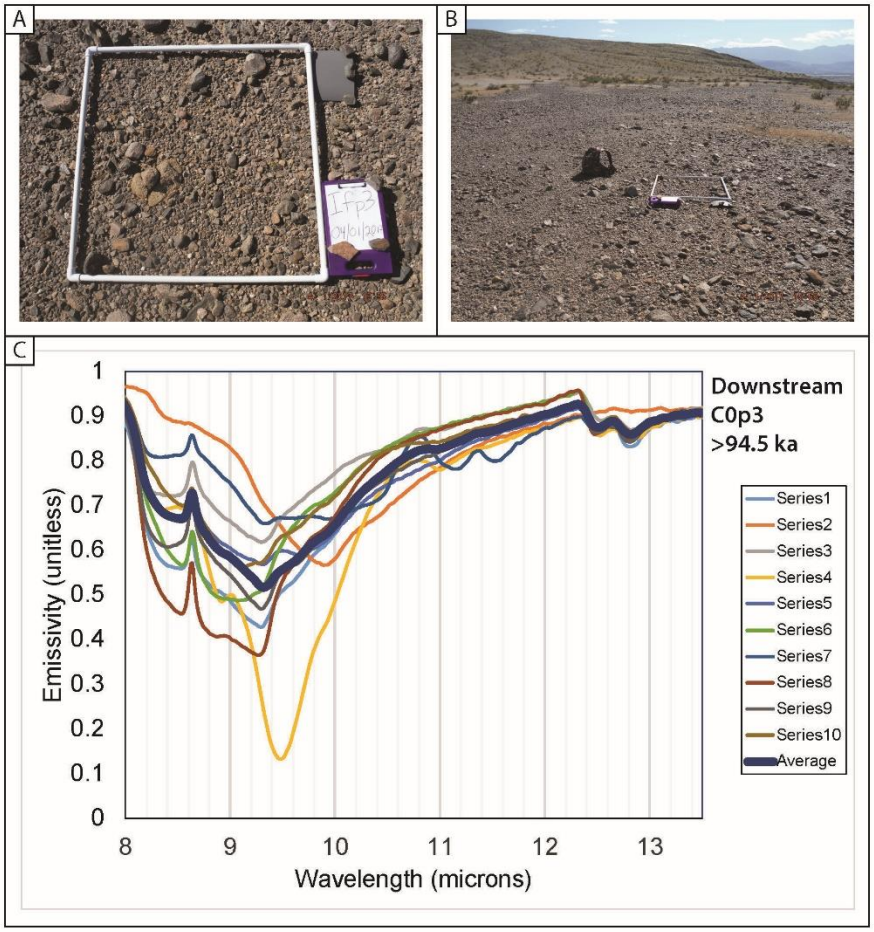
A
B
C
Downstream
C0p3
>94.5 ka
Emissivity (unitless)
Wavelength (microns)
Series1
Series2
Series3
Series4
Series5
Series6
Series7
Series8
Series9
Series10
Average

Figure S27